# 國立交通大學

## 光電工程研究所

## 博 士 論 文

面射型雷射高頻特性之研究
High speed characteristics of Vertical-Cavity
Surface-Emitting Laser

研 究 生：張亞衛

指導教授：王興宗　博士

　　　　　郭浩中　博士

中 華 民 國 九 十 四 年 七 月

面射型雷射高頻特性之研究
# High speed characteristics of Vertical-Cavity Surface-Emitting Laser

研 究 生：張亞銜　　　　　Student：Ya-Hsien Chang

指導教授：王興宗 博士　　　Advisor：Dr. Shing-Chung Wang

　　　　　郭浩中 博士　　　　　　　 Dr. Hao-Chung Kuo

國 立 交 通 大 學　電機資訊學院
光電工程研究所
博 士 論 文

A Thesis
Submitted to Institute of Electro-Optical Engineering
College of Electrical Engineering and Computer Science
National Chiao Tung University
in partial Fulfillment of the Requirements
for the Degree of
Doctor of Philosophy
in

Electro-Optical Engineering

July 2005

Hsinchu, Taiwan, Republic of China

中華民國九十四年七月

# 面射型雷射高頻特性之研究

研究生：張亞衛　　　　　　　　　　　　　　指導教授：王興宗 教授

　　　　　　　　　　　　　　　　　　　　　　　　　　郭浩中 教授

國立交通大學光電工程研究所

## 摘要

　　本論文旨在探討面射型雷射高頻特性的改進之道。從雷射發光層的材料、元件結構與元件等效的寄生電阻電容來改進面射型雷射的高頻操作特性，包跨小信號頻寬與眼圖。本論文第一部份為使用InGaAsP/InGaP為雷射增益層的面射型雷射。InGaAsP/InGaP材料的最佳化可藉由光激輝光光譜與理論模擬來達到，理論證明此種量子井具有較大的光增益與較低的透明電流。元件部分其臨界電流與微分效率分別為 0.4 mA 與 0.6 W/A，相較於傳統的GaAs/AlGaAs量子井，InGaAsP/InGaP具有較高的熱穩定度，當基板溫度從室溫升高到 $85^{\circ}$C時，其臨界電流僅僅升高了 0.2 mA。其小信號頻寬可達 14.5 GHz 而電流調制效率為 $11.6\ \mathrm{GHz/(mA)^{1/2}}$，我們同時展示了 12.5 Gb/s的眼圖，證明了InGaAsP/InGaP極適合作為高速面射型雷射的主動層。論文的第二部份則聚焦在如何降低在元件的等效電容。我們使用離子佈植($\mathrm{H^+}$)方法成功阻斷了元件的特性電容使小信號頻寬由 2.3 GHz增加到 9 GHz，其 10 Gb/s的眼圖也大幅改善，可通過 802.3ae所規範的遮罩。為了精確得知元件在離子佈植前後的電容與阻抗，我們建立了面射型雷射的等效電路，使用Agilent ADS軟體從元件量測到的阻抗係數(S11)抽取元件的接面電容，結果證明離子佈植技術能有效降低雷射寄生電容。論文的最後部分，我們使用漸變氧化層來取代傳統單一組成氧化層，以做為面射型雷射的電流侷限與光學侷限。漸變氧化層可提供漸變的折射率分佈，理論上可以減少元件的高頻操作時的阻泥係數。我們發現使用漸變氧化層的面射型雷射具有相似的靜態特性(LIV)，但是其小信號頻寬則由 10 GHz增加到 13.2 GHz，阻泥係數也降低了一倍，顯示漸變氧化層的確可以改善雷射的高頻響應。

# High speed characteristics of Vertical-Cavity Surface-Emitting Laser

Student : Ya-Hsien Chang

Advisor : Dr. Shing-Chung Wang

Dr. Hao-Chung Kuo

Institute of Electro-Optical Engineering
National Chiao Tung University

## Abstract

The dissertation explores the improvement of high speed performance of vertical-cavity surface-emitting lasers (VCSELs) by adapting new active region, epi-structure, and fabrication process. This dissertation can be divided into three parts. In the first part, we present InGaAsP/InGaP strain-compensated MQWs VCSELs. The InGaAsP/InGaP MQWs composition was optimized through theoretical calculations and the growth condition was optimized using photoluminescence. These VCSELs exhibited superior performance with characteristics threshold currents ~0.4 mA, and the slope efficiencies ~ 0.6 mW/mA. The threshold current change with temperature is less than 0.2 mA and the slope efficiency drops less than ~30% when the substrate temperature is raised from room temperature to 85°C. High modulation bandwidth of 14.5 GHz and modulation current efficiency factor of 11.6 GHz/(mA)$^{1/2}$ are demonstrated. In the part two of this thesis, we investigate high speed performance of oxide-confined VCSELs with planar process and reduced parasitic capacitance by proton implantation. The parasitic capacitance of VCSELs was reduced using additional proton implantation. The small signal modulation bandwidth which was restricted by electrical parasitic capacitance expanded from 2.3 GHz to 9 GHz after proton implantation. To investigate the extrinsic bandwidth limitation of the oxide VCSELs, an equivalent circuit for the VCSEL impedance was introduced. The reflection coefficient showed that the electric parasitic pole exceeded 20 GHz. The eye diagram of VCSEL with reduced parasitic capacitance operating at 10Gps with 6mA bias and 6dB extinction ratio showed a very clean eye with a jitter of less than 20 ps. This simple method can be applied to mass production with low cost. In the last part, we present the improved oxide-implanted VCSELs utilizing the tapered oxide layer. The VCSELs exhibited similar static performance, but superior modulation bandwidth up to 13.2 GHz, compared with conventional blunt oxide VCSELs. The damping rate was reduced two times in the tapered oxide VCSEL and

therefore enhanced the maximal modulation bandwidth. A very clean eye was demonstrated from improved VCSEL with rising time of 26 ps, falling time of 40 ps and jitter of less than 20 ps, operating at 10Gb/s with 6mA bias and 6dB extinction ratio.

# 誌謝

博士班的生涯，充滿驚異，畢業在即，心中充滿感謝。

崔小姐等在計畫及行政作業上的幫忙。文凱、游敏與意偵，祝你們實驗順利！柏傑，希望還有機會一起打球！感謝所有曾經幫助過我的老師以及朋友們。此外，玉珠，謝謝你兩年來的陪伴。

最後，特別要感謝我的家人給我最溫馨的支持與關懷以及無怨無悔的付出，媽媽、祐榮、翔宸，謝謝你們。僅將此論文獻給他們以及我所最親愛的母親。

謝謝大家！

<div align="right">

亞衡　于 94 年 7 月 27 日

交通大學光電工程研究所

</div>

# Content

## CHAPTER 1. Introduction

## CHAPTER 2. Rate Equations and laser dynamics

## CHAPTER 3. Experimental Setup

# List of Figures

# List of Tables

# CHAPTER 1    Introduction

The surface-emitting laser is considered as one of the most important devices for short range optical communication, storage area network, and optical interconnects. In this chapter, we briefly review the history and introduce the concept of vertical-cavity surface-emitting laser from the structure of VCSELs and compare it with conventional edge emitting lasers(EEL). Then, we will discuss some important applications and future prospects.

The vertical-cavity surface-emitting laser was first proposed by Iga *et. al.* in 1979 [1], demonstrated under pulsed conditions at room temperature (RT) by the same group five years later[2], and finally continuous wave (CW) operation at room temperature was achieved in 1989 [3]. The achievements encouraged people to devote into the development of the VCSELs with different structure and novel materials. After that, VCSELs based on GaAs have been extensively studied and devices in 980, 850, and 650 nm are now commercial available. The research of InGaAsN, a key material toward 1300nm on GaAs substrate nowadays, started in mid-90 and is still improving up to now.

## 1.1 Structure of VCSELs
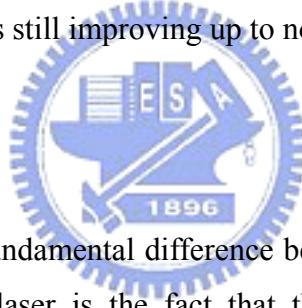
As its name indicates, the fundamental difference between an edge-emitting laser and a vertical cavity surface emitting laser is the fact that the laser oscillation as well as the out-coupling of the laser beam occur in a direction perpendicular to the epitaxial gain region and the surface of the laser chip.

The structure of most VCSELs consists of two parallel reflectors which sandwich a thin active layer, is illustrated with Figure 1-1. The reflectivity necessary to reach the lasing threshold should normally be higher than 99.5%. Together with the optical cavity formation, the scheme for injecting electrons and holes effectively into the small volume of the active region is necessary for a current injection device. The ultimate threshold current depends on how to small the active volume can be make and how well the optical field can be confined in the cavity to maximize the overlap with the active region. These confinement structures will be presented later.
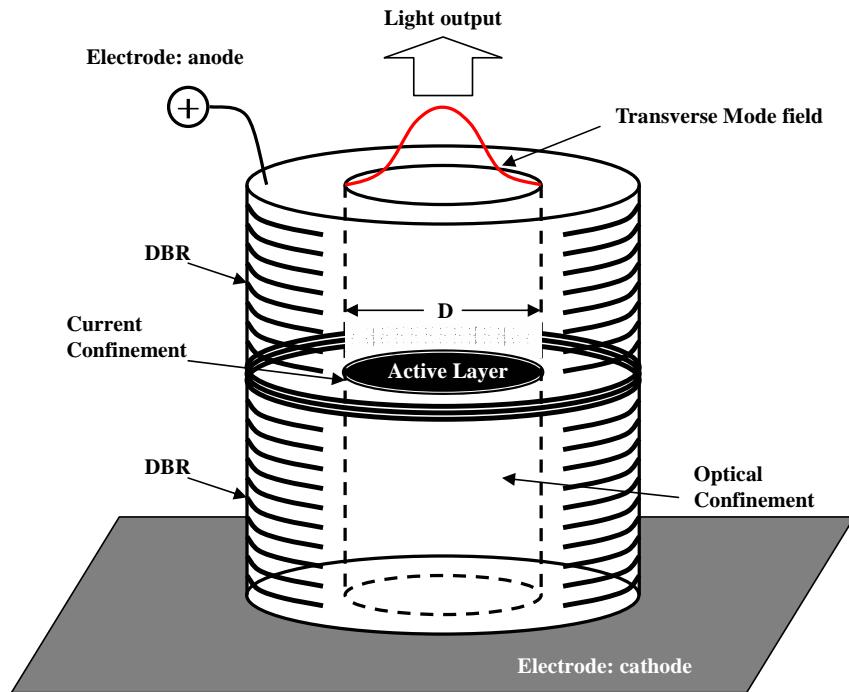
Fig. 1-1 Structure of vertical-cavity surface-emitting laser
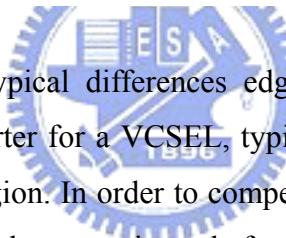
Figure 1-2 illustrates the typical differences edge-emitting laser and VCSELs. The overall cavity length is much shorter for a VCSEL, typically a few um, as opposed to some mode spacing and shorter gain region. In order to compensate for the shorter gain region, the light has to travel back and forth more times before coupled out, therefore the mirror reflectivity have to be much higher. The reflectivity of an output facet for an edge emitting laser, resulting from the change of refractive index at the cleaved interface semiconductor-air is typically around 30%. The structure parameters are listed in Table 1-1. and compared with the edge emitting lasers.
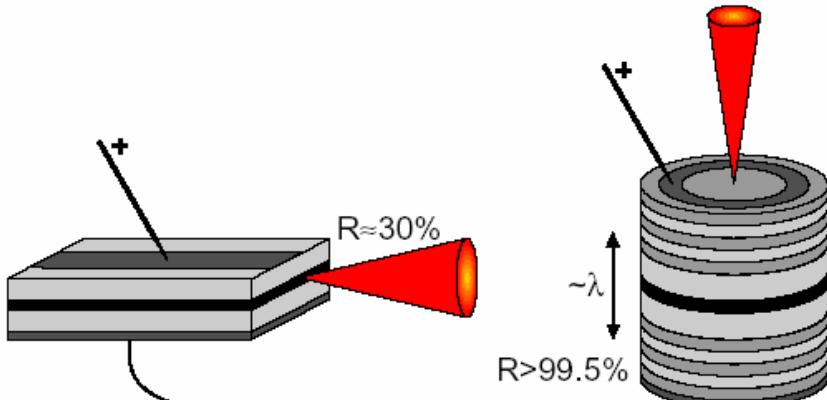


Fig. 1-2 Comparison of edge emitting laser and vertical-cavity surface-emitting laser

| Parameter | Symbol | Material | Wavelength |
|---|---|---|---|
| Active layer thickness | d | 100 Å ~ 0.1μm | 80 Å ~ 0.5μm |
| Active layer area | S | 3 x 300 μm$^2$ | 5x5μm$^2$ |
| Active volume | V | 60 μm$^3$ | 0.07μm$^3$ |
| Cavity length | L | 300 μm | ~1 μm |
| Reflectivity | $R_m$ | 0.3 | 0.99 – 0.999 |
| Optical confinement | ξ | ~ 3 % | ~ 4 % |
| Optical confinement (Transverse) | $ξ_t$ | 3 – 5 % | 50 – 80 % |
| Optical confinement (Longitudinal) | $ξ_l$ | 50 % | 2 x 1% x 3 (3 QWs) |
| Photon Life time | $τ_p4$ | ~ 1 ps | ~ 1 ps |
| Relaxation Frequency ( Low Current Levels) | $f_r$ | < 5 GHz | > 10 GHz |

Table 1-1 Comparison of parameters between stripe laser and VCSEL

## 1.2  Material for Active Region

There are some choices of the materials for semiconductor lasers in Figure 1-3. The
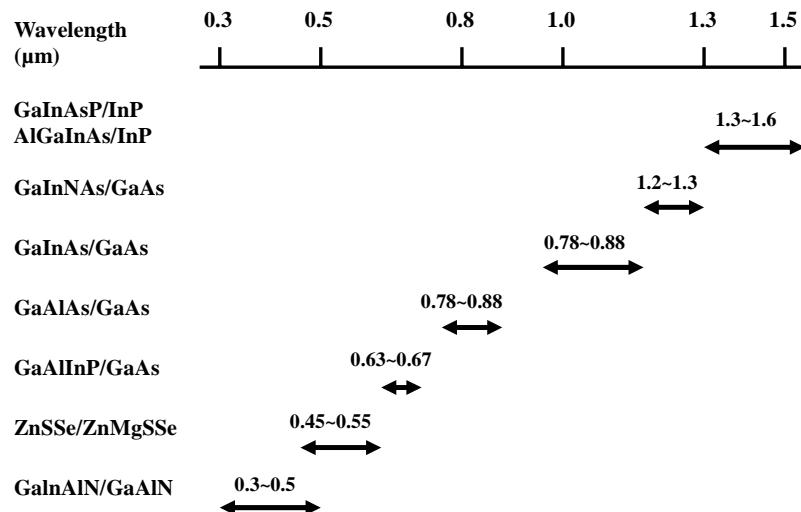


Fig. 1-3 Material for vertical-cavity surface-emitting laser in wide spectra band

availability of substrates against lattice constant related to the systems is also shown. The problems are listed below that should be taken into account consideration for making VCSELs:

▲ Design of resonant cavity and mode-gain matching

▲ Multi-layered distributed Bragg reflectors (DBRs) to realize high-reflective mirrors

▲ Heat sinking for high temperature and high power operation

In addition, the resistivity of material is crucial for high speed operation.

So far, these are mainly two methods of current confinement schemes for the VCSEL structures,

▲ Proton-implant type: An insulating layer made by proton ($H^+$) irradiation to limit the current spreading toward the surrounding area. The progress is rather simple and most commercialized devices are made by this method.

▲ Selective AlAs oxidation type: By oxidizing the AlAs layer to form an insulator.
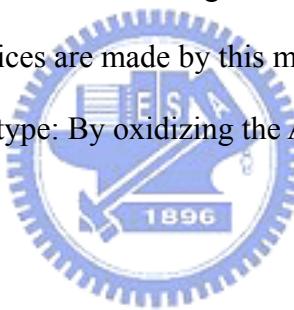
## 1.3 Advantages of VCSELs

There are many reasons why VCSELs are becoming increasing popular as light source for applications such as datacomm and optical interconnects. The monolithically integrated structure requires one single epitaxial run, making it easier to fabricate. Since the mirrors are formed during the epitaxial growth, each individual VCSEL can be tested already on the wafer, before it is cleaved into separate chips, thereby drastically reduce the production cost. The use of DBRs eliminates the risk of catastrophic optical damage (COD) in the mirrors which can occur in edge-emitters where the active material close to the facets are depleted by surface recombination and thereby light absorbing. It also reduces the risk of mechanical mirror damage. The extremely short resonator leads to a large longitudinal mode spacing that is large compared with the gain bandwidth and leads to inherent single longitudinal mode operation. The small active volume and high mirror reflectivity contribute to the very low threshold observed in VCSELs, as low as a few microamperes[4], resulting in low power

4

consumption and reduced heating of the device. This feature, combined with the absence of CODs, explains the remarkable reliability of VCSELs. Lifetimes of more than 10000 hours have been reported by several groups. [5-6]

The surface emission and the small size make it possible to fabricate very dense two-dimensional arrays of VCSELs, suitable for multi-channels parallel transmission modules. [7] VCSELs do not need to be cleaved; it is therefore possible to integrate them monolithically with other optoelectronic components such as photodetectors, modulator or hetero-bipolar transistors (HBT). [8] Because of the circular symmetry of the VCSEL structure, the light is emitted with a circular beam and very low divergence. This results in high coupling into optical fibers, up to 90% [9] and allows for relaxed tolerance in alignment, further reducing the cost of installation. For comparison, the output light emitted from an edge-emitting laser is elliptical with a transverse and lateral divergence of about 40 and 10 degrees, respectively, making it cumbersome to couple the light into an optical fiber without significant optical loss or advanced optics.

In addition, VCSELs have inherent single-wavelength structure that is well suited for wavelength engineering, making it possible to process multi-wavelength array or tuneable VCSELs. Although the manufacturing challenges are numerous, both types of devices have been demonstrated. By carefully designing the optical cavity, with the implemenatation of a small thickness variation in the bottom DBR, a record 150-wavelength VCSEL array has been reported. The thickness gradient creating a cavity thickness variation, which in turn led to laser wavelength variation, the overall wavelength span across the array being 43 nm. [10]

## 1.4 Drawbacks of VCSELs

However, VCSELS also have some drawbacks compared to edge-emitters. The manufacturing tolerances on VCSEL growth are much tighter than for edge-emitting lasers, the layer thickness having to be controlled within 1%. The major disadvantage with VCSELs is the strong tendency to operate on multiple transverse modes, due to the large transverse dimensions of the optical cavity. These results in emission spectra with multiple emission wavelengths, which limits the maximum achievable distance due to chromatic dispersion effects. Most commercial VCSEL of today operate multimode and are mainly used in short distance multimode fiber based optical data links[11], optical interconnects[12], optical storage[13] and laser printing[14]. A lot of efforts are made to produce high power single mode VCSELs. This include oxide confined VCSELs with current aperture small enough to support only the fundamental mode, index-guided structures such as regrown or surface relief

VCSELs, and spatial mode filtering in an external cavity or extended cavity. Although the first and last of these techniques have produced high single mode power they are difficult to implement with high uniformity and yield. A more reliable technique is to combine a large area oxidation with an etched shallow surface relief for mode selection. This implies only a small modification to the fabrication procedure but produces reasonably high single mode power, with high uniformity and yield. [15]

**1.5 Applications of VCSELs**

**1.5.1 Data communication**

Today, datacom moduels based on near-infrared VCSELs represent 95% of the VCSEL market, 80% of which are commercialized by a few companies: Agilent, Honeywell, Infineon, Furukawa and Zarlink. The remaining 20% are shared among numerous start-ups offering innovative designs. The market has recently exploded: it is evaluated to be worth USD 500 million at present, and is constantly growing due to the rapid deployment of Gigabit Ethernet and fiber channels. Most of today's commercial datacom components are based on oxide 850 nm VCSELS. They are often package as single component or in parallel fiber modules of linear arrays, offering 4 to 12 channels at 2.6 GB/s per channel, which aggregate bandwidth up to 30 GB/s. The research and
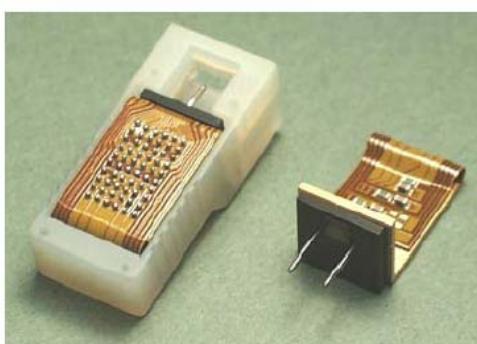


Fig. 1-4 Commercial 2.5 Gb/s VCSEL array for data communication application.

development efforts are focusing on the next generation of high speed VCSEL, and a number of groups have reported transmission at 10 GB/s or more for distances up to 300 m of MMF.   Figure 1-4 shows a 12 channel 2.5 Gb/s VCSEL array for short distance transmission applications.

For long wavelength part, Metro and Access Networks are dominated by 1300nm

and 1550 nm FP and DFB lsers up to now. A long wavelength VCSEL (LW-VCSEL) would be an ideal low-cost alternative to the DFB laser, particularly for the standard IEEE 802.3ae applications, which extend the existing Gigabit Ethernet into traditional SONET markets at OC-192 data rates.[16]. However, the performance specifications for such LW-VCSELs are challenging. For low-cost transceivers, they must operate over the 0 to 70 C temperature range for indoor applications and over the -40 to 85 C range for outdoor applications, without external temperature stabilization. The laser power launched into the single mode fiber must usually be more than 0.7 mW in order to support transmission distance of 10 km at 10 GB/s. Despite intense research effort, the technology so far has not yet met these requirements

## 1.5.2 Optical interconnect

The optical interconnect is considered by many to be inevitable in the computer technology. The performance of massively parallel computers is usually limited by the communication bottleneck between processors. Optic provides an effective mean to line these processors because of its high capacity, low crosstalk and attenuation, and the possibility to obtain three-dimensional architectures. Other potential applications include routers, switches and storage. The VCSEL is a strong candidate as the preferred optical light source for the emerging optical interconnect mass market, meeting the requirement of low cost, high density integration and low power dissipation. A 256-channel bi-directional optical interconnect using VCSELs and photodiodes on CMOS was demonstrated.[17]

## 1.5.3 Sensor

Reflective optical sensors are used to sense the presence or absence of a distant object. Examples of reflective sensors used in a variety of industrial and consumer products include barcode scanners and proximity sensors. The packaging of optical reflective sensors can be quite compact, and in the case of some LED sources, can even be packaged in a single TO can. However, a significant disadvantage to these devices is the quantity of optical crosstalk that may degrade the signal-to-noise ratio (S/N) in the detector. Crosstalk results from the fact that LEDs emit from all surfaces and the emission subtends nearly 90°. Suppliers go to great lengths to isolate the LED and the detector by using a mechanical structure to separate the optoelectronic components. In addition, the LED optical output is not easily collimated or focused to a spot to increase the amount of reflected light from a distant object. By using the technical features of the VCSEL, integrating a phototransistor in the package, and designing

the optical element into the TO can lid, an effective reflective sensor can be developed. The advantages of the sensor include the ability to package the entire assembly in a single compact TO can, along with the focusing optics and a phototransistor. Depending on the application, a single-mode or multimode VCSEL can be used. In some cases, when coherence of the optical beam is desired, the single-mode VCSEL might be the best choice, but in other cases when total output power is more important, a multimode VCSEL might be more beneficial. For example, a multimode VCSEL can be mounted on the centerline of the lens and package, and the phototransistor mounted to the side of the VCSEL. In this configuration, the optimal signal is obtained by tilting the package with respect to the centerline of the TO. The optical system is made by including a melt-formed glass lens in the TO lid. The lid can be designed to accept other lenses, and the height can be varied, which allows for the design of a wide variety of optical sensors. In addition to the reduced power consumption and single-package interface, the recurring theme in the application is the ability of the VCSEL sensor to provide higher S/N in environments where the LED sensor is not able to adequately perform. Other application areas include the sensing of diffuse reflective surfaces such as paper in a printing system, or low-reflectivity surfaces such as glasses or plastics. The small focal spot also has significant advantages in optical encoding applications such as barcode
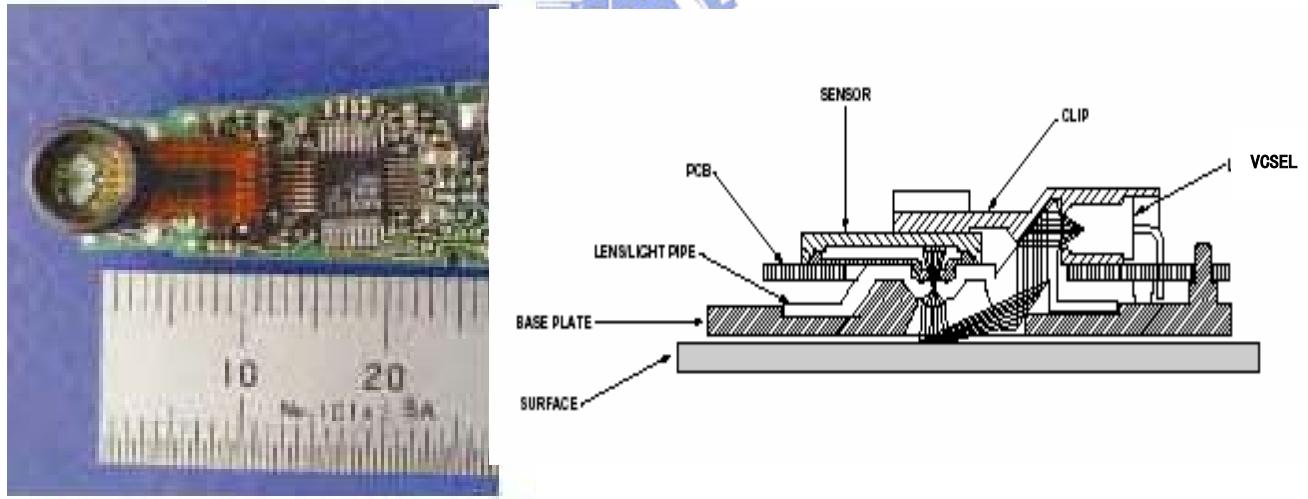


Fig. 1-5    A laser mouse module using VCSEL.

reading or positioning equipment. Figure 1-5 illustrate the VCSEL sensor module used in laser mouse application. The sensitivity and resolution of the laser mouse is 20 times higher than the conventional LED mouse. In 2004, the VCSEL based biosensor also demonstrated by C. J. Chang-Hasnain *et al*. [18-19]

# References

[1] H. Soda, K. Iga and Y. Suematsu, "GaInAs/InP surface emitting injection lasers", Jpn. J. Appl. Phys. v.18, 2329, (1979)

[2] K. Iga, Sishikawa, S. Ohkouchi and T. Nishimura, "Room temperature pulsed oscillation of GaAlAs/GaAs surface-emitting injection laser", App. Phys. Lett. v45, 348, (1984)

[3] F. Koyama, S. Kinoshita and K. Iga, "Room-temperature continuous wave lasing characteristics of GaAs vertical cavity surface-emitting lasers", App. Phys. Lett. V44, 221, (1989)

[4] G. M. Yang, M. H. MacDougal and P. D. Dapkus, "Ultralow threshold current vertical-cavity surface-emitting lasers obtained with slelective oxidation", Electron. Lett., Vol. 13. pp. 886-888, 1995

[5] J. K. Guenter, J. A. Tantum, A. Clark. R. S. Penner, R. H. Johnson, R. A. Hawthorne, J. R. Biard, Y. Liu, "Commericalisation of Honeywell's VCSEL technology:further developments", Proceedings of SPIE's Optoelectronics 2001, Vol. 4286, pp. 1-14, 2001.

[6] J. S. Span, Y. S. Lin, C. F. Li, C. H. Chang, J. C. Wu, B. L. Lee, Y. H. Chuang, S. L. Tu, C. C. Wu, "Commericailised VCSEL components fabricated at Truelight Corporation", Proceedings of SPIE's Optoelectronics 2001, Vol. 4286, pp. 15-21, 2001.

[7] A. V. Krishnamoorthy, K. W. goossen, L. M. F. Chirovsky, R. G. Rozier, P. Chandramani, S. P. Hui, J. Lopata, J. A. Walker, L. A. D'Asaro, "16x16 VCSEL array flip-chip bonded to CMOS VLSI circuit", IEEE Photon. Technol. Lett., Vol. 12, pp. 1073-1075, 2000

[8] U. Eriksson, P. Evaldsson and K. Streubel. "A novel technology for monolithic integration of VCSELs and heterojunction bipolar transistors at 1.55um", CLEO Pacific Rim '97, Chiba, Japan, paper PD2.8, 1997

[9] K. Tai, G. Hasnain, J. D. wyn, R. J. Fisher, Y. H. Hang, B. Weir, J. Gamelin and A. Y. Cho, "90% coupling of top surface-emitting GaAs/AlGaAs quantum well laser output into 8 um diameter core silica fiber", Electron. Lett., Vol. 26, pp. 1628-1629, 1990

[10] M. Y. Li, W. Yuen, G. S. Li and C. J. Chuang-Hasnain, "Top-emitting micromechanical VCSEL with a 31.6nm tuning range", IEEE Photon. Technol. Lett., Vol. 10, pp. 18-20, 1998

[11] U. Fiedler, G. Reiner, P. Schnitzer and K. J. Ebeling, "Top surface-emitting vertical-cavity laser diode for 10GB/s data transmission", IEEE Photon. Technol. Lett., Vol. 8, pp. 746-748, 1996

[12] M. W. Haney, M. P. Christensen, P. Milojkovie, J. Ekman, P. Chandramani, R. Rozier, F. Kiamilev, Y. Liu and M. Hibbs-Brenner, "Multichip free-space global optical

interconnection demonstration with integrated arrays of vertical-cavity surface-emitting lasers and photodetectors", Appl. Opt., Vol. 38, pp. 6190-6200, 1999

[13] K. Goto, "Proposal for ultrahigh density optical disk system using a vertical cavity surface emitting laser array", Jpn. J. Appl. Phys., Vol. 37, pp. 2274-2278, 1998

[14] R. L. Thornton, "Vertical-cavity lasers and their application to laser printing", Proc. SPIE, Vol. 3003, pp. 112-119, 1997

[15] H. Martinsson, J. A. Vukusic, M. Grabherr, R. Michalzik, R. Jager, K. J. Ebeling and A. Larsson, "Transverse mode selection of large-area oxide-confined vertical-cavity surface-emitting laser using a shallow surface relief", IEEE Photon. Technol. Lett., Vol. 11, pp. 1536-1538, 1999

[16] http://grouper.iee.org/groups/802/3/ae/index.html

[17] D.V. Plant, M. B. Venditti, E. Laprise, J. Faucher, K. Razavi, M. Chateauneuf, A. G. KirK, J. S. Ahearn, "256-channel bi-directional optical interconnect using VCSELs and photodiodes on CMOS", J. Lightwave Techno. 19(8) 1093, 2001

[18] F. Mateus, M. C. Huang, Univ. of California/Berkeley; P. Li, B. Cunningham, SRU Biosystems; C. J. Chang-Hasnain, "High sensitivity label-free biosensor using VCSEL" , Proceedings of SPIE's BIOS 2004 vol. 5328-22, 2004.

[19] D. Kumar, H. Shao, Kevin Lear, "Dependence of vertical cavity surface emitting laser diodes with integrated micro-fluidic channels on fluid refractive index" Optical Information systems II in series Proceedings of SPIE, vol. 5557, Aug 2004

## Chapter 2　Rate Equations and laser dynamics

The rate equations provide the most fundamental description of the laser. It describes the time-evolution of carrier- and photon densities in a laser cavity as a function of the pump rate, material gain and parameters associated with the material properties and laser construction. In its simplest form, it consists of a pair of coupled nonlinear differential equations Eq.(2-1), one for the carrier density, and one for the photon density. Therefore it is well suited for modeling simulation. By this technique, many of properties of VCSELs can be investigated in this paper.

$$
\begin{cases}
\dfrac{dN(t)}{dt} = \dfrac{\eta_i I(t)}{qV_a} - v_g S(t)G(N,S) - \dfrac{N(t)}{\tau_N} \\[2mm]
\dfrac{dS(t)}{dt} = \Gamma v_g S(t)G(N,S) + \beta \dfrac{N(t)}{\tau_N} - \dfrac{S(t)}{\tau_S} \\[2mm]
G(N,S) = g_0 \dfrac{N(t) - N_{tr}}{1 + \varepsilon S(t)}
\end{cases}
\tag{2-1}
$$

The phase does not enter into Eq.(2-1), since the optical power does not depend on the phase, it depends on the optical magnitude only. However, some effects are highly related to the laser phase, such as mode locking, injection locking and polarization switching, etc, in this situation, the phase has to be taken into account. Before proceeding further, it is important to clear up the fundamental mechanisms and assumption in the rate equations, such as stimulated and spontaneous emission, stimulated absorption, non-radiative recombination, and so on. When referring to "carriers", the ambipolar assumption is applied, that means there is no difference between electrons and holes.

### 2.1 Carrier Rate Equation

The rate of change of the electrons (or holes) density comes from electron-hole generation and recombination. And these changes must be related to the number of photons produced (for a direct bandgap semiconductor). We assume that the electrons and holes remained confined to the active region having volume $V_a$. It is intuitive to obtain the basic form of carrier rate equation:

$$\frac{dN}{dt} = \text{Generation - Recombination}$$

$$= \text{Pump} - \begin{pmatrix} \text{Stimulated emission} \\ -\text{ Stimulated absorption} \end{pmatrix} - \text{Spontaneous recombination} - \begin{array}{c} \text{Non -} \\ \text{radiative recombination} \end{array}$$

$$= Ginj - Rstim - Rspon - Rnonr$$

(2-2)

where *Ginj* is pumping energy, *Rstim* is stimulated recombination which is the difference between stimulated emission and stimulated absorption, *Rspon* is spontaneous emission, and *Rnonr* is non-radiative recombination. In Figure 2.1, it shows all the individual terms contribute to the carrier rate equation. Now, we will carefully examine each term as the section proceeds.

**Carrier Rate Equation**
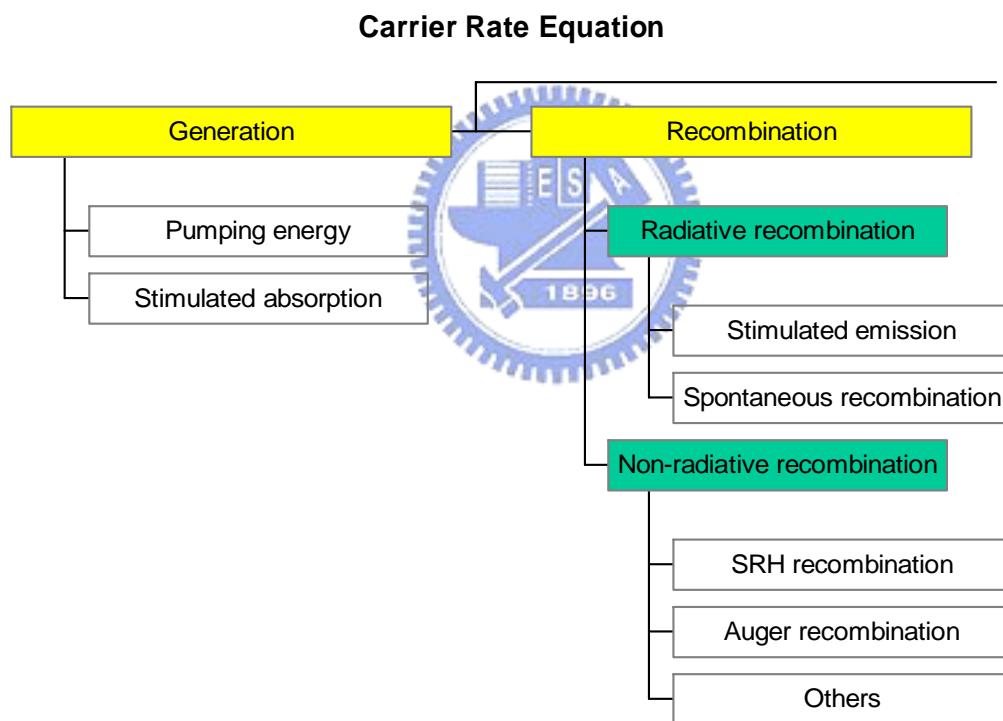


Fig 2.1    The individual terms considered by general carrier rate equation.

### 2.1.1    Pumping Energy

The pump consists of either bias current or optical flux. The pump term describes the density of electron-hole pairs produced in the active volume $V_a$ in each second, which is given by

$$Ginj = \frac{\eta_i I(t)}{qV_a} \qquad (2\text{-}3)$$

where $Ginj$ is pumping current density per second (carriers/cm$^3$/ sec), $\eta_i$ is injection efficiency or internal quantum efficiency (ideal is 1), $I(t)$ is injection current per second, $q$ is the elementary charge which changes the units from coulombs to the "number of electrons". Pump increases the number of electrons and holes in the conduction band (CB) and valence band (VB), respectively, is shown in Figure 2.2.



before                                        after
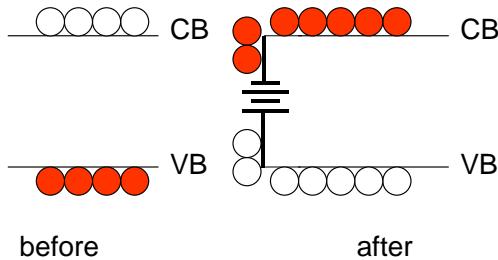
Fig. 2.2   The continuous pumping is the essential condition to reach population inversion.

The injection efficiency $\eta_i$ represents the fraction of injected current that flow into the active region. In practical, due to the surface leakage or other carrier loss mechanisms, the $\eta_i$ is always less than 1, it is defined by

$$\eta_i \equiv \frac{\text{carriers in active region}}{\text{total injected carriers in the device}} \qquad (2\text{-}4)$$

### 2.1.2   Stimulated absorption and stimulated emission

The reason we discuss stimulated absorption and emission in the same section is due to their interaction will be used to present the concept of gain medium, it is the major part of laser device ( recall laser = *Light Amplified by the Stimulated Emission of Radiation* ). Both of stimulated absorption and stimulated emission results from stimulated recombination, therefore, need photons to conduct its process (see Figure 2.3). In contrast, the spontaneous emission does not need photons to conduct its process, will be discussed in next section(2.1.3). According to their various physical mechanisms, please refer to [1][2][3] for further explanation, again, the main purpose of this paper is to demonstrate how to build up a device model based on well-known electro-optics theory. In the simplest way to merge stimulated absorption and recombination mechanisms into to rate equations is to understand the stimulated absorption process would decrease photons number and electron-hole pairs increased.

On the opposite, the stimulated recombination process would multiple increase photons (photons amplified) and electron-hole pairs decreased, that's why the pumping current should maintain in a certain level to keep the emission process continuously in the active region.

Stimulated absorption                           Stimulated emission

before              after              befor              after
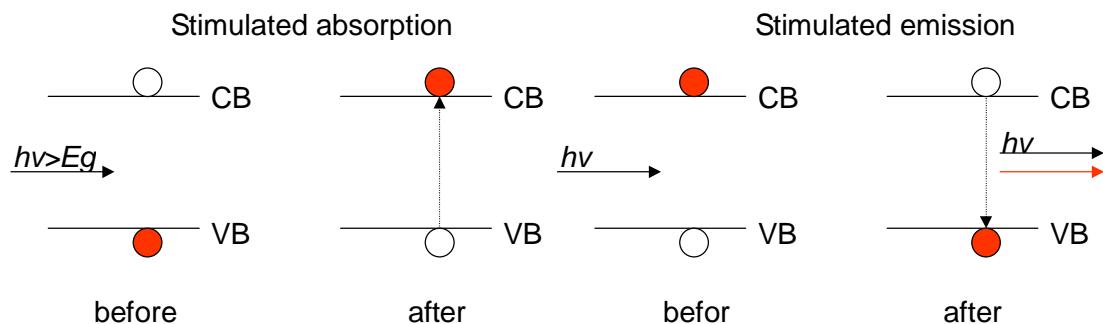
Fig. 2.3    Stimulated absorption generates more electron-hole pairs. Stimulated emission produced coherent light (same energy, phase, propagation direction, highly monochromatic).

The term *Rstim* is stimulated recombination which is the difference between stimulated emission and stimulated absorption, usually, the stimulated recombination produces more photons than them absorbed (this is one of the essential conditions for lasing, otherwise, the gain will be less than one, no amplified). The Figure 2.4 shows single photon incident on the left side of the gain medium. This photon enters the material and interacts with the carriers. Some of the processes emit photons (stimulated emission) while some of them absorb photons (absorption or sometimes called stimulated absorption) and some do nothing. It implies the gain is the ratio of output photons over the input photons. The gain describes here only the stimulated emission and absorption processes and does not include photon losses through the side of the laser or through the mirrors.
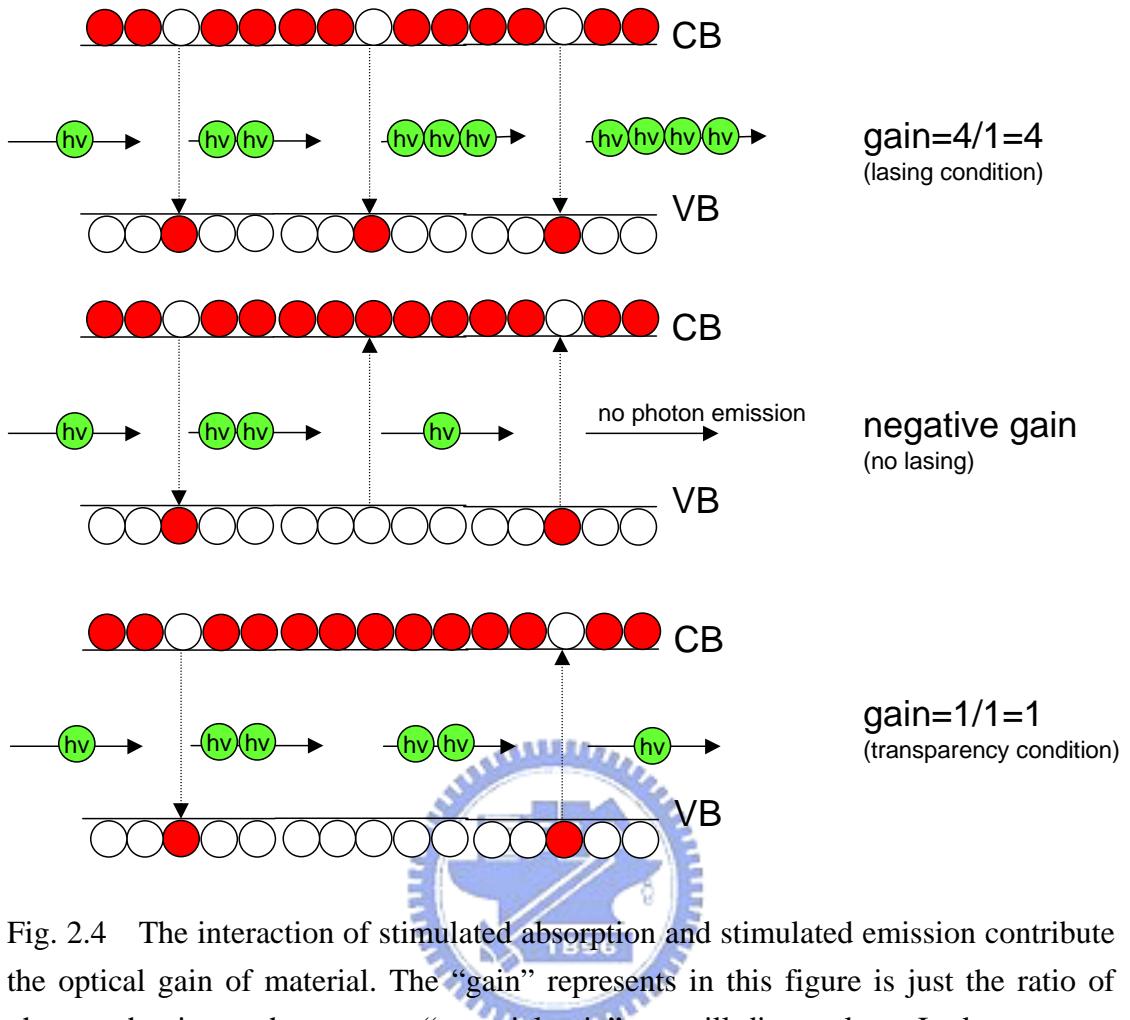
Fig. 2.4 The interaction of stimulated absorption and stimulated emission contribute the optical gain of material. The "gain" represents in this figure is just the ratio of photons that is not the same as "material gain" we will discuss later. It also presents the gain is the function of photons traveling length.

The lower one of Figure 2.4 brings up one terminology, called "material transparency". The semiconductor material becomes "transparent" ("material transparency") when the rate of stimulated absorption just equals the rate of stimulated emission. One incident photon produces exactly one photon in the output. The transparency density $N_{tr}$ (number per unit volume) represents the number of excited carriers per volume required to achieve transparency. The material gain required to achieve lasing will be much larger than zero since the gain must offset other losses besides stimulated absorption (typically G=150 cm$^{-1}$ ). The relation between material gain and carrier density is depicted in Figure 2.5. This yields the simplest expression of material gain:

$$G(N) = g_0(N - N_{tr}) \quad (2\text{-}5)$$

where $g_0$ is linear gain coefficient or differential gain at $N_{tr}$, $N_{tr}$ is transparency density. In this case, we assume the photon density S is not high. Therefore, the gain curves can be approximated by a straight line at $N_{tr}$ (refer to Figure 2.5).

When photon density is high enough, the factor $(1 + \varepsilon S)$ is taken into account. This factor accounts for nonlinear gain saturation, where $\varepsilon$ is gain suppression coefficient. This yields another material gain expression:

$$G(N, S) = g_0 \frac{N(t) - N_{tr}}{1 + \varepsilon S(t)} \qquad unit : cm^{-1} \qquad (2\text{-}6)$$

In general, Eq.(2-6) is more practical than Eq.(2-5) in most case, however, we use Eq.(2-6) in our model.
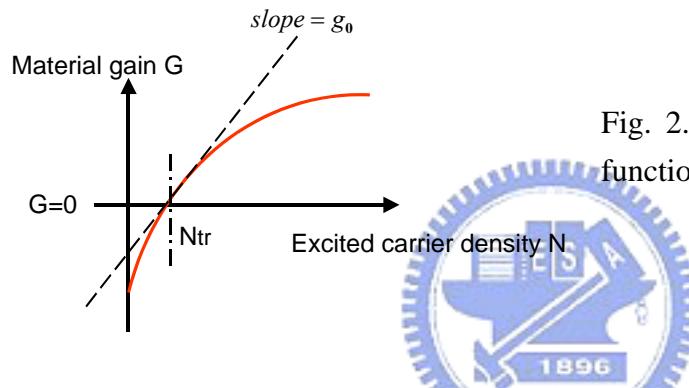


Fig. 2.5 The material gain (G) is as function of carrier concentration (N).

Let's recall the beginning of this section and combine with the concept of material gain, the expression of Stimulated recombination *Rstim* can be generated:

$$Rstim = \text{Stimulated emission - Stimulated absorption}$$

$$= G(N, S) \times S \qquad unit: \frac{1}{length} \times \frac{1}{volume}$$

$$= G(N,S) \times S \times v_g \qquad unit: \frac{1}{time} \times \frac{1}{volume} \qquad (2\text{-}7)$$

where $v_g$ is the group velocity of light (cm/sec). By substituting Eq.(2-6) into Eq.(2-7), we obtain

$$Rstim = g_0 \frac{N(t) - N_{tr}}{1 + \varepsilon S(t)} \times S(t) \times v_g \qquad (2\text{-}8)$$

### 2.1.3   Spontaneous recombination

Spontaneous recombination refers to the recombination of holes and electrons without an applied optical field (i.e., no incident photons -- see Figure 2.6). Spontaneous recombination produces photons by reducing the number of electrons in the conduction band and holes in the valence band. Due to it is a bimolecular recombination events, the recombination rate is proportional to "np", it can be written as Eq.(2-9) by ambipolar assumption (n=p).

$$Rspon = BN^2 \tag{2-9}$$

where $B$ is proportionality constant.

Spontaneous recombination
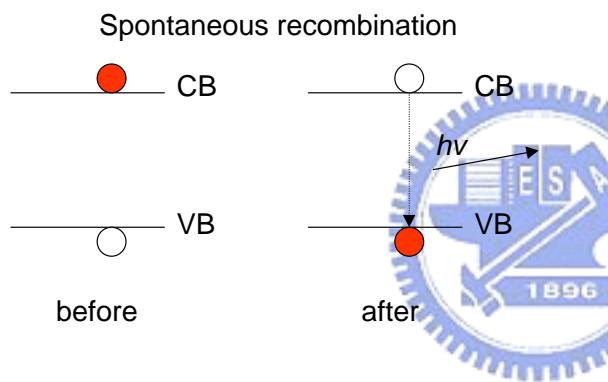


Fig. 2.6   Spontaneous recombination emits incoherent light in all directions which is a random process.

The spontaneous emission initiates laser action but decreases the efficiency of the laser. The number of photons in the lasing mode increases not only from stimulated emission but also from the spontaneous emission. Let's see how this happens. Excited carriers in the gain medium spontaneously emit photons in all directions. The wavelength range of spontaneously emitted photons cannot be confined to a narrow spectrum. Figure 2.7 compares the typical spectra for spontaneous and stimulated emission (for GaAs). Some of the spontaneously emitted photons propagate in exactly the correct direction to enter the waveguide of the laser cavity. Of those photons that enter the waveguide, a fraction of them have exactly the right frequency to match that of the lasing mode. This small fraction of spontaneously emitted photons adds to the photon density $S$ of the cavity is given as:

$$Fraction\ of\ Rspon = \beta BN^2 \tag{2-10}$$

where $\beta$ is spontaneous recombination coefficient.
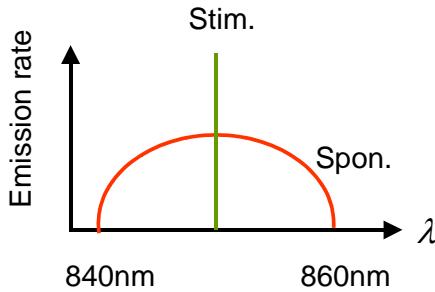
Fig. 2.7 Comparing spectra for spontaneous and stimulated emission.

### 2.1.4 Non-radiative recombination

There are two recombination mechanisms play the major roles for non-radiative recombination(see Figure 2.8). One is Shockly-Read-Hall(SRH) recombination when an electron falls into a "trap", an energy level within the bandgap caused by the presence of a foreign atom or a structural defect. Once the trap is filled it cannot accept another electron. The electron occupying the trap, in a second step, falls into an empty valence band state, thereby completing the recombination process. One can envision this process as a two-step transition of an electron from the conduction band to the valence band or as the annihilation of the electron and hole, which meet each other in the trap. In Shockley-Read-Hall recombination, carriers are captures in trap states in the bandgap. The trap states may be created by deep level impurities (metals or transition metals) or by radiation or process induced defects (vacancies, interstitials, antisites or dislocations). We can treat SRH recombination is a monomolecular recombination and the recombination rate is proportional to " n or p", giving

$$R_{SRH} = AN \tag{2-11}$$

where $A$ is proportionality constant.
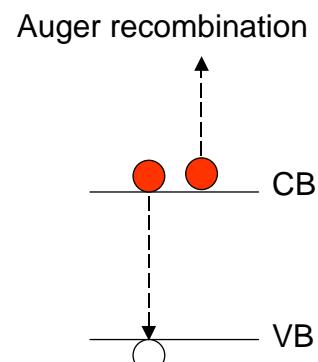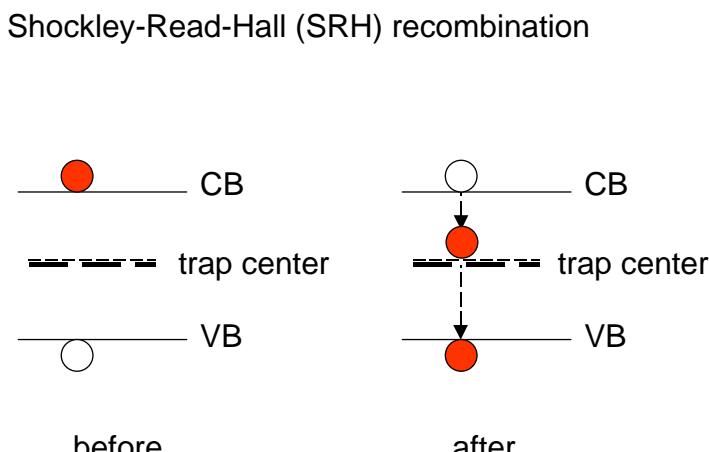


Fig. 2.8 Two non-radiative recombination mechanisms.

18

Another one is Auger recombination (see Figure 2.8). It involves three particles: an electron and a hole, which recombine in a band-to-band transition and give off the resulting energy to another electron or hole. The involvement of a third particle affects the recombination rate so that we need to treat Auger recombination differently from band-to-band recombination. Non-radiative Auger recombination where an electron-hole recombination instead of emitting a photon, moves a third carrier (electron or hole) to a higher energy. The third carrier dissipates its energy by heating the crystal via phonon emission. We can treat Auger recombination rate is proportional to " nnp ", giving

$$R_{Auger} = CN^3 \tag{2-12}$$

where $C$ is proportionality constant. By combining (2-10) and (2-11), yields

$$Rnonr = R_{SRH} + R_{Auger} = AN + CN^3 \tag{2-13}$$

By substituting Eq.(2-3),(2-8),(2-9) and (2-12) into Eq.(2-2) and organize all the terms, obtain carrier rate equation as:

$$\frac{dN}{dt} = Ginj - Rstim - Rspon - Rnonr \tag{2-14}$$

$$= \frac{\eta_i I(t)}{qV_a} - g_0 \frac{N(t) - N_{tr}}{1 + \varepsilon S(t)} \times S(t) \times v_g - BN^2 - (R_{SRH} + R_{Auger})$$

$$= \frac{\eta_i I(t)}{qV_a} - g_0 \frac{N(t) - N_{tr}}{1 + \varepsilon S(t)} \times S(t) \times v_g - BN^2 - (AN + CN^3)$$

$$= \frac{\eta_i I(t)}{qV_a} - g_0 \frac{N(t) - N_{tr}}{1 + \varepsilon S(t)} \times S(t) \times v_g - (AN + BN^2 + CN^3)$$

$$= \frac{\eta_i I(t)}{qV_a} - g_0 \frac{N(t) - N_{tr}}{1 + \varepsilon S(t)} \times S(t) \times v_g - \frac{N}{\tau_N}$$

by defining equivalent carrier lifetime $\tau_N^{-1} \equiv (A + BN + CN^2)$. It implies the carrier lifetime contains the information of spontaneous recombination and non-radiative recombination.

If lasers made with "good" material, $R_{SRH}$ term can be neglected. Also, $R_{Auger}$ term is important for lasers (such as InGaAsP) with emission wavelengths larger than 1μm

(small bandgap). For comparison, GaAs lasers generally emit between 800 to 860 nm. If we restrict our attention to GaAs then $R_{Auger}$ term can be neglected. We will usually rewrite Eq.(2-10) as:

$$Fraction \ of \ Rspon = \beta BN^2 \cong \beta \frac{N}{\tau_N} \tag{2-15}$$

### 2.1.5   Photon Rate Equation

Many of the processes that decrease the carrier density $N$ in the active volume $V_a$ must also increase the photon density $S$ in the modal volume $V_m$. Figure 2.9 shows all the individual terms contribute to the photon rate equation.
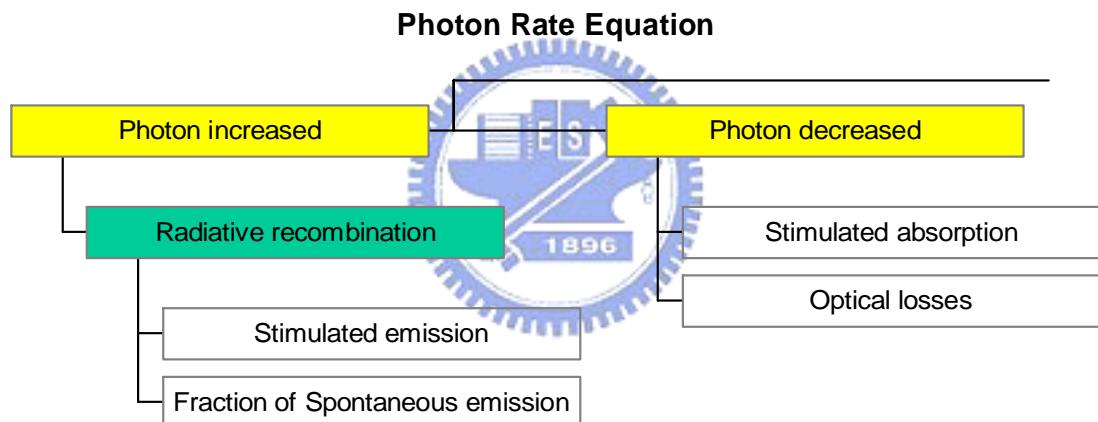


Fig. 2.9    The individual terms considered by general photon rate equation.

We can therefore write a photon rate equation as:

$$\frac{dS}{dt} = \text{radiative recombination} - \text{photon decrease} \tag{2-16}$$

$$= \left( \begin{array}{c} \text{Stimulatede emission} \\ + \text{Fraction of spontaneous emission} \end{array} \right) - \left( \begin{array}{c} \text{Stimulated absorption} \\ + \text{optical losses} \end{array} \right)$$

$$= \left( \begin{array}{c} \text{Stimulatede emission} \\ - \text{Stimulated absorption} \end{array} \right) + \text{Fraction of spontaneous emission} - \text{optical losses}$$

$$= \Gamma(Rstim + Fraction \ of \ Rspon) - Optical_{loss}$$

where the optical confinement factor $\Gamma$ specifies the fraction of the optical mode that overlaps the gain region (active region). In other words, the confinement factor gives the percentage of the total optical energy found in the active region $V_a$, it can be expressed as $\Gamma = V_a / V_m$.

The term $Optical_{loss}$ describes the changes of the photon density in each second by optical loss mechanisms, such as light scattering through the sidewall, free carrier absorption, mirror loss, etc, is given by

$$Optical_{loss} = (\alpha_{int} + \alpha_m)S \qquad\qquad unit: \frac{1}{length} \times \frac{1}{volume} \qquad (2\text{-}17)$$

$$= (\alpha_{int} + \alpha_m)v_g S \qquad\qquad unit: \frac{1}{time} \times \frac{1}{volume}$$

$$= \frac{S}{\tau_s}$$

By defining $\tau_s^{-1} = (\alpha_{int} + \alpha_m)v_g$, where $\tau_s$ is photon lifetime, $\alpha_{int}$ is internal loss due to sidewalls or free carrier absorption, $\alpha_m$ is mirror loss ( both top and bottom mirrors), given

$$\alpha_m = \frac{1}{L}\ln(\frac{1}{\sqrt{R_1 R_2}}) \qquad\qquad (2\text{-}18)$$
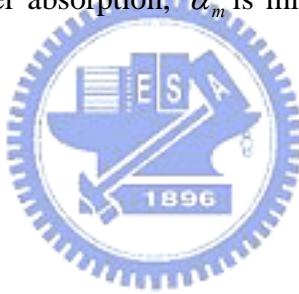
where $L$ is cavity length, $R_1$ and $R_2$ are the reflectivity of top and bottom mirrors, respectively.

By substituting Eq.(2-8),(2-15) and (2-17) into Eq.(2-16) and organize all the terms, obtain photon rate equation as:

$$\frac{dS}{dt} = \Gamma(Rstim + Fraction\ of\ Rspon) - Optical_{loss} \qquad (2\text{-}19)$$

$$= \Gamma(g_0 \frac{N(t) - N_{tr}}{1 + \varepsilon S(t)} \times S(t) \times v_g + \beta \frac{N}{\tau_N}) - \frac{S}{\tau_s}$$

here the $R_{SRH}$ and $R_{Auger}$ are neglected.

For convenience, let's write the carrier rate equations Eq.(2-14) and photon rate equation Eq.(2-19) together, given Eq.(2-20) as:

Carrier injection | Stimulated recombination | Spontaneous recombination +Non-radiative recombination

$$\begin{cases} \dfrac{dN(t)}{dt} = \dfrac{\eta_i I(t)}{qV_a} - v_g S(t) g_0 \dfrac{N(t) - N_{tr}}{1 + \varepsilon S(t)} - \dfrac{N(t)}{\tau_N} \\[4mm] \dfrac{dS(t)}{dt} = \Gamma v_g S(t) g_0 \dfrac{N(t) - N_{tr}}{1 + \varepsilon S(t)} + \Gamma \beta \dfrac{N(t)}{\tau_N} - \dfrac{S(t)}{\tau_S} \end{cases} \quad (2\text{-}20)$$

Stimulated emission | Spontaneous emission | Optical losses

Eq.(2-20) is same as Eq.(2-1). It represents the general laser rate equation with all the terms and associated phenomena. It can help us to simulate the static-state and dynamic properties of VCSELs. However, the capability of Eq.(2-20) is limited due to it does not take spatial consideration into account.

Marc Xavier Jungo have proposed spatiotemporal model of VCSELs in 2003 which is a 2D, multimode, time-domain model, given in Eq.(2-21). Many of VCSELs properties can be investigated in his theoretical research [4].

$$\begin{cases} \dfrac{\partial N(r,\theta,t)}{\partial t} = \dfrac{\eta_i I(r,\theta,t)}{qV_a} - v_g \sum_m S_m(r,\theta,t) G_m(N,S_m) - \dfrac{N(r,\theta,t)}{\tau_N} + D_N \nabla^2 N(r,\theta,t) \\[4mm] \dfrac{\partial S(r,\theta,t)}{dt} = \Gamma_m v_g S_m(r,\theta,t) G_m(N,S_m) + \Gamma_m \beta_m \dfrac{N(r,\theta,t)}{\tau_N} - \dfrac{S_m(r,\theta,t)}{\tau_{S_m}} \\[4mm] G_m(N,S_m) = g_0 \dfrac{N(r,\theta,t) - N_{tr}}{1 + \dfrac{\varepsilon}{\pi R^2} \displaystyle\int_{-\pi}^{\pi} \int_0^R S_m(r,\theta,t) r\, dr\, d\theta} \end{cases} \quad (2\text{-}21)$$

where $D_N$ is ambipolar diffusion coefficient, the suffix $m$ represents the related parameters for $m^{th}$ mode. In generally, there are several modes contribute to laser's intensity. Each mode has its own frequency and optical profile. They play a very important role for coupling properties and other practical applications. The multimode behavior of VCSELs is dominated by the interaction of spatially inhomogeneous carrier diffusion and optical field distribution which can't be represented in Eq.(2-20). The radial and azimuthal distribution (2D) of carriers and photons for individual mode are considered in Eq.(2-21). It accounts for the phenomenon of inhomogeneous distribution of carriers and photons in the active layer and help us to understand how the spatial hole burning (SHB) and multimode operations to affect the static and

dynamic properties of VCSELs. However, Eq.(2-20) is still very important for one to know how to build up the models of VCSELs base on the theory of lasers phenomenology. Due to the understanding of general laser rate equations, one can easily to translate it to Eq.(2-21). Regarding the exact mathematical derivation and formulation of the core model as well as of the advanced mechanisms can be found in [4].

## 2-2 Small signal modulation

### 2-2-1 Transfer function

Under small signal modulation, the carrier and photon density rate equation, are used to calculate relaxation resonance frequency and its relationship to laser modulation bandwidth.

Consider the application of an above-threshold DC current, $I_0$, carried with a small AC current, $I_m$, to a diode laser. Illustration is, shown in Figure 2-5, under basic L-I characteristics (Light output power versus current). The small modulation signal with some possible harmonics of the drive frequency, $\omega$. Small signal approximation, assumes $I_m \ll I_0$ bias and spontaneous emission term, $\beta$, is neglected, is expressed as

$$I = I_0 + I_m(t) = I_0 + I_m(\omega)e^{j\omega t}$$

$$n = n_0 + n_m(t) = n_0 + n_m(\omega)e^{j\omega t} \tag{2-22}$$

$$n_p = n_{p0} + n_{pm}(t) = n_{p0} + n_{pm}(\omega)e^{j\omega t}$$

Before applying these equations, the rate equation is rewritten for the gain. Assumption under DC current is sufficiently above threshold that the spontaneous emission can be neglected. Without loss of generality, we suppose full overlap between the active region and photon field, $\Gamma = 1$; furthermore, internal quantum efficiency, $\eta_i$, is neglected. That is,

$$\frac{dn}{dt} = \frac{I}{qV} - \frac{n}{\tau} - g_0(n - n_{tr})n_p \tag{2-23}$$

$$\frac{dn_p}{dt} = g_0(n - n_{tr})n_p + \beta R_{sp} - \frac{n_p}{\tau_p} \tag{2-24}$$

substitute Eq. (2-8) into Eq. (2-9)

$$\frac{d(n_0 + n_m)}{dt} = \frac{(I_0 + I_m)}{qV} - \left(\frac{n_0 + n_m}{\tau}\right) - g_0(n_0 + n_m - n_{tr})(n_{p0} + n_{pm})$$

$$= \left(\frac{I_0}{qV} - g_0(n_0 - n_{tr})n_{p0} - \frac{n_o}{\tau}\right) + \left(\frac{I_m}{qV} - g_0(n_0 - n_{tr})n_{pm} - an_{p0}n_m - \frac{n_m}{\tau}\right)$$

for this, it is similarly expressed modulation terms as

$$\frac{dn_m}{dt} = \frac{I_m}{qV} + g(n_0)n_{pm} - g_0 n_{p0} n_m - \frac{n_m}{\tau} \tag{2-25}$$

$$\frac{dn_{pm}}{dt} = g_0 n_{p0} n_m + g(n_0)n_{pm} - \frac{n_{pm}}{\tau_p} \tag{2-26}$$

The small signal terms in frequency domain of carrier and photon are given by

$$n_m(t) = n_m(\omega)e^{j\omega t}$$

$$n_{pm}(t) = n_{pm}(\omega)e^{j\omega t}$$

substitute into Eq. (2-25) and (2-26), the equations become

$$j\omega n_m(\omega)e^{j\omega t} = \frac{I_m(\omega)e^{j\omega t}}{qV} + g(n_0)n_{pm}(\omega)e^{j\omega t} - g_0 n_{p0} n_m(\omega)e^{j\omega t} - \frac{n_m(\omega)e^{j\omega t}}{\tau}$$

Carrier modulation term in frequency domain is simplified as

$$j\omega n_m(\omega) = \frac{I_m(\omega)}{qV} + g(n_0)n_{pm}(\omega) - g_0 n_{p0} n_m(\omega) - \frac{n_m(\omega)}{\tau}$$

$$\left( j\omega + g_0 n_{p0} + \frac{1}{\tau} \right) n_m(\omega) = \frac{I_m(\omega)}{qV} + g(n_0)n_{pm}(\omega) \tag{2-27}$$

Photon modulation term in frequency domain is simplified as

$$j\omega n_{pm}(\omega) = g_0 n_{p0} n_m(\omega) + g(n_0)n_{pm}(\omega) - \frac{n_{pm}(\omega)}{\tau_p}$$

$$\left( j\omega - g(n_0) + \frac{1}{\tau_p} \right) n_{pm}(\omega) = g_0 n_{p0} n_m(\omega) \tag{2-28}$$

Solve for $n_m(\omega)$ and $n_{pm}(\omega)$ using Eq. (2-27) and (2-28), we obtain the frequency response of two arranged equations as below

$$n_m(\omega) = \left( \frac{j\omega}{j\omega\Omega - \omega^2 - \omega_r^2} \right) \left( \frac{I_m(\omega)}{qV} \right) \tag{2-29}$$

$$\tag{2-30}$$

where $n_{pm}(\omega) = \left( \frac{\tau_p \omega_r^2}{j\omega\Omega - \omega^2 - \omega_r^2} \right) \left( \frac{I_m(\omega)}{qV} \right)$

$$\omega_r^2 = (2\pi \cdot f_r)^2 = \left( \frac{n_{p0}}{\tau_p} \right) g_0 \quad \ldots\ldots\text{Relaxation frequency} \tag{2-31}$$

$$\tag{2-32}$$

$$\Omega = \frac{1}{\tau} + n_{p0} g_0 \quad \ldots\ldots\text{Damping constant (decay rate)}$$

With the Eq. (2-29) and (2-30) we observe the coupling between the small signal photon, $n_{pm}$, and carrier, $n_m$. Small signal carrier injection induces photon achieved oscillation. This phenomenon produces a natural resonance in the laser cavity which shows up the output power of the laser in response to sudden changes in the input current. The natural frequency of oscillation associated with this mutual dependence between $n_m$ and $n_{pm}$. Modulation response is expanded the small signal modulation

relationship to steady-state. From Eq. (2-29) and (2-30), the modulation response is denoted as

$$M(\omega) = \left| \frac{n_{pm}(\omega)}{n_{pm}(0)} \right| = \left| \frac{\dfrac{\tau_p \omega_r^2}{j\omega\Omega - \omega^2 - \omega_r^2}}{\dfrac{\tau_p \omega_r^2}{\omega_r^2}} \right| = \left| \frac{\omega_r^2}{j\omega\Omega - \omega^2 - \omega_r^2} \right|$$

(2-33)

Modulation bandwidth is determined as cutoff frequency, $f_c$, which is the position with half response written as

$$M(\omega_c) = \frac{1}{2}M(0) = \frac{1}{2} \frac{\omega_r^2}{\left[ \left(\omega_c^2 - \omega_r^2\right)^2 + \omega_r^2 \Omega^2 \right]} = \frac{1}{2}$$

(2-34)

for $\omega_r^2\Omega^2 \ll (\omega_c^2 - \omega_r^2)^2$, the cutoff frequency, $\omega_c$, is approximated to $\sqrt{3}\,\omega_r$.

Transfer function, $H(\omega)$, is the identical term in Eq. (2-25) and (2-26) respectively obtained with Cramer's rule. It is similar to modulation response, $M(\omega)$, describing the response of the laser intensity to small variations in the drive current through the active region. That is,

$$H(f) = C \frac{f_r^2}{f_r^2 - f^2 + j\dfrac{f}{2\pi}\gamma}$$

(2-35)

where $f_r$ is the resonance frequency same as Eq. (2-31), $\gamma$ is the damping rate similar to Eq. (2-32), and C is a constant. Accounting for additional extrinsic limitations due to carrier transport and parasitic elements related to the laser structure results in an extra pole in the small signal modulation transfer function

$$H(f) = C \left( \frac{f_r^2}{f_r^2 - f^2 + j\dfrac{f}{2\pi}\gamma} \right) \cdot \left( \frac{1}{1 + j\dfrac{f}{f_p}} \right)$$

(2-36)

where $f_p$ is the cutoff frequency of the low pass filter characterizing the extrinsic limitations. It is crucial for microwave applications that the modulation bandwidth of the VCSEL is sufficiently large so that efficient modulation is achieved as the modulation frequency.

## 2.3 Relative Intensity Noise (RIN)

The measurement of relative intensity noise (RIN) describes the laser's maximum available amplitude range for signal modulation and serves as a quality indicator of laser devices. RIN can be thought of as a type of inverse carrier-to-noise-ratio measurement. RIN is the ratio of the mean-square optical intensity noise to the square of the average optical power:

$$RIN = \frac{<\Delta P^2>}{P^2} \ dB/Hz \qquad (2\text{-}36)$$

where $<\Delta P^2>$ is the mean-square optical intensity fluctuation (in a 1-Hz bandwidth) at a specified frequency, and $P$ is the average optical power. It is more convenient to define RIN per unit bandwidth because the measurement bandwidth can vary under different experimental conditions. As defined, RIN is measured in dB/Hz.

Relative intensity noise measurements represent the alternative technique used for studies of high-speed dynamics in semiconductor lasers. Like modulation response technique described above this approach allows for determining of $dG/dn$ and $K$-factor through numerical fitting procedure. However, the signal measured is not response to the external modulation of the bias current but noise spectra of the laser itself. This noise power is associated with the fluctuation of the concentrations in photon and electron systems caused by spontaneous light emission events. Deviation of the electron and photon densities from equilibrium values leads to their damped oscillations with the frequency of electron-phonon resonance and damping factor. Hence, the measurements of the laser noise power spectra at different bias currents provide enough information to determine such important laser parameters as differential gain and $K$-factor.

Small signal analysis applied to the rate equations, but taking into account internal noise source and transport of carriers leads to the following expression for the spectral dependence of the RIN:

$$RIN = \frac{4}{\pi} \ \delta f_{st} \frac{f^2 + (\gamma/2\pi)^2}{(f_r^2 - f^2)^2 + f^2(\gamma/2\pi)} \qquad (2\text{-}37)$$

where - $\delta f_{st}$ - Schawlow-Townes linewidth and * $g$ - differs from $g$ in denominator due to carrier transport through the active region of modern MQW laser .

The main advantage of the RIN technique with respect to modulation response measurements is the elimination of the problem by high frequency modulation experimental equipment. At the same time, low level of the noise for high quality lasers makes it is necessary to use low noise preamplifiers. Also, there is no low

frequency rolloff in the RIN spectra, which is related to the carrier capture and diffusion across SCH time.

**References**

1. BAHAA E. A. SALEH, MALVIN CARL TEICH, " Fundamentals of Phtonics," John Wiley & Sons, Inc., 1991.
2. Siu Fung Yu, " Analysis and design of vertical cavity surface emitting lasers," John Wiley & Sons, Inc., 2003.
3. Govind P. Agrawal, Niloy K. Dutta, "Semiconductor lasers," 2nd edition, AT & T, 1993.
4. Marc Xavier Jungo, " Spatiotemporal VCSEL Model for Advanced Simulations of Optical Links," Hartung-Gorre Verlag Konstanz, 2003.

# CHAPTER 3    Experimental facility and setup

## 3.1 Inductively coupled plasma reactive ion etching

The ICP etching equipment was a planar ICP-RIE system (SAMCO ICP-RIE 101iPH) as shown in Figure 3-1. The ICP main system is consisted of the source chamber and plasma chamber. The source chamber is constructed with RF generation and matching unit including vacuum pumping system, gas transportation system, and cooling water system.

### (1) Plasma source system

The ICP power and bias power source with RF frequency were set at 13.56 MHz. The output RF power introduce into the tornado coil through impedance match and RF power transmission line. The high density plasma was formed by the tornado coil using the theory of inductively coupled plasma.

The tornado coil was fixed in the source chamber connecting with ground, and the source chamber has the electromagnet field shielding effect. Between the source chamber and plasma chamber, there is the quartz window to be as the separation.
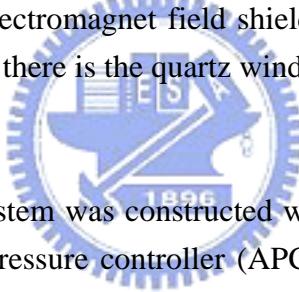
### (2) Vacuum pumping system

The vacuum pumping system was constructed with mechanical pump and turbo pump. There is a automatic pressure controller (APC) between the plasma chamber and pump. It could control the pumping rate by tuning the throttle inside the APC. The throttle and the pressure meter on the plasma chamber assemble a feedback control system.

### (3) Gas transportation system

Gas transportation system controls the flow rate of the gas source by the mass flow controller (MFC) and the entering of the gas source is decided by a control valve. The MFC and control valve can control the flux and time of the gas source. During the experiment, the pressure of the plasma chamber is set by tuning the APC and the MFC which control the flow rate of the gas source.

### (4) Cooling water system

During the experiment, some equipment must be continuously cooling and sure to be normal operating to prevent the damage, for example the RF generation and turbo pump. And the source chamber and plasma chamber should not be too hot; they also need to remove the heat by the circulating of the cooling water system.

**(5) Wafer transportation system**

In the lab, the load lock chamber is set for keeping the high vacuum of the plasma chamber and enhances the convenience of the operation. The wafer transportation system contains the load lock chamber, the gate valve, the transportation arm.

**3.2 Ion implantation system**

The basic requirement for an ion-implantation system is to deliver a beam of ions of a particular type and energy to the surface of a wafer. Figure 3-2 shows a schematic view of a medium-energy ion implanter. Following the ion path, we begin with the left-hand-side of the system with the high-voltage enclosure containing many of the system components. A gas source feeds a small quantity of source gas such as $BF_3$ into the ion source where a heated filament causes the molecules to break up into charged fragments. This ion plasma contains the desired ion together with many other species from other fragments and contamination. An extraction voltage, around 20 kV, causes the charged ions to move out of the ion source into the analyzer. The pressure in the remainder of the machine is kept below at $10^{-6}$ Torr to minimize ion scattering by gas molecules. The magnetic field of the analyzer is chosen such that only ions with the desired charge to mass ratio can travel through without being blocked by the analyzer walls. Surviving ions continue to the acceleration tube, where they are accelerated to the implantation energy as they move from high voltage to ground. Apertures ensure that the beam is well collimated. The beam is then scanned over the surface of the wafer using electrostatic deflection plates. The wafer is offset slightly from the axis of the acceleration tube so that ions neutralized during their travel will not be deflected onto the wafer. A commercial ion implanter is typical 6m long, 3m wide, and 2m high, consumes 45 kW of power, and can process 200 wafers per hour (dose $10^{15}$ ions/cm$^2$).

Three quantities define an ion implantation step: the ion type, energy, and dose. Given an appropriate source gas, the ion type is determined by magnetic field of the analyzing magnet. In a magnetic field of strength B, ions of charge Q move in a circle of radius R, where

$$RB = \frac{M_1 v}{Q} = \sqrt{\frac{2M_1 V}{Q}}$$

(3-1)

where V is the ion velocity and V is the source extraction voltage. The magnetic field is adjusted so that R corresponds to the physical radius of the magnet for the desired

ion. It is possible for other ions to be accepted if they have a similar value for M1/Q, but since the source provides ions with decrease the beam current. The selected ions are accelerated to the implantation energy by the voltage applied to the acceleration tube.

The total number of ions entering the target per unit area is called the dose. If the current in the ion beam is I, then for a beam swept over an area A, the dose Φ is given by

$$\Phi = \frac{1}{QA}\int I dt$$

(3-2)

where the integral is over time t. Completing the circuit between target and on source allows the current to be measured. For an accurate current reading, care must be taken to recapture secondary electrons emitted from the target by incident ions. A Faraday cage around the target, at a small positive bias voltage collects this charge so that it can be included. Wafers frequently patterned surface layers of silicon dioxide, which is a good insulator. Implantation can charge up insulated regions of the surface high enough for dielectric breakdown to occur, which damages the materials. If the wafer is not well grounded, charging of the whole wafer can distort the ion beam. To avoid this effect, a low-energy election beam can be directed onto the target surface during implantation. The electrons are drawn to charging regions where they neutralize the charge buildup.

Any implantation machine has design limits to its energy range. The minimum implantation energy is usually set by the extraction voltage, which cannot be reduced too far without drastically reducing beam current. Some special machines can operate in a deceleration mode, in which ions are extracted with a normal voltage but then slowed down in a reverse-biased "acceleration" tube resulting in energies as low as 5 KeV. A more common technique uses implants of molecular ions containing the required dopant, for example, $BF_2^+$ ions could be implanted at 30 KeV. When the molecule hits the target surface it immediately breaks up into its components, and the energy is divided according to the relative masses. In this case, we would have one 7 keV boron atom and two 11 keV fluorine atoms. The resulting profiles are the same as if 7 keV boron and 11 keV fluorine had been directly implanted, because the binding energy of the molecule is negligible compared to the implantation energy. If channeling is significant, the profiles will be different from that of 7 keV boron alone because the addition of fluorine will increase the lattice damage and reduce channeling. The fluorine distribution is shallower than the boron distribution, so ions can still enter channels when they have traveled past the fluorine peak. Fluorine has only a small effect on annealing and on electrical mobility in the final device.

The maximum implantation energy is set by the design of the high-voltage

31

equipment. The only way to circumvent this is to implant a multiply-charged ion such as $B^{++}$. This ion would receive twice the energy of $B^+$ from the same accelerating potential, effectively doubling the energy of the machine. The price paid is a reduced beam current since the number of $B^{++}$ ions in the source plasma is much smaller.



$$Cl_2 + e^* \rightarrow 2Cl + e^-$$

$$Ar + e^* \rightarrow Ar^+ + 2e^-$$

$$GaN + nCl \rightarrow GaCl_{3(s)} + NCl_{3(s)}$$
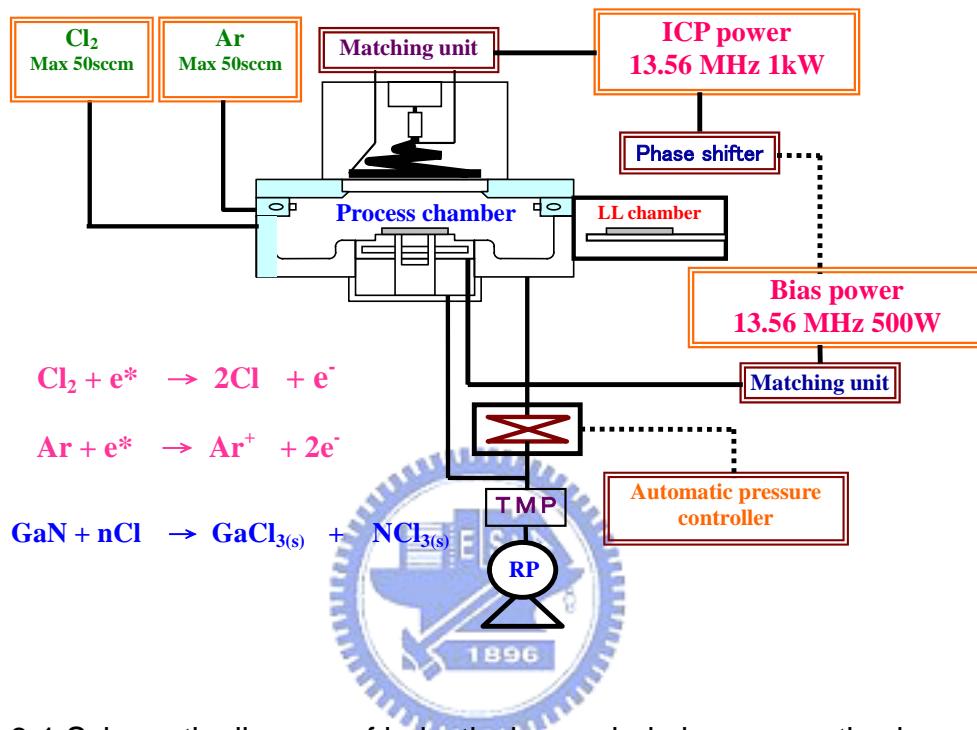
Fig. 3-1 Schematic diagram of inductively coupled plasma reactive ion
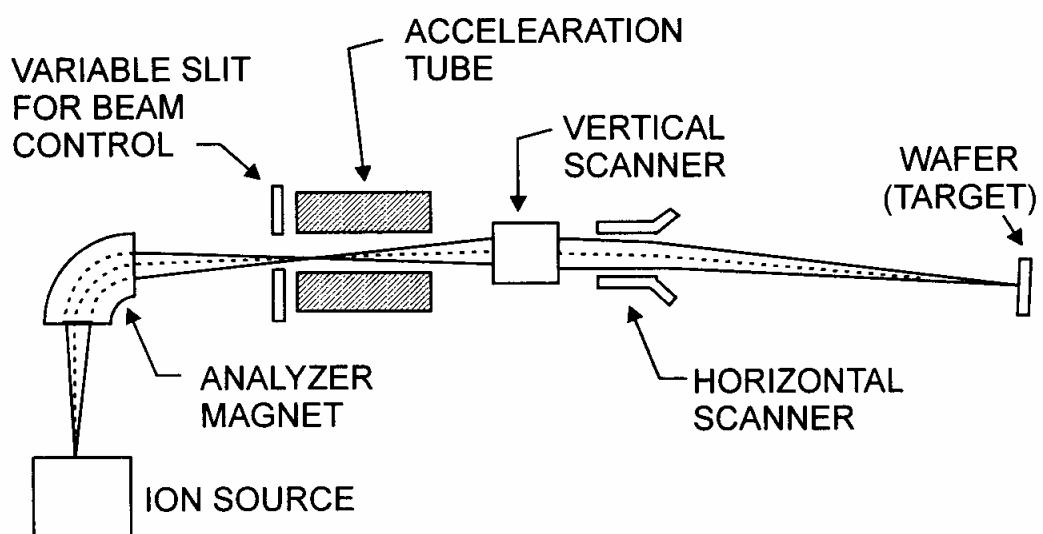


Fig. 3-2 Schematics diagram of a typical commercial ion-implantation

## 3.3 Oxidation process

Fabrication of selectively oxidized monolithic VCSEL is determined by the layer compositions, and thus the oxidation rates, such that specific oxide layers near the laser cavity have a greater lateral extent to define an oxide aperture. The oxidation selectively to Al composition is exploited to fabricate the buried oxide layers within a VCSEL: With minute changes in Ga concentration, one or more AlGaAs layers are induced to oxidize more rapidly and thus form buried oxide layers for electrical and optical confinement. The selectively oxidation process begins with the deposition of electrical contacts. A silicon nitride mask is deposited and patterned on the wafer top to encapsulate the metal contact and to form an etch mask. Dry etching, such as
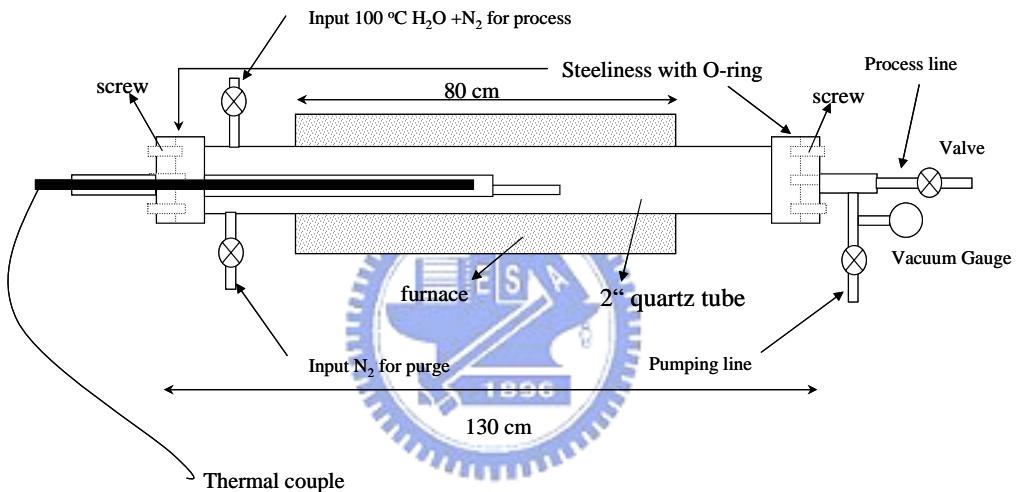


Fig. 3-3 Schematics of oxidation furnace setup.

reactive ion etching, is used to define mesas or holes to expose the oxidation layers. Oxidation process was performed in furnace under $400^{o}C \sim 450^{o}C$, as shown in Figure 3-3. For mesa structures, the oxide aperture is formed by oxide layer extending from the edge into the center of the mesa, as shown in Figure 3-4. For etched hole planar structures, the aperture is formed by the overlap of oxides that extend outward from each hole. The lateral oxidation extent of a layer within the etched mesa or surrounding the etched hole is controlled by the composition of the layer and the oxidation time. Typically, an oxidation temperature of 440 $^{o}$C produces a oxidation rate of approximately 1 μm/min for the $Al_{0.98}Ga_{0.02}As$ layers. After oxidation the nitride mask is removed to permit laser testing.

The oxidation front of an oxide aperture within a VCSEL mesa is shown is Figure 3-5. For a given oxidation time and thus lateral extent of oxidation, variation of the oxide aperture area within a sample can be obtained using differing mesa sizes or

separation between the etched holes. For mesa-etched oxide structures, planarization can be accomplished using polyimide as a backfill or an airbridge technology can be used to allow deposition of metal interconnects. A planar hole oxide structures, but electrical isolation between VCSELs must still be accomplished by some technique such as stacked ion implantation.
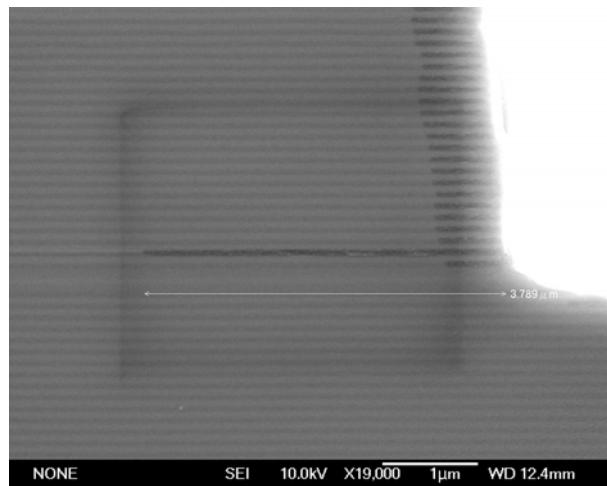


Fig. 3-4 SEM image of cross section of oxidized VCSEL.
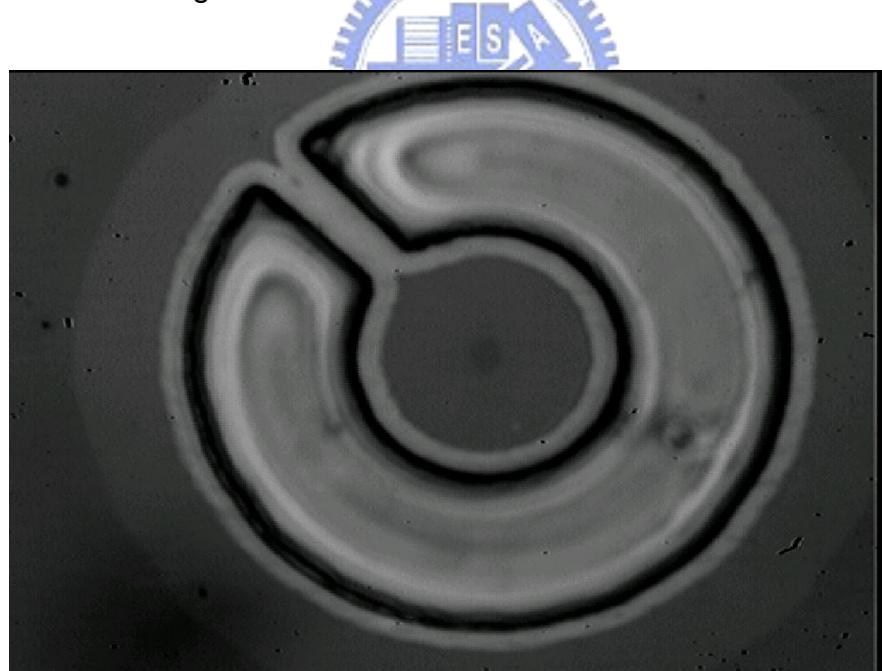


Fig. 3-5 Optical microscope image of top view of oxidized VCSEL.

## 3-4 Probe station and spectrum measurement system

Probe station system was essential instrument for basic device characteristics measurement such as I-L (current versus light output), I-V (current versus voltage). Scheme of probe station system, as illustrated in Figure 3-6, include probe station, current source, and power-meter module. Keithley 238 supplies continuous current for diode laser and receives relative voltage synchronously. The laser was temperature controlled by a precise thermoelectric controller and the output power was measured by Newport power-meter module (model 1835C). An integration sphere was used to pick up whole emitting power from VCSEL to improve the accuracy of power measurement. The integration sphere was calibrated with 850nm, 1300nm, and 1550nm and all the measured values can be traced to NIST standard.

The VCSEL device was placed on a platform of the probe station and was injected bias current with a microprobe. Threshold condition, slope efficiency, turn-on voltage and differential resistance can be obtained from L-I-V information by sweeping bias current. Emission spectrum was measured by optical spectrum analyzer (OSA, Advantest 8381). A multi-mode fiber probe was placed close to the emission aperture to take optical spectra. The OSA had spectrum resolution of 0.1nm which was adequate to measure VCSEL lasing spectra. Scheme of spectrum measurement system was combined with probe station as Figure 3-6.
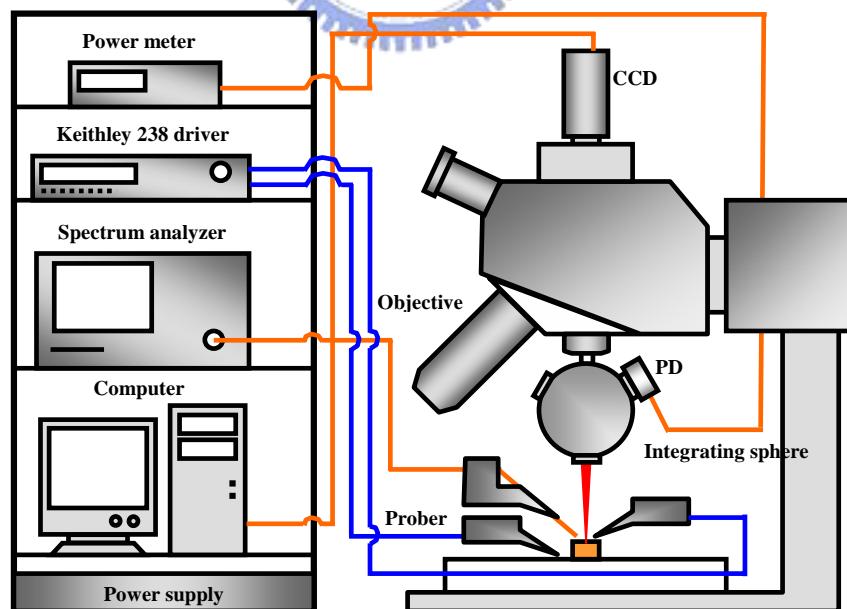


Fig. 3-6 Probe station measurement instrument setup

## 3-5 Far-field and near-field
Near-field pattern (NFP) of VCSELs was magnified by high resolution optics

and projected into a B/W CCD then digitized by computer. Beam-view analyzer is useful software we used for the image process of the NFP. We could obtain NFP image under threshold, as spontaneous emission, to define oxide aperture size. Far-field angle measurement was achieved by scanning the detector cross the laser emission, as shown in Figure 3.7, and recording the intensity with angle simultaneously. A stereo microscope was installed to assistant the wafer-level far-field test.
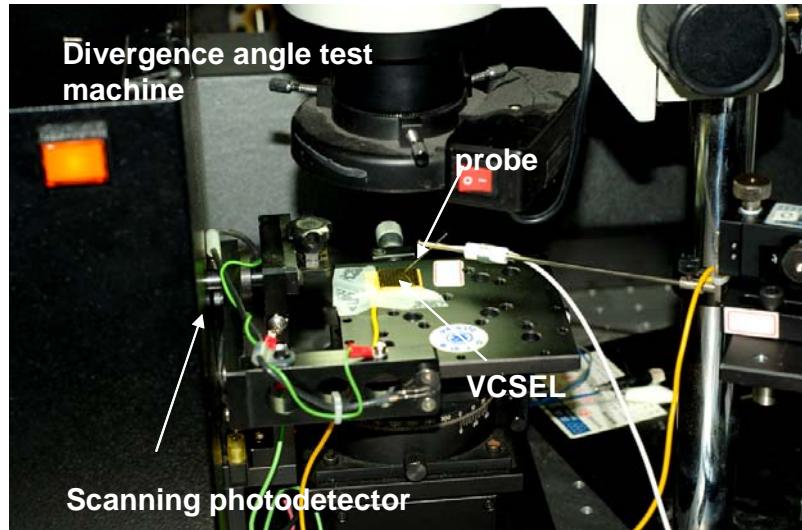


Fig. 3-7 Photograph of far-field measurement setup

## 3-6  Microwave test system

### 3.6.1 Setup

The microwave test system was mainly consisted of network analyzer, optical platform and microwave probe, as illustrated with Figure 3-8. Agilent 8720ES network analyzer was a crucial instrument of this microwave measurement. Transmitter of network analyzer produced -10dBm RF signal. Laser diode drivers (Newport, model 525) provided direct bias current to set the laser above the threshold. Bias-Tee combined AC and DC signal transmission through the same coaxial cable. The mixed signal was transmitted through the coplanar microwave probe and was injected into VCSEL, which was bonded on RF submount, as Figure 3-9. The coplanar microwave probe had 700μm pitch (ground (G) to signal (S) tip spacing) and suitable measurement frequency range was up to 40 GHz. Signal probe was higher than ground tips. Fine probing was observed by signal probe skating on contact substrate. Illustration of microwave probe holder in whole was shown in Figure 3-10.

Optical platform contained microscope, beam splitter, objective and fiber coupler etc. We used a long work distance objective (20X, Mitutoyo), fixed in a triple-divide translation stage, to pick up the laser output from VCSEL. Light was separated by

beam splitter and received by CCD and another 10X objective lens(Olympus). One of splitting light was received by a simplified microscope, which was constructed by beam splitter and a CCD to make probing easily. Another light path trough 10X objective coupling into multimode fiber by five-axis fiber aligner (Newport).

The collected light was transmitted into 12 GHz photodetector (Model 1580, NewFocus) and was conversed into electrical signal and fed to network analyzer. Comparing two channels microwave signal by network analyzer, information of transmission and reflection characteristics could be expressed as vector (magnitude and phase), scalar (magnitude only), or phase-only quantities, that was, S-parameter.
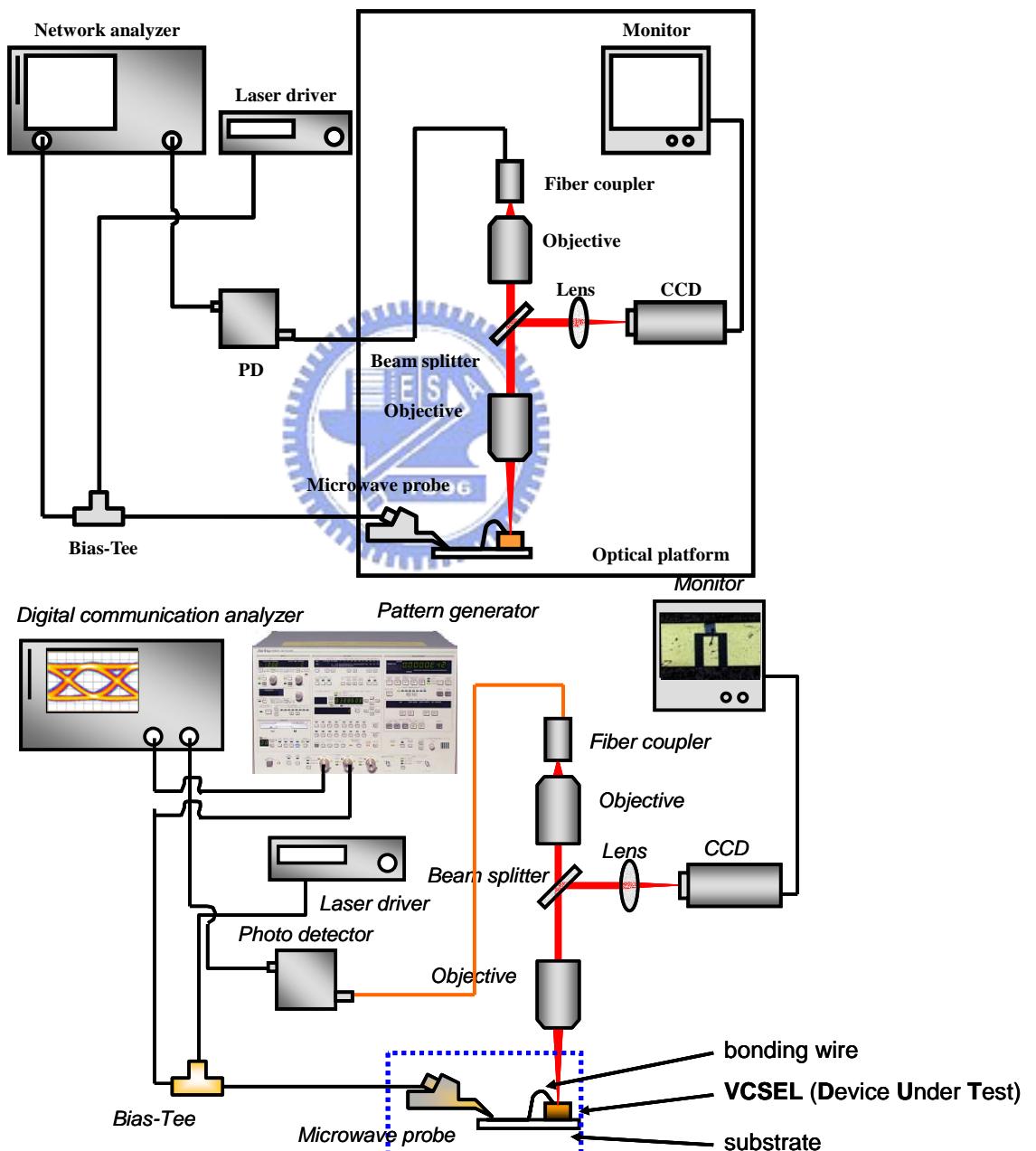
Fig. 3-8 Microwave test system setup

**OM vertical view image**

**Bonding wire**

**VCSEL**

**Au**

**AlN**

1521μm

1050μm    279μm    456μm
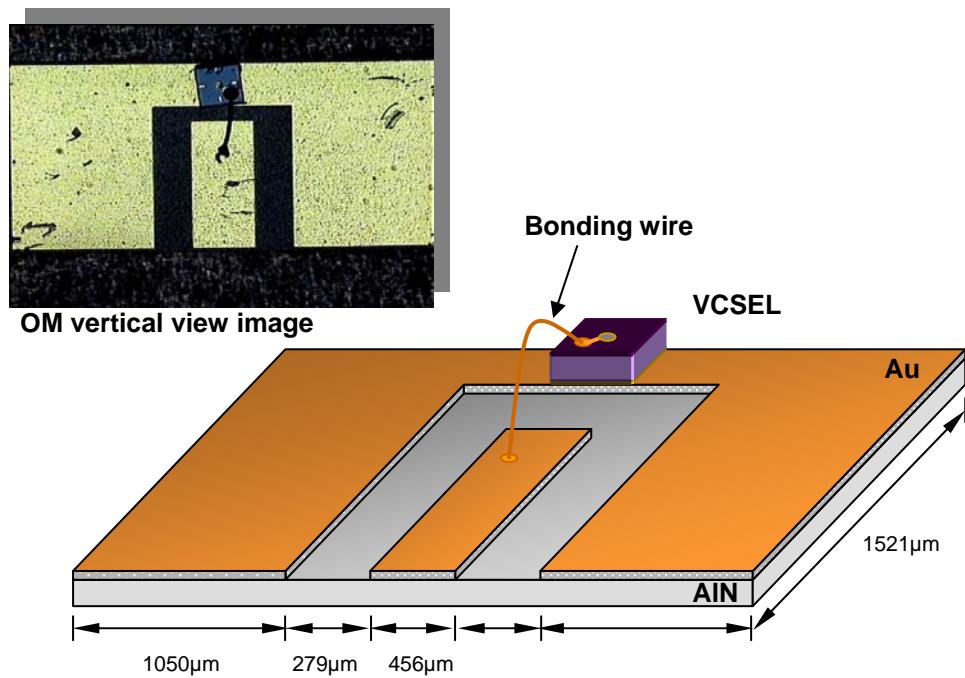
Fig. 3-9 Sub-mount substrate design



**Network analyzer**

**Laser driver**

**Photodetector**

**Optical platform**

**Microwave probe**
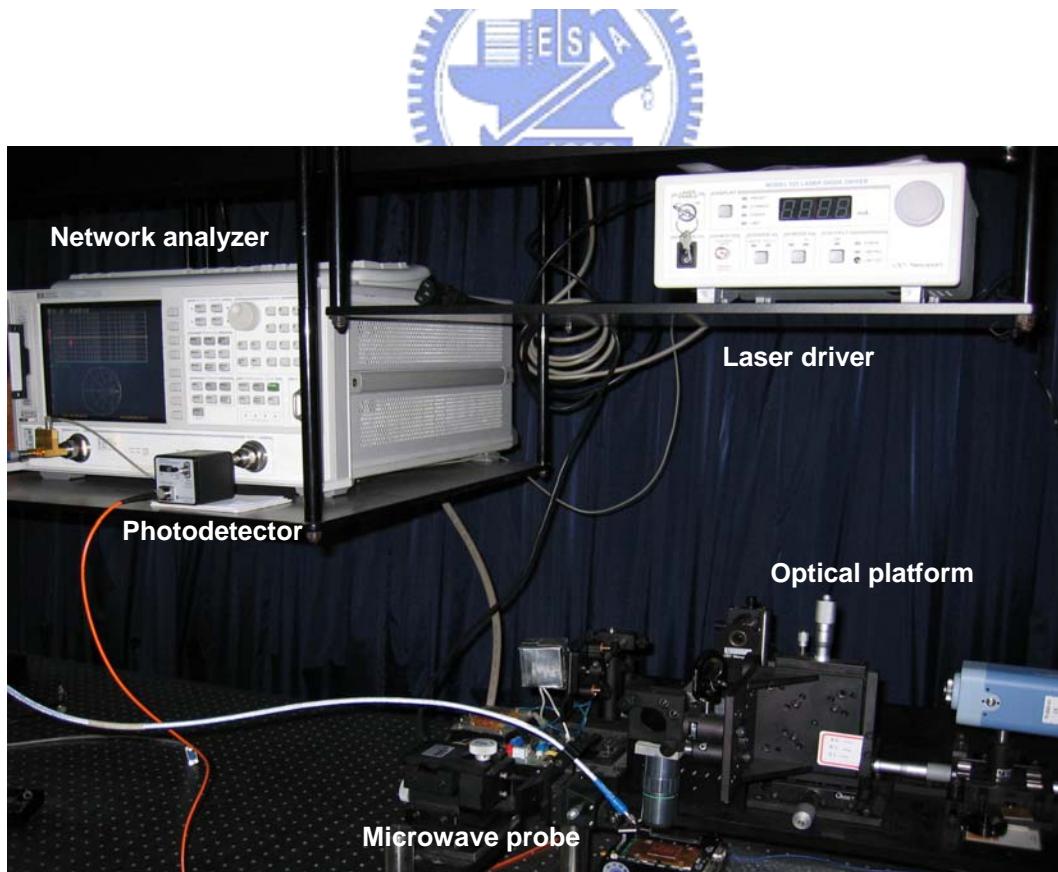
Fig. 3-10 Illustration of microwave test system

**3.7 Relative Intensity Noise measurement**

The experimental setup of RIN is shown in Figure 3-11. The laser was driven by a low noise current source and was temperature controlled by a precise thermoelectric controller. The laser output was collimated and focused by two objective lenses. A beam splitter guided ~ 5% of the laser light into an image-formation lens then the image was recorded by a CCD camera. A multimode fiber was coated with Al thin film on one facet with reflectivity of 10%. The fiber was held by a 5-axises precision fiber positioner and the coated facet was taken as the reflecting mirror. The reflected beam was collimated and re-focused back to the emission aperture of the VCSEL. The tilt of fiber- facet was carefully aligned and formed an external cavity between the top DBR of VCSEL and the fiber-facet. Size of reflected spot can be controlled by the Z-axis of the positioner while the overlapping between the reflected spot and emission aperture was controlled by tilt of the positioner. The external cavity length was about 28 cm. Mirror M1 guide the laser to a fast photodetector (PD, Newfocus 1601) and its output is coupled to a 0.5 GHz oscilloscope (Agilent Infinium) to exam the stability of laser. The output of fiber was connected to a 12 GHz photodetector (NewFocus 1580-A) and its output was coupled
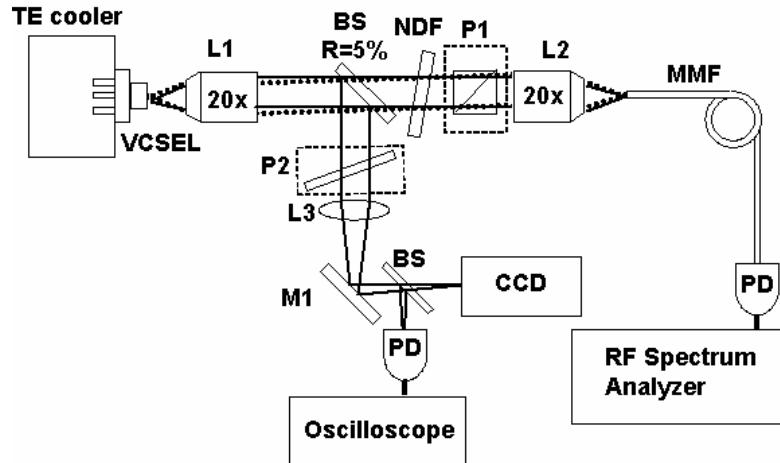


Fig. 3-11 Relative Intensity Noise test system setup

to a RF spectrum analyzer (HP 8563E).

The main problem with the measured noise in the RF spectrum analyzer is that it also represents the shot noise power caused by the quantum nature of the photodetection and the receiver's total measured thermal noise power. Hence in order

to quantify the shot noise power and the receiver thermal noise power we use, the experimental procedure as described in following.

In order to measure the shot noise power and the receiver thermal noise power, we turn off the transmitter and just have the receiver connected to the RF Spectrum Analyzer. By comparing the noise power level between the 'Transmitter On & Receiver On' and 'Transmitter Off & Receiver On' cases, we can find the receiver thermal noise to be ~ -66 dBm. The system relative intensity noise has contributions from the RIN laser, photodiode shot noise power and thermal noise power. Hence

$$RIN(Measured) = RIN(Laser) + \frac{2q}{I_{dc}} + \frac{P_n(thermal)}{P_{AVG}(electrical)}$$

(3-3)

Now RIN(Measured) = -66 – 10*log(Resolution BW) – $P_{avg,elec}$

The is $P_{avg,elec}$   found by modulating the transmitter with a 10dBm 200Mhz signal. The average signal power found at the modulating frequency gives the $P_{avg,elec}$. For example, $P_{avg,elec}$ = -0.587 dBm

Also the $I_{dc}$ current is generated from this $P_{avg,elec}$. Hence $I_{dc}^2$ R = $P_{avg,elec}$   where R = 50 ohms, resolution bandwidth = 1 MHz.

Hence RIN(Measured) = -66 – 10*log(1000000) – (-0.587) =    -125.4 dB/Hz

$$\frac{2q}{I_{dc}} = \frac{2*1.609x10^{-19}}{4.18x10^{-3}} = 7.7x10^{-17} = -161.13dB/Hz$$

$$\frac{P_n(thermal)}{P_{AVG}(electrical)} = -67.5 - 10*\log(1000000) - (-0.587) = -126.9dB/Hz$$

Hence ,

$$RIN(Laser) = RIN(measured) - \frac{2q}{I_{dc}} - \frac{P_n(thermal)}{P_{AVG}(electrical)} = -159.6dB/Hz$$

# CHAPTER 4    Strain-Compensated InGaAsP/InGaP MQWs VCSELs

The use of an Al-free InGaAsP based active region is an attractive alternative to the conventional (Al)GaAs active region for IR VCSELs. While edge emitting diode lasers with Al-free active regions have demonstrated performance and reliability surpassing AlGaAs-active devices [8-9].   In addition, theoretical calculations have predicted a lower transparency current density, a high differential gain and better temperature performance in InGaAsP-strain active VCSELs in respect to lattice-matched GaAs quantum-well active devices [10]. These parameters are all very important in high speed and high temperature VCSEL design because the relaxation resonance frequency of the laser depends on the square root of the differential gain as well as the difference of operation current and threshold current [4]. The use of tensile-strained barriers like $In_{0.4}Ga_{0.6}P$ can provide strain compensation and reduce active region carrier leakage. Al-free materials are significantly less reactive to oxide level, compared to AlGaAs materials make them ideal for the reliable manufacture process [8]. Proton implanted VCSELs using compressive strain $In_{0.18}Ga_{0.82}As_{0.8}P_{0.2}$ active-region has been demonstrated good performance [11]. This chapter present the fabrication and characteristics of high performance 850nm InGaAsP/InGaP SC-MQWs VCSELs. High speed modulation up to 12.5 Gbit/s was demonstrated from $25^{\circ}C$ to $85^{\circ}C$ utilizing $In_{0.18}Ga_{0.82}As_{0.8}P_{0.2}/In_{0.4}Ga_{0.6}P$ strain-compensated MQWs (SC-MQWs) VCSELs [12]. The DC, small signal, and large signal measurements were performed on SC-MQWs VCSELs. Finally, the initial reliability data from these VCSELs are presented.

## 4.1 Theory

To compare the InGaAsP/InGaP SC-MQWs and GaAs/AlGaAs QWs, the gain spectrum and material gain as a function of carrier density were calculated based on the k•p theory with valence banding mixing effect. An 8×8 Lutttinger-Kohn Hamiltonian matrix is used in this investigation. The method is followed by Chuang [13] and the gain spectral is broadened by Lorentzian's function. The well width and MQWs compositions were both set as 8 nm and $In_{0.18}Ga_{0.82}As_{0.8}P_{0.2}/In_{0.4}Ga_{0.6}P$ to tune the emission wavelength to 842 nm. A scheme of the conduction band diagram was shown in Fig. 4-1.   The obtained gain spectrum and material gain were compared with a conventional $GaAs/Al_{0.26}Ga_{0.74}As$ MQWs using same algorithm. The conduction band offset of $In_{0.18}Ga_{0.82}As_{0.8}P_{0.2}/In_{0.4}Ga_{0.6}P$ and $GaAs/Al_{0.26}Ga_{0.74}As$ are

assumed to be 0.5 and 0.65 respectively. The calculation of bandgap energy formula is adapted from Varshni equation with $\alpha = 5.5 \times 10^{-4}$ eV/K, $\beta = 225$ K for both InGaAsP and AlGaAs materials and the bandgap is adapted the value at 298 K. Although the Varshni parameters might not be the same for InGaAsP and AlGaAs, the error incurred is likely tolerable because the small bandgap deviation should not affect the material gain. As shown in Fig. 4-2(a), the material gain of $In_{0.18}Ga_{0.82}As_{0.8}P_{0.2}/In_{0.4}Ga_{0.6}P$ is approximately triple higher than that of $GaAs/Al_{0.26}Ga_{0.74}As$ structure when the input carrier concentration is $2 \times 10^{18}$ $cm^{-3}$. The material gains of $In_{0.18}Ga_{0.82}As_{0.8}P_{0.2}/In_{0.4}Ga_{0.6}P$ and $GaAs/Al_{0.26}Ga_{0.74}As$ as a function of the input carrier concentration are depicted in Fig. 4-2(b). The transparent carrier concentrations of $In_{0.18}Ga_{0.82}As_{0.8}P_{0.2}/In_{0.4}Ga_{0.6}P$ and $GaAs/Al_{0.26}Ga_{0.74}As$ are $1.5 \times 10^{18}$ $cm^{-3}$ and $1.78 \times 10^{18}$ $cm^{-3}$ respectively. Furthermore, $In_{0.18}Ga_{0.82}As_{0.8}P_{0.2}/In_{0.4}Ga_{0.6}P$ provides higher gain than $GaAs/Al_{0.26}Ga_{0.74}As$ in the entire calculation range. The results obtained numerically suggest that the high material gain, low transparency carrier concentration make the InGaAsP SC MQWs a better active layer. In addition, its superior performance has been confirmed in edge emitting lasers. [8-9]

## 4.2 Fabrication Process of polyimide planarized VCSEL

The schematic structure of a fabricated top emitting VCSEL is shown in Fig. 4-3(a), which has been grown by low pressure metal organic chemical vapor deposition (MOCVD) on a semi-insulating (100) GaAs substrate. The group-V precursors are the hydride sources $AsH_3$ and $PH_3$. The trimethyl alkyls of gallium (Ga), aluminum (Al) and indium (In) are the group-III precursors. The dopant sources are $Si_2H_6$ and $CBr_4$ for the *n* and *p* dopants, respectively. The bottom n-type distributed Bragg reflector (DBR) consists of 35-period-$Al_{0.15}Ga_{0.85}As/Al_{0.9}Ga_{0.1}As$. The top p-type DBR consists of 23 pairs of $Al_{0.15}Ga_{0.85}As/Al_{0.9}Ga_{0.1}As$. The active layer consists of three $In_{0.18}Ga_{0.82}As_{0.8}P_{0.2}/ In_{0.4}Ga_{0.6}P$ (80Å/100Å) SC-MQWs surrounded by $Al_{0.6}Ga_{0.4}As$ cladding layer to $1\tilde{\lambda}$-cavity. A 30nm thick $Al_{0.98}Ga_{0.02}As$ was introduced on the upper cavity spacer layer to form an oxide confinement. Finally, $1\lambda$ thickness of current spreading layer and heavily doped GaAs (p> $2 \times 10^{19}$ $cm^{-3}$) contacting layer was grown. The n-type DBR was grown at 750$^{o}$C. The quantum well region and p-type DBR were grown at 650$^{o}$C. Growth interruptions of 5s, 10s, or 15s were introduced before and after $In_{0.18}Ga_{0.82}As_{0.8}P_{0.2}$ QW growth. Fig. 4-4 shows the comparison of

photoluminescence spectra of $In_{0.18}Ga_{0.82}As_{0.8}P_{0.2}/In_{0.4}Ga_{0.6}P$ with different growth interruption times. The 5s growth interruption is not enough to evacuate residual As in the growth reactor, resulting in the carry-over of As into the $In_{0.4}Ga_{0.6}P$ barrier. The 15s growth interruption is so long that some impurities can be gettered at the interface or indium segregation after strained layer growth, resulting in the degradation of luminescence. The 10s growth interruption seems to give the best luminescence quality. The composition of SC-MQWs is characterized by high-resolution x-ray diffraction. The gain peak position = 835 nm was determined by photoluminescence while the FP-dip resonant wavelength = 842 nm was determined by reflectance measurement. The VCSELs were fabricated utilizing the processing described by Peters *et al.* to minimize capacitance while keeping reasonably low resistance [3]. The processing sequence included six photomasks to fabricate polyimide-planarized VCSELs with coplanar wave-guide probe pads, as shown in Fig. 4-3(b). Device fabrication began with the formation of cylindrical mesas of 20 μm in diameter by etching the surrounding semiconductor to the bottom n-type mirror to a depth of 5 μm using a Reactive Ion Etching (RIE) system. The sample was wet-oxidized in a 420 °C steam environment for ~12 min to form the current aperture and provide lateral index guiding to the lasing mode. The oxidation rate was 0.6 μm/ min for the $Al_{0.98}Ga_{0.02}As$ layer, so the oxide extended 7.5 μm from the mesa sidewall. The VCSELs therefore have a 5 μm in diameter emitting aperture defined by lateral oxidation. A 40 μm circular mesa were formed after oxidation using wet chemical etching ($H_2O:H_2SO_4:H_2O_2 = 8:1:8$) down to n-buffer layer. Following $Si_3N_4$ was deposited for passivation. Ti/Au was evaporated for the p-type contact ring, and AuGeNi/Au was evaporated onto the etched n–buffer layer to form the n-type contact which is connected to the semi-insulating substrate. Contacts were alloyed for 30 sec at 420 °C using RTA. After contact formation, photosensitive polyimide was spun on the sample for field insulation and planarization. Ti/Au with thicknesses of 200/3000Å were deposited for metal interconnects and coplanar waveguide probe-bond pads. Heat treatment after the metal deposition was utilized to improve metal-to-polyimide adhesion strength. Fig. 4-5 shows the SEM photo of a finished VCSEL.

## 4.3 Result and discussion

Fig. 4-6 shows the typical light output and voltage versus current (LIV) curves of the SC-MQWs InGaAsP/InGaP VCSEL at room temperature and 85°C under CW opteration.

These VCSELs exhibit kink-free current-light output performance with threshold currents ~0.4 mA, and slope efficiencies ~ 0.6 mW/mA. The threshold current change with temperature is less than 0.2 mA and the slope efficiency drops by less than ~30% when the substrate temperature is raised from room temperature to 85°C.    This is superior to the properties of GaAs/AlGaAs VCSELs with similar size [14]. The resistance of our VCSELs is ~95 Ohm and capacitance is ~0.1 pF. As a result, the devices are limited by the parasitics to a frequency response of approximately 15 GHz. The lateral mode characteristics is an important feature since it strongly affects the transmission properties. Fig. 4-7 shows the emission spectrum of a VCSEL at an operating current of 6 mA. This spectrum was recorded with an optical spectrum analyzer (Advantest 8381A) with spectral resolution of 0.1 nm. Two dominant modes were observed at 844.2 nm and 843.7 nm. The root-mean-squared (RMS) spectral linewidths at 2, 6, 8 mA are 0.15, 0.37, and 0.4 nm respectively, which can fulfill the requirement (<= 0.45 nm) of 10Gbps data transmission.[15]

The small signal response of VCSELs as a function of bias current was measured using a calibrated vector network analyzer (Agilent 8720ES) with on-wafer probing and a 50 μm multimode optical fiber connected to a New Focus 25GHz photodetector. Fig. 4-8 shows the measured (dashed lines) and fitted (solid lines) small-signal frequency response of a 5 μm VCSEL at different bias current levels. The modulation frequency is increased with increasing bias current until flattening at a bias of approximately 5mA. With only 3mA (5mA) of bias current, the maximum 3dB modulation frequency response is measured to be ~13 (14.5) GHz at 25 °C and is suitable for 12.5 Gb/s operation. The measured data were fit to a general 3-pole modulation transfer function [16, 17]

$$H(f) = C\left(\frac{fr^2}{fr^2 - f^2 + j\frac{f}{2\pi}\gamma}\right)\left(\frac{1}{1 + j\left(\frac{f}{fp}\right)}\right)$$

where $f$ is modulation frequency, $f_p$ is parasitic roll off frequency, $f_r$ is resonant frequency and $\gamma$ is damping rate.

Fig. 4-9 shows the 3dB modulation frequency as a function the square root of the difference in current above threshold. The relaxation resonance frequency is found saturate for driving currents above 3mA.    By fitting the lowest current points in Fig. 4-8, we obtain a modulation current efficiency of 11.6 GHz/(mA)$^{1/2}$[18]. This is higher than GaAs/AlGaAs VCSELs with similar size [6, 19] and is comparable with oxide confined VCSELs with InGaAs based quantum wells [7, 16]. Plotting the damping rate $\gamma$ versus $f_r^2$ reveals a K-factor of 0.3 ns. Neglecting heating effects and external parasitics, the intrinsic bandwidth was found to be 29.6GHz using the relation $f_{max} = \sqrt{2}(2\pi/K)$   .

To measure the high-speed VCSEL under large signal modulation, microwave and

lightwave probes were used in conjunction with a 12.5-Gb/s pattern generator and a 12-GHz photoreceiver. The eye diagrams were taken for back-to-back (BTB) transmission on SC-MQWs InGaAsP/InGaP VCSEL. As shown in Fig. 4-10(a), the room temperature eye diagram of our VCSEL biased at 4 mA with data up to 12.5 Gb/s and 6dB extinction ratio has a clear open eye pattern indicating good performance of the VCSELs. The rise time $T_r$ is 28 ps and fall time $T_f$ is 41 ps with jitter (p-p)=20 ps. The VCSELs also show superior performance at high temperature. Fig. 4-10 (b) demonstrated the high speed performance of our VCSELs (biased at 5mA) with reasonably open eye-diagrams at 12.5 Gb/s and 6dB extinction ratio at 85°C.    This further confirms the superior performance of our VCSELs.

To guarantee the device reliability is always a tough work but a natural task for the components supplier in the data communication markets. We have accumulated life test data up to 1000 hours at 70°C/8mA with exceptional reliability. As shown in Fig. 4-11, the light output is plotted versus time scale for SC-MQW VCSEL chips under the high temperature operation lifetime (HTOL) test at 70°C/8mA. None of them shows the abnormal behavior.

**References**
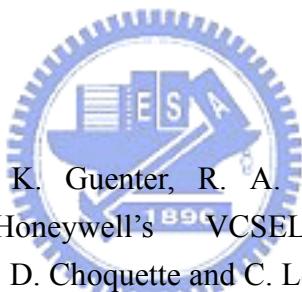
[1] J. A. Tatum, A. Clark, J. K. Guenter, R. A. Hawthorne, and R. H. Johnson, "Commercialization of Honeywell's VCSEL technology," *Vertical-Cavity Surface-Emitting Lasers IV*, K. D. Choquette and C. Lei, editors, Proceedings of the SPIE, vol. 3946, pp. 2-13, SPIE, Bellingham, WA, 2000..

[2] F. H. Peters and M. H. MacDougal, "High-Speed High-Temperature Operation of Vertical-Cavity Surface-Emitting Lasers" IEEE Photon. Technol. Lett., vol. 13, No 7, p. 645–647, July 2001.

[3] F. H. Peters, D. J. Welch, V. Jayaraman, M. H. MacDougal, J. D. Tagle, T. A. Goodwin, J. E. Schramm, T. D. Lowes, S. P. Kilcoyne, K. R. Nary, J. S. Bergey, and W. Carpenter, "10 Gb/s VCSEL-based data links," Photonics West, San Jose, CA, Tech. Rep. OE 3946–26, 2000.

[4] C.W. Wilmsen, H. Temkin, and L.A. Coldren, eds., *Vertical-Cavity Surface-Emitting Lasers: Design, Fabrication, Characterization, and Applications*, Cambridge University Press, 1999.

[5] K. L. Lear, M. Ochiai, V. M. Hietala, H. Q. Hou, B. E. Hammons, J. J. Banas, and J. A. Nevers, "High-speed vertical cavity surface emitting lasers," in *Dig. IEEE/LEOS Summer Topical Meetings*, 1997, pp. 53–54.

[6] J. A. Lehman, R. A. Morgan, M. K. Hibbs-Brenner, and D. Carlson, "High-frequency modulation characteristics of hybrid dielectric/AlGaAs mirror singlemode VCSELs," *Electron. Lett.*, vol. 31, pp. 1251-1252, 1995.

[7] K. L. Lear, A. Mar, K. D. Choquette, S. P. Kilcoyne, R. P. Schneider, Jr., and K. M. Geib, "High-frequency modulation of oxide confined vertical cavity surface emitting lasers," *Electron. Lett.*, vol. 32, pp. 457–458, 1996.

[8] L. J. Mawst, S. Rusli, A. Al-Muhanna, and J. K. Wade, "Short-wavelength (0.7 μm < λ <0.78 μm) high-power InGaAsP-active diode lasers," *IEEE J. Select. Topics Quantum Electron.*, vol. 5, pp. 785–791, (1999).

[9] N. Tansu, D. Zhou, and L. J. Mawst, "Low Temperature Sensitive, Compressively-Strained InGaAsP Active (λ=0.78-0.85 μm) Region Diode Lasers," *IEEE Photon. Technol. Lett.*, Vol.12(6), pp.603-605 , 2000.

[10] T. E. Sale, C. Amamo,Y. Ohiso, and T.Kurokawa, "Using strained lasers (AlGa) In As P system materials to improve the performance of 850 nm surface- and edge-emitting lasers," *Appl. Phys. Lett.*, vol. 71, p. 1002–1004, (1997).

[11] N. Tansu, L.J Mawst, "Compressively-strained InGaAsP-active (λ=0.85μm) VCSELs" *IEEE Lasers and Electro-Optics Society 2000 Annual Meeting. LEOS 2000.* vol. 2, p. 724 -725 (2000).

[12] H. C. Kuo, Y. S. Chang, F. I. Lai, T. H. Hsueh, "High speed modulation of 850 nm InGaAsP/InGaP strain-compensated VCSELs. Electon. Lett. Vol 39, p. 1051-10523 (2003)

[13] S. L. Chuang, "Efficient band-structure calculation of strained quantum-wells", Phys. Rev. B, 43, 9649-9661 (1991).

[14] David J. Bossert, Doug Collins, Ian Aeby, J. Bridget Clevenger, "Production of high-speed oxide confined VCSEL arrays for datacom application" Photonics West, San Jose, CA, p.p 142 Proc. SPIE Vol. 4649 (2002)

[15] http://www.ieee802.org/

[16] Thibeault BJ, Bertilsson K, Hegblom ER, "High-speed characteristics of low-optical loss oxide-aperture vertical-cavity laser," IEEE Photon. Technol. Lett., vol. 9, pp. 11-13, Jan. 1997

[17] L. A. Coldren and S. W. Corzine, *Diode Lasers and Photonic Integrated Ciurcuits*. New York: Wiley, 1995, pp. 201-204

[18] T. R. Chen, B. Zhao, L. Eng, Y. H. Zhuang, "Very high modulation efficiency of ultralow threshold current single quantum well InGaAs lasers", Electon. Lett., Vol. 29, p. 1525-1526 (1993)

[19] Sven Eitel, Stephan Hunziker, Dominique Vez, "Multimode VCSELs for high bit-rate and transparent low-cost fiber-optic links", p183 Proc. SPIE Vol. 4649 (2002)
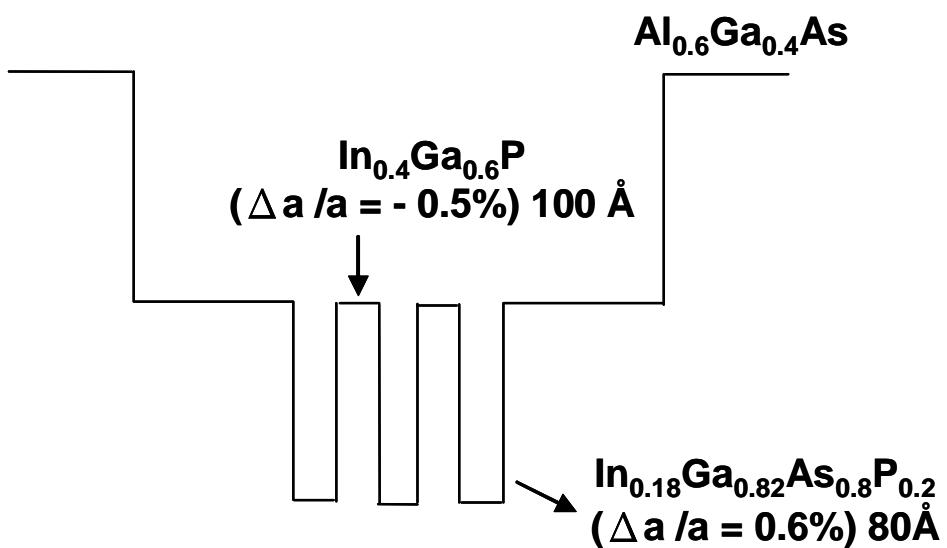
FIG. 4-1 Schematic energy bandgap diagram for $In_{0.18}Ga_{0.82}As_{0.8}P_{0.2}/In_{0.4}Ga_{0.6}P$ active region.

Fig. 4-2(a)
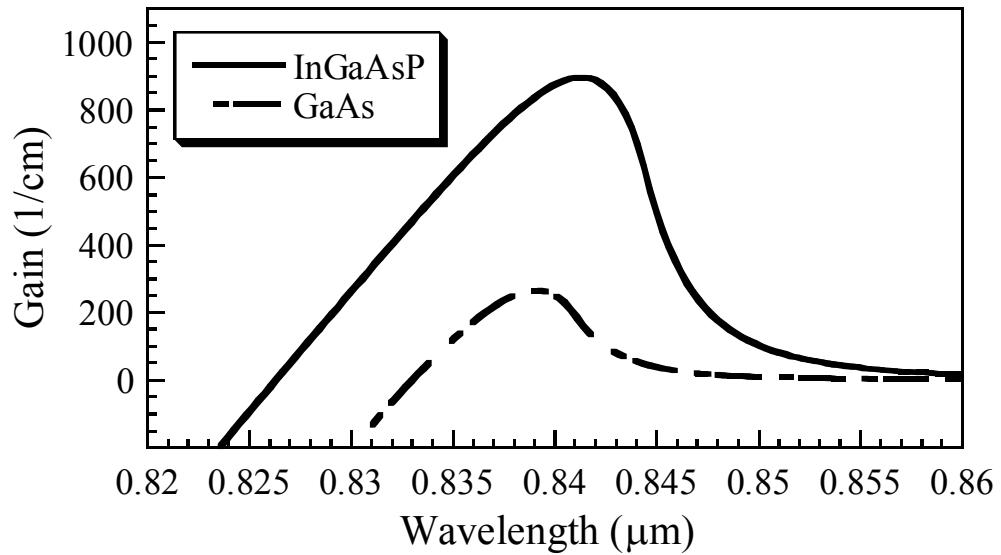


Fig. 4-2(b)
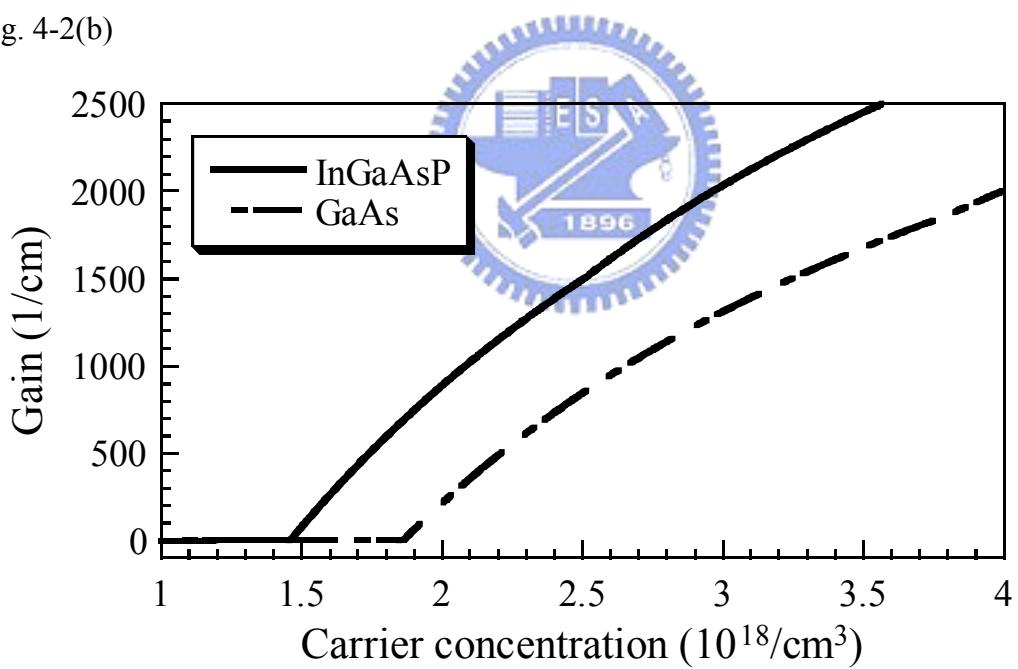


FIG. 4-2 Material gain spectrum and material gain as a function of carrier density of

$In_{0.18}Ga_{0.82}As_{0.8}P_{0.2}/In_{0.4}Ga_{0.6}P$ MQW and $GaAs/Al_{0.26}Ga_{0.74}As$ MQW
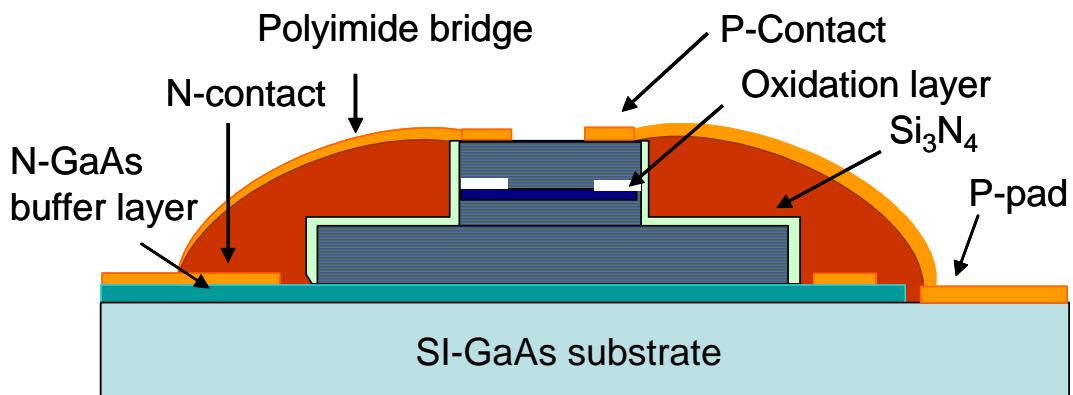
FIG. 4-3(a) Schematic cross section of high speed VCSEL structure.
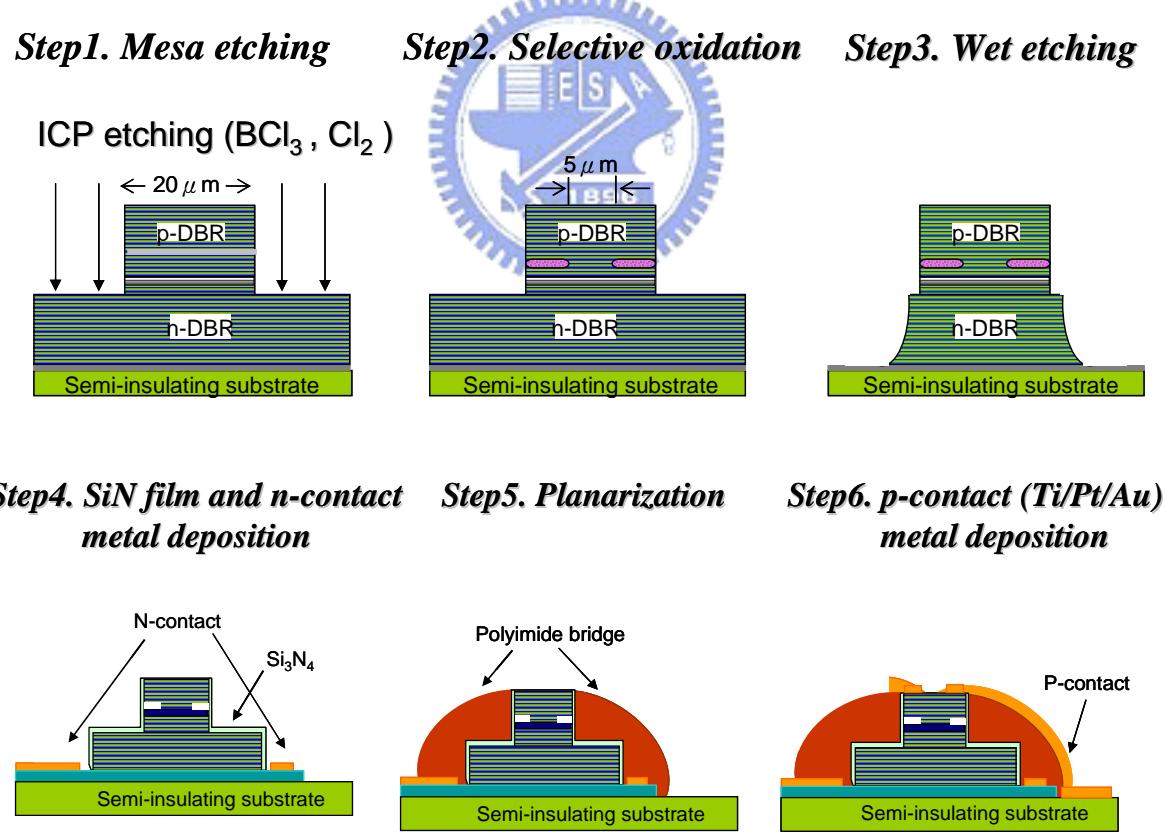


FIG. 4-3(b) Process steps of high speed VCSELs.
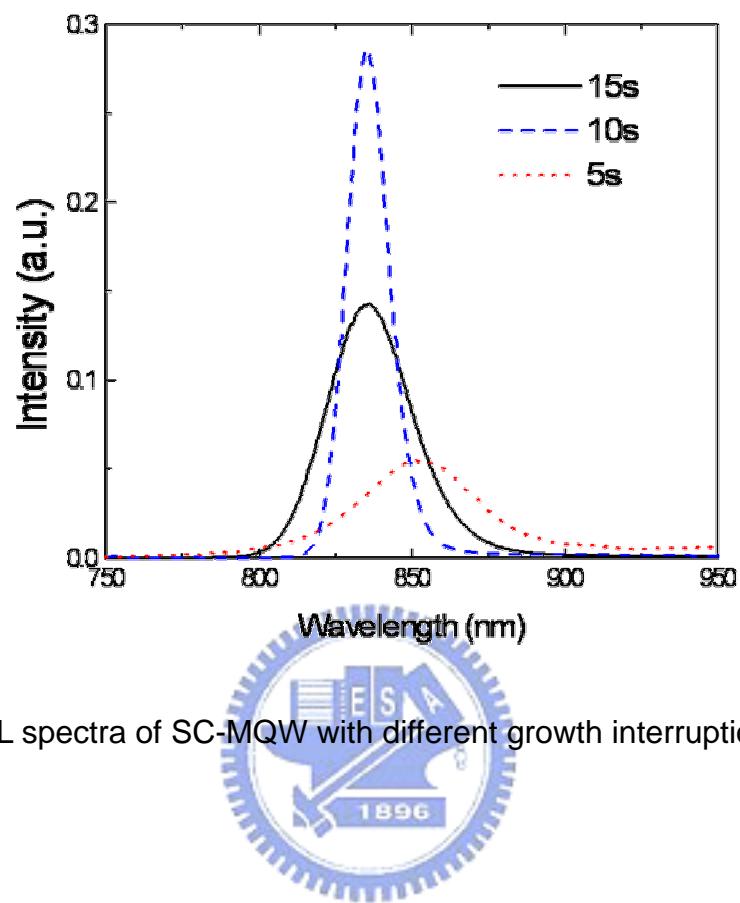
FIG. 4-4 PL spectra of SC-MQW with different growth interruption times.
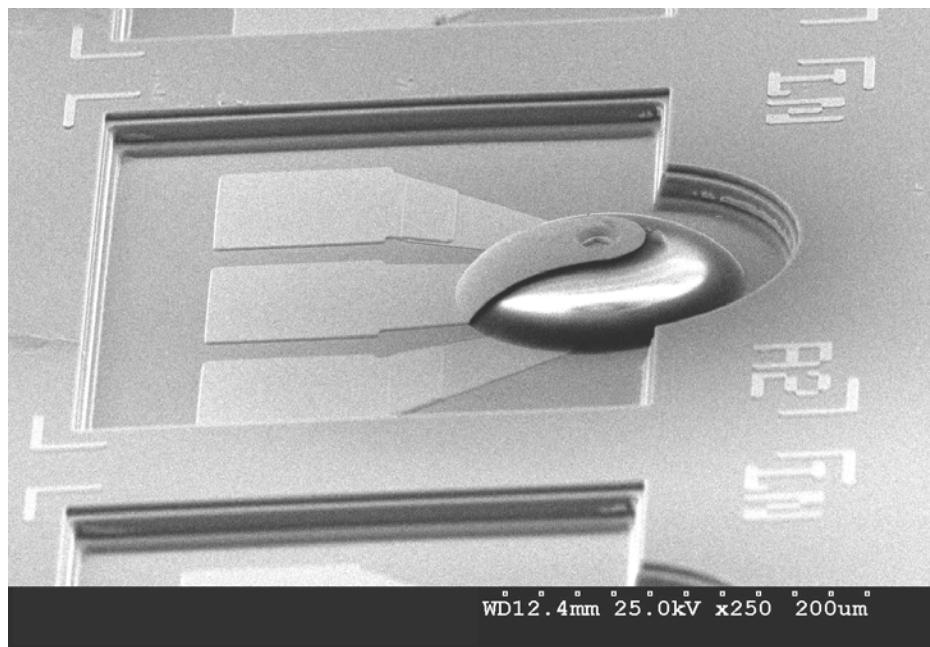
FIG. 4-5 SEM picture of the finished VCSEL
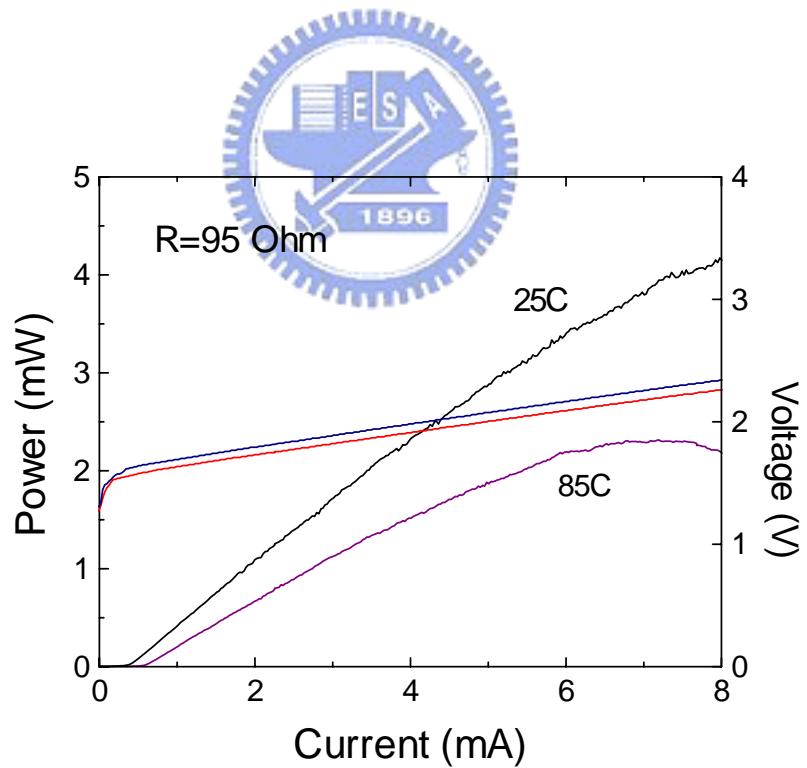


FIG. 4-6 SC-MQWs InGaAsP/InGaP VCSEL light output and voltage versus

current (LIV) curves at room temperature and 85°C.
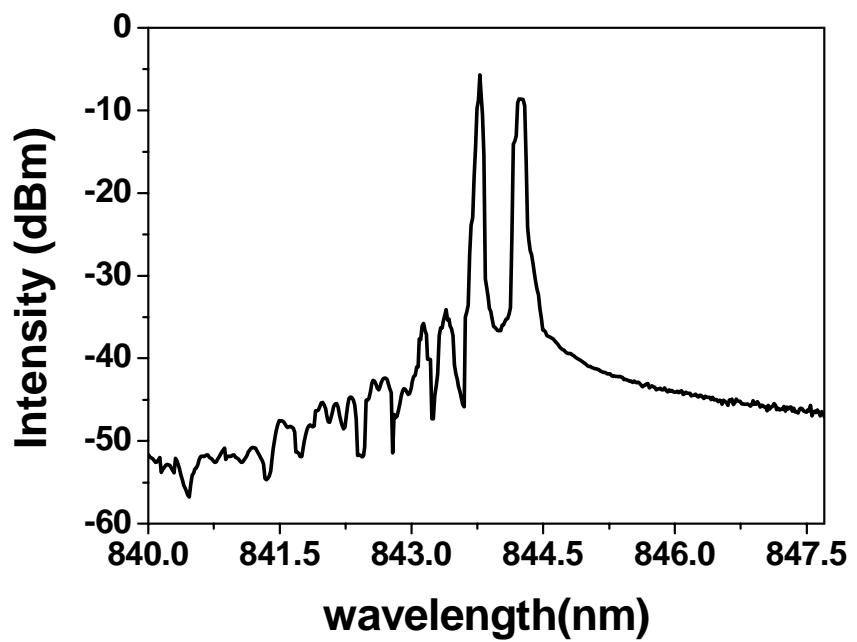
FIG. 4-7 Optical spectrum at 6 mA of the VCSEL
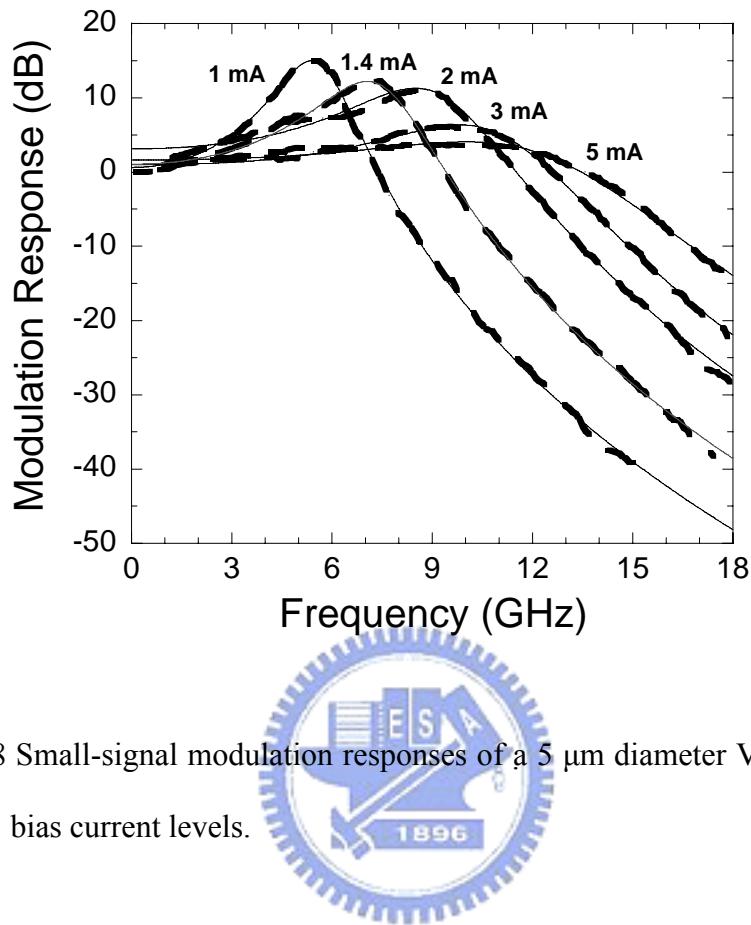
FIG. 4-8 Small-signal modulation responses of a 5 μm diameter VCSEL at different

bias current levels.
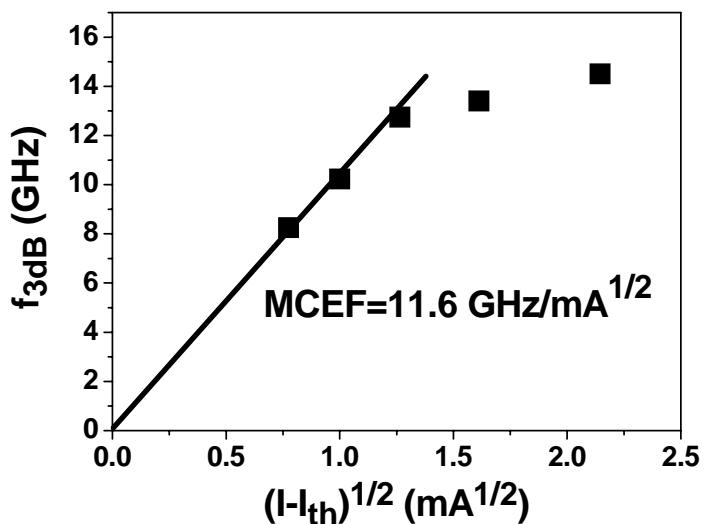


Fig. 4-9 Resonant frequency as a function of square root of current above

threshold current.

Fig. 4-10(a)
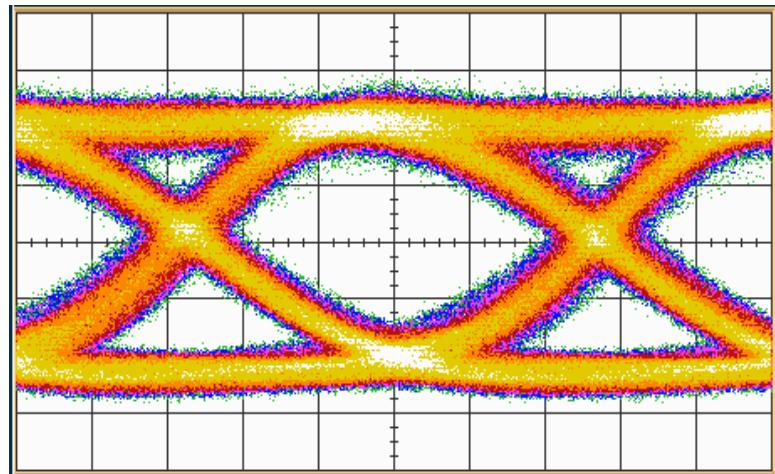


Fig. 4-10(b)
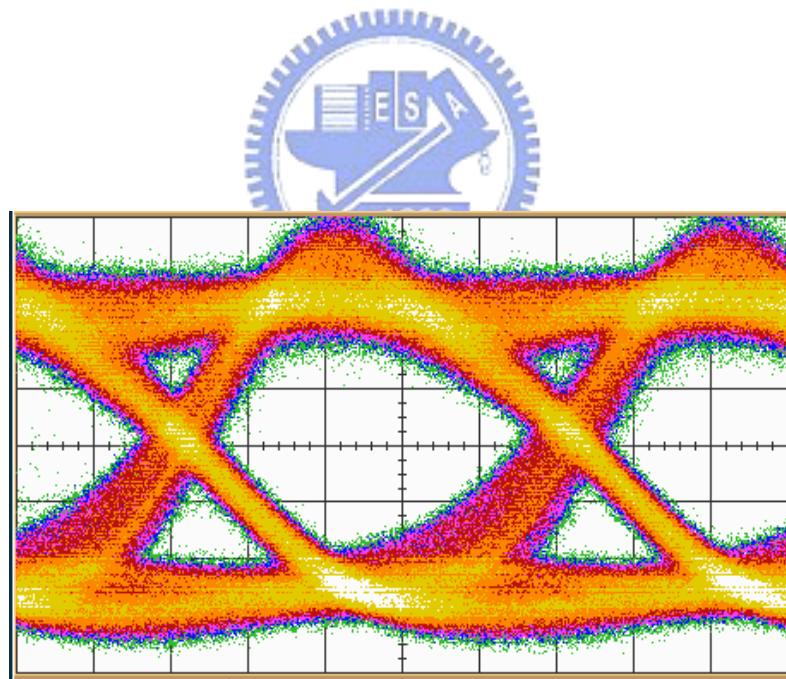


FIG. 4-10   (a) 25°C (b) 85°C eye diagram of SC-VCSEL up to 12.5 Gb/s with 6dB

extinction ratio. The scale in the fig. is 15 ps/div.

FIG. 4-11 HTOL (70°C/8mA) performance of strain compensated VCSEL
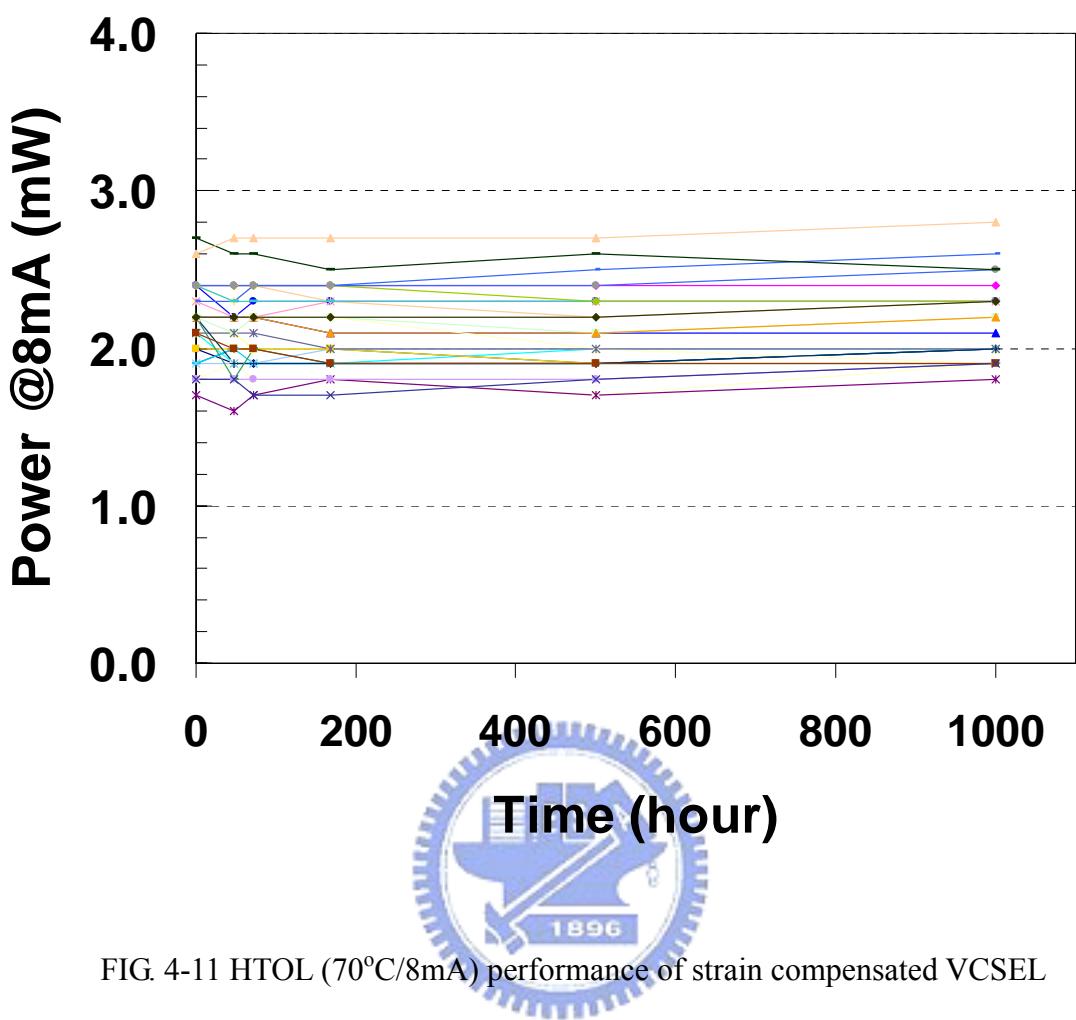
# CHAPTER 5    Reducing capacitance of Oxide-Confind VCSEL by proton implantation

## 5.1 Introduction

850 nm oxide-confined Vertical Cavity Surface Emitting Lasers (VCSELs) have become a standard technology for applications in local area networks (LANs) and storage area networks (SANs). The main advantages of VCSELs are low threshold current, low divergence angle, and circular beam, leading to simpler packaging and low electrical power consumption. The surface emission property of VCSELs also simplifies the 2-dimensional arrays and enables wafer level testing, thus low fabrication cost [1]. However, the electrical resistance of VCSELs is higher than that of edge-emitting lasers owing to their small current injection area and highly resistive DBRs. The small top contact area also increases contact resistance. For 10Gbps operation, the 3dB-bandwidth should exceed 7GHz [2]. Since the typical electrical resistance of high speed VCSELs is ~100 Ohm due to smaller oxide-confined aperture (5-7 μm in diameter), the requirement for the RC time constant therefore depends on the parasitic capacitance of device. Previously developed art high-speed VCSELs adopted either intra-cavity/co-planar metal contact [3] or the polyimide planarization [4] process to reduce parasitic capacitance. Unfortunately, these nonplanar approaches have numerous disadvantages and are inconvenient for mass production [5]. To avoid these unfavorable process techniques, a simple planar approach for high-speed oxide-confined VCSELs fabrication has already been demonstrated [5] [6]. The static operation characteristics and lifetime test of devices demonstrate the fabrication technology adequate to the requirement of mass production. To further improve VCSELs performance, additional proton implantation procedure was introduced into the process to reduce parasitic capacitance, and the eye-diagram widened to 10 Gbps was obtained [6]. This chapter details the proton implantation effect on high speed VCSELs with planar geometry. A comprehensive small signal measurement and analysis was conducted based on the physical modeling of VCSELs. The analytical results confirm that proton implantation effectively reduces the parasitic capacitance of the oxide-confined VCSELs, improving the high speed performance.

## 5.2 Fabrication Process

The VCSEL epi-wafers were grown by Aixtron 2400 G3 metal-organic chemical

vapor-phase deposition (MOCVD) on $n^+$-GaAs substrate, the structure of which consists of a three quantum-well GaAs/AlGaAs active layer, sandwiched by fully doped n- and p-DBR mirrors. Both n- and p-DBR are composed of interlaced $1/4\lambda$-thick $Al_{0.15}Ga_{0.85}As$ and $Al_{0.9}Ga_{0.1}As$ layers, with the periods of 39.5 and 22, respectively. The oxide-confined VCSEL process procedure has been described elsewhere [5] [6]. Moreover, the mesa diameter of the fabricated device was 22 μm with a 5 μm oxide aperture, and the device surface was quasi-planar so that the annular p-contact metal and the bond pad were on the same level. The p-contact was created by directly depositing Ti/Pt/Au on the upper heavily doped $p^+$ GaAs contact layer, and Au/Ge/Ni/Au was deposited on the bottom side of the substrate following thinning down. Notably, the process did not use either the intra-cavity / co-planar metal contact nor the polyimide resin planarization technique. Multiple proton implantations with a dose of $10^{15}$ $cm^{-2}$ and four different proton energy ranges between 300 to 420keV were adapted according to simulation results of the stopping and range of ions in matter (SRIM). The implantation region was kept away from the mesa to prevent damage to the active region and consequent voiding of triggering reliability issues.

## 5.3 LIV / 3-dB Bandwidth / Eye diagram
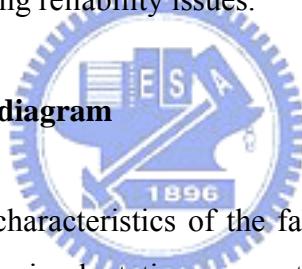
Fig. 5-1 displays the L-I-V characteristics of the fabricated VCSELs with (solid lines) and without (dashed lines) proton implantation, respectively. The inset in the lower right corner of Fig. 5-1 also shows a top view microphotograph of the emitting area. Notably, the L-I-V curves before and after implantation are very similar. This result differs significantly from previous investigation [7], because the mesas were entirely protected during implantation in this study and thus no damage was introduced into the active region. Consequently the threshold current can be maintained at the same value, and the DC characteristics are not influenced. The threshold currents of both samples are 0.5mA and the resistance typically is 90 ohm.

The small signal response of VCSELs as a function of bias current was measured using a calibrated vector network analyzer (Agilent 8720ES) with on-wafer probing and a 50 m multimode optical fiber connected to a New Focus 25GHz photodetector. The samples then were wire bonded to coplanar transmission lines with an impedance of 50 ohm.

The small signal modulation responses for both oxide-only VCSEL and oxide-implanted VCSEL are shown in Figs. 5-2(a) and 5-2(b) respectively. Figure 5-2(a) reveals that the

resonance frequency increased with the biasing current as expected. The 3dB frequency was restricted at ~2.3 GHz owing to parasitic cut-off. After proton implantation, a parasitic-free modulation response was obtained as shown in Fig 5-2(b). Figure 5-3 plots the resonant frequency and 3 dB frequency as a function of bias current for both oxide-only and oxide-implanted VCSEL. Figure 5-3 clearly indicates that the resonant frequencies are similar for both oxide-only and oxide-implanted VCSELs. However, although the resonant frequency increases with bias current, the 3dB frequency is restricted at ~2.3 GHz for oxide-only VCSEL, while the 3dB frequency of oxide-implanted VCSEL increases with bias current throughout the measurement range. These results clearly show that the parasitic components restricted the modulation bandwidth of oxide-only VCSEL, and moreover that the proton implantation successfully removed the parasitic effect. For large signal modulation, bias current and a nonreturn-to-zero (NRZ) pseudorandom bit sequence (PRBS) were combined in a bias-tee and fed to a top-emitting VCSEL which was wire-bonded to an SMA socket. Figure 5-4 shows the eye diagram modulated at 10Gbps with 6mA bias and 6dB extinction ratio for both oxide-only and oxide-implanted VCSELs. For oxide-only VCSEL, the turn on jitter was about 30 ps, and the fall time tail clearly hit the mask. In contrast, the eye improved significantly after ion implantation, and could pass the 10 Gb/s mask. The rise time, fall time and jitter of the oxide-implanted device were 44 ps, 54 ps and 20 ps, respectively. To further explore how the ion-implantation influenced the electrical parasitic, Fig. 5-5 illustrates the reflection coefficient ($S_{11}$) of the oxide-only VCSEL and oxide-implanted VCSEL. The reflection coefficient curves reveal that more RF power is reflected back from the oxide-only VCSEL and therefore degrades the modulation bandwidth. The electrical bandwidth for oxide-only devices is ~ 3 GHz, and exceeds 20 GHz for oxide-implanted devices. This finding again confirms that the proton-implantation has successfully reduced the parasitic capacitance.

**5.4 Equivalent circuit extraction**

An equivalent circuit model shown in Fig. 5-6 was used to extract the circuit components. The resistance Rm represents the mirror loss, while the Ra accounts for the active region resistance. Ca represents a combination of the capacitance of the active area and oxide layer. A shunt resistance Rp is also included to account for pad loss, and the pad capacitance is represented by Cp. This equivalent circuit can also be applied to examine the extrinsic limitations on the modulation speed and to determine the influence of parasitic capacitance

and mirror resistance on the modulation bandwidth. The values of the circuit components were extracted using ADS (Advanced Design System, Agilent) by fitting both the magnitude and phase of $S_{11}$ over the measured frequency range. Based on a co-optimization at several bias conditions, Rm was around 42 ohm and Ra was found to be bias dependent, varying from 80 to 37 ohm in 1~6 mA. The major difference between oxide-only and oxide-implanted devices was the capacitance Ca and Cp. Moreover, the Ca and Cp of oxide-only devices were 1.8 and 0.4 pF, respectively, while the Ca and Cp of oxide-implanted devices were 0.5 and 0.28 pF, respectively. Therefore, proton-implantation is shown to effectively reduce both bond pad capacitance and oxide capacitance.

**References**

[1] Ian Aeby, Doug Collins, Brian Gibson, Christopher J. Helms, Hong Q. Hou, Wenlin Luo, David J. Bossert, Charlie X. Wang, *Photonic West*, San Jose, CA, pp. 152-161, Vol. 4994, 2003.

[2] Noriyuki Yokouchi, Norihiro Iwai, Akihiko Kasukawa, *Photonic West*, San Jose, CA, pp. 189-196, Vol. 4994, 2003.

[3] R.C. Strijbos , G. Verschaffelt , M. Creusen, W.C. Vleuten, F. Karouta, T.G. Roer, M. Buda, J. Danckaert, B. Ryvkin, I. Veretennicoff, and H. Thienpont, *Photonics West*, San Jose, CA, Tech. Rep. OE 3946–14, pp. 69-77, 2000.

[4] F. Mederer, M Grabherr, F. Eberhard, I. Ecker, R. Jager, J. Joos, C. Jung, M. Kicherer, R. King, P. Schnitzer, H. Unold, D. Wiedenmann, K.J. Ebeling, *Electronic Components and Technology Conference*, *Proceedings. 50th* , pp. 1242 –1251, 2000

[5] H.C. Yu, S.J. Chang, Y.K. Su, C.P. Sung, Y.W. Lin, H.P. Yang, C.Y. Huang, J.M. Wang, *CLEO PR 2003*, Conference Digest, pp. 159, 2004

[6] H.C. Yu, S.J. Chang, Y.K. Su, C.P. Sung, Y.W. Lin, H.P. Yang, C.Y. Huang, J.M. Wang, *Mater. Sci. Engi. : B.*, to be published.

[7] K.D. Choquette , A.J. Fischer, K.M. Geib , G.R.Hadley, A.A. Allerman, J.J. Hindi, *Semiconductor Laser Conference*, Conference Digest, pp.59 –60, 2000**.**
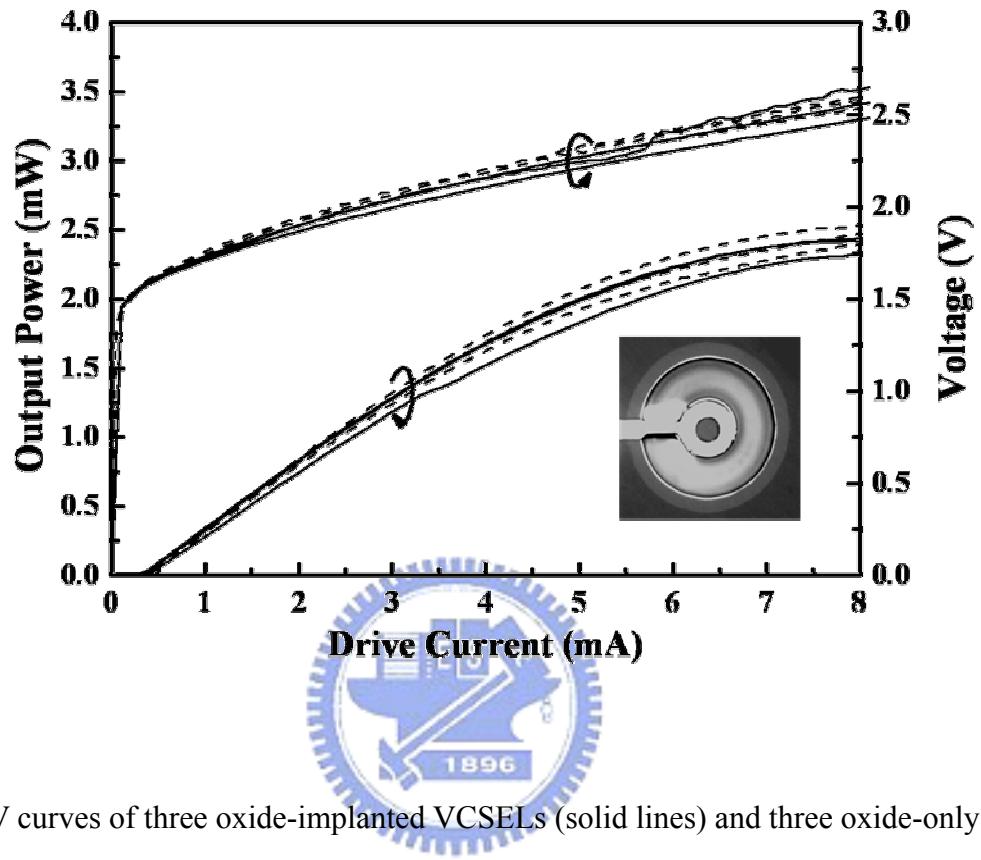
Fig. 5-1 L-I-V curves of three oxide-implanted VCSELs (solid lines) and three oxide-only VCSELs

(a)
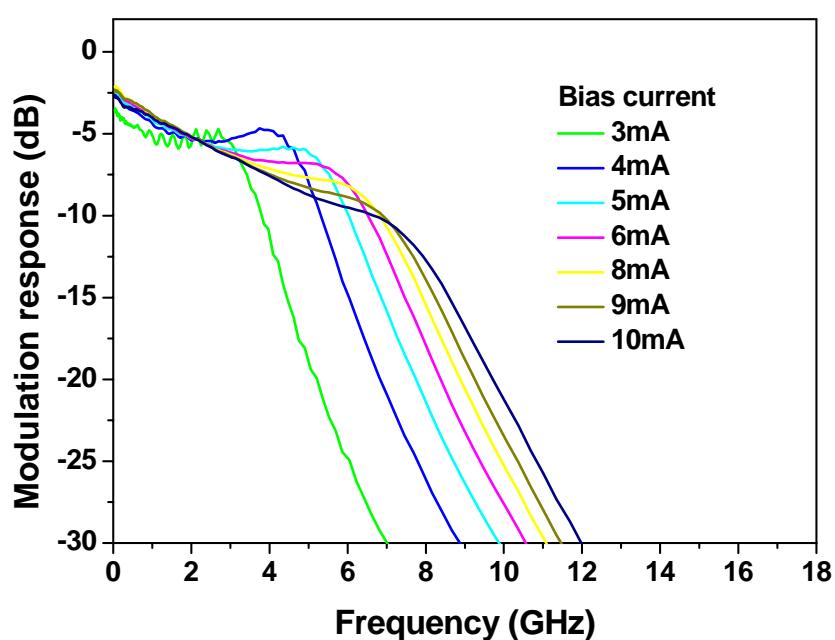


(b)
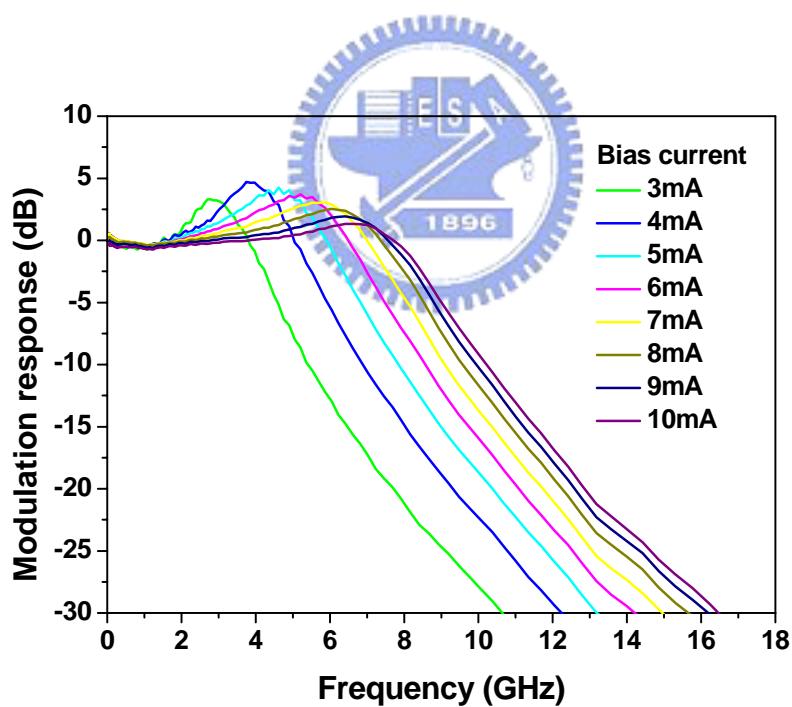
FIG. 5-2 Small signal modulation response of (a) oxide-only VCSEL (b) oxide-implanted

VCSEL

61
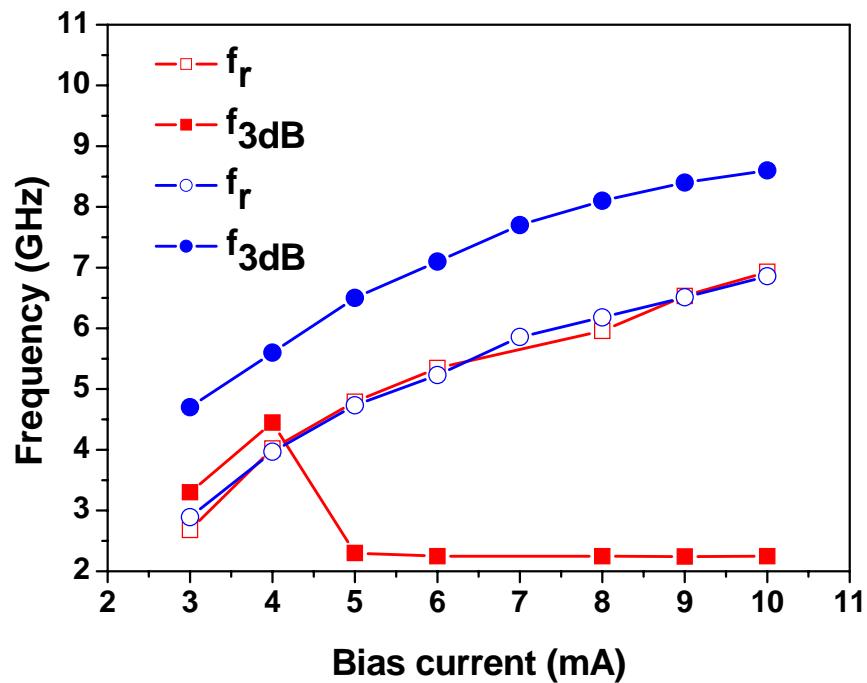
FIG. 5-3. Resonant frequency and 3 dB frequency for oxide-only VCSELs (square

symbol) and oxide-implanted VCSELs (circle symbol)
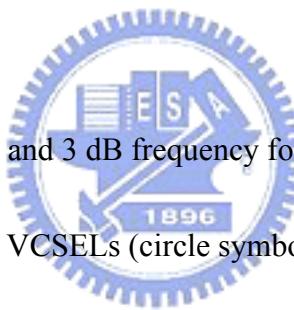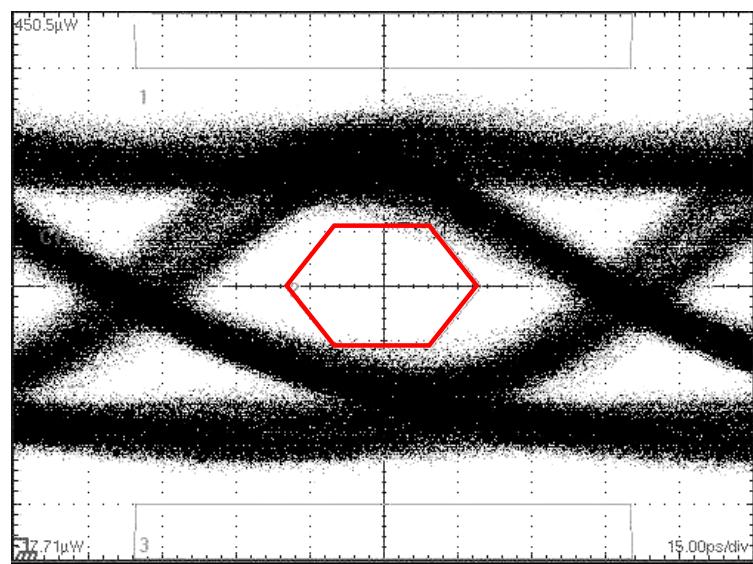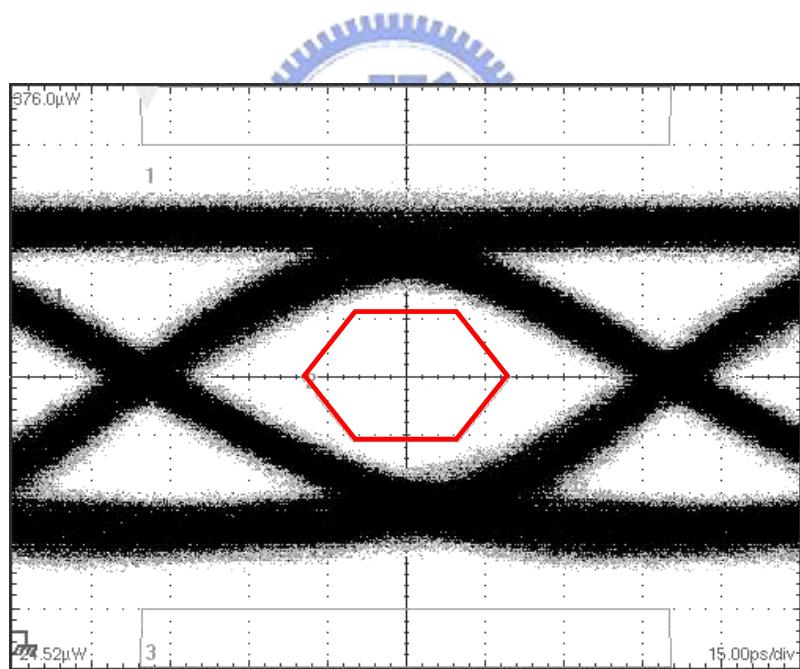
FIG. 5-4. Eye diagram of (a) oxide-only VCSEL (b) oxide-implanted VCSEL

63
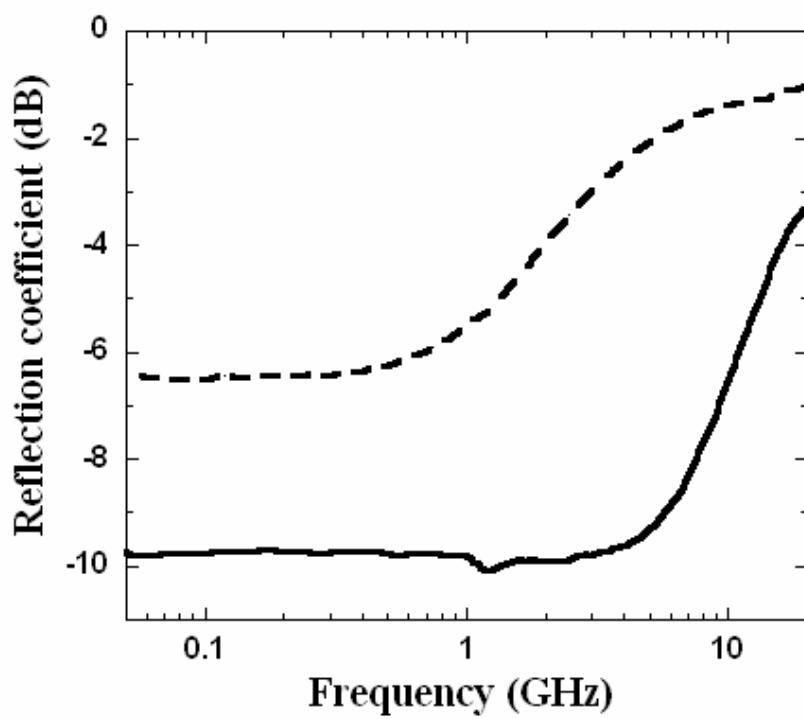
Fig. 5-5 Reflection coefficient ($S_{11}$) for oxide-only device (dashed line) and

oxide-implanted device (solid line) at 3 mA
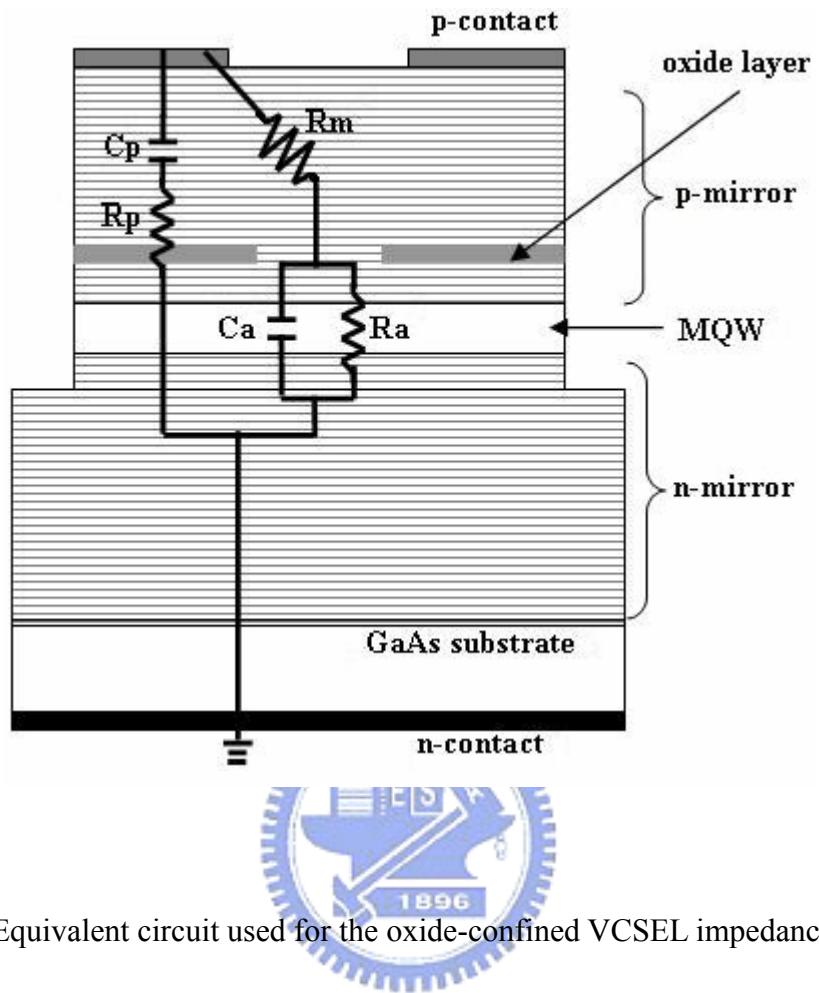
FIG. 5-6 Equivalent circuit used for the oxide-confined VCSEL impedance

# CHAPTER 6    High Speed (>13GHz) Modulation of 850nm VCSELs with Tapered Oxide Confined Layer

For optical communication applications, high modulation bandwidth is desirable. Principal factors affecting laser diode modulation bandwidth are the relaxation oscillation frequency, optical nonlinearities, and parasitic circuit effects. Spatial hole burning (SHB) was known as one of the limitations on the bandwidth of VCSELs by inhibiting high resonance frequencies [2-3]. Due to the nonuniform optical intensity, carriers at different locations in the quantum well have different stimulated recombination rates, and therefore exhibit different dynamic responses to small signal modulation. This nonuniformity causes an overdamping of the relaxation oscillation, and makes the intrinsic maximum bandwidth of oxide VCSELs much smaller than predicted by the conventional rate equation model which assumes uniform optical intensity.

## 6.1 Review of tapered oxide layer

Tapered oxide layer were first introduced to reduce scattering loss for small aperture VCSELs [4]. Recently, tapered oxide was theoretically investigated to reduce the nonlinear damping effect by making the electrical aperture smaller than the optical aperture, and thereby improves the modulation bandwidth [5]. Additionally, the tapered aperture also has lower parasitic capacitance. When devices are under modulation, the parasitic capacitance across a thin oxide layer (~ 30 nm) will limit the high speed performance [6]. A thicker oxide layer would help on reduction the capacitance. Unfortunately, thick oxide layer incur excess scattering losses. The tapered oxide can be thick at the boundary of mesa to provide a lower capacitance without the expense of excess scattering losses.

We previously demonstrated a simple planar approach for high-speed oxide-implanted VCSELs with good static operation characteristics and reliability [7-8]. In this chapter, we discuss the improved VCSELs utilizing a tapered oxide layer. The VCSELs exhibited similar static performance comparing with the previous devices, but superior high speed performance. The improvement was attributed to the reduced damping rate in the tapered oxide VCSEL. The extrinsic bandwidth limitation of the tapered oxide VCSELs was determined based on the equivalent circuit model.

### 6.2 Sample structure and fabrication process

The VCSEL epi-wafers were grown by Aixtron 2400 G3 metal-organic chemical vapor-phase deposition (MOCVD) on $n^+$-GaAs substrate, the structure of which consists of three GaAs/$Al_{0.3}Ga_{0.7}As$ (80Å/80Å) quantum well, sandwiched by fully doped n- and p-DBR mirrors. Both n- and p-DBR are composed of interlaced $1/4\lambda$-thick $Al_{0.15}Ga_{0.85}As$ and $Al_{0.9}Ga_{0.1}As$ layers, with the periods of 39.5 and 22, respectively. The gain peak position = 835 nm was determined by photoluminescence while the FP-dip resonant wavelength = 845 nm was determined by reflection measurement. For blunt oxide VCSELs, a 30-nm-thick $Al_{0.98}Ga_{0.02}As$ layer was placed in node position. For tapered oxide VCSEL, the tapered oxide layer was formed of a 10-nm-thick $Al_{0.99}Ga_{0.01}$ layer adjacent to a 200-nm-thick $Al_{0.98}Ga_{0.02}As$ layer, which is similar to Ref. [4]. The oxide-confined VCSEL process procedure has been described elsewhere [7-8]. Moreover, the mesa diameter of the fabricated device was 30 μm with a 5.5 μm oxide aperture. The diameter of oxide aperture was determined by dark-field microscopy and the size of spontaneous emission pattern. The device surface was quasi-planar so that the annular p-contact metal and the bond pad were on the same level. The p-contact was created by directly depositing Ti/Pt/Au on the upper heavily doped $p^+$ GaAs contact layer, and Au/Ge/Ni/Au was deposited on the bottom backside of the substrate following thinning down. Multiple proton implantations with a dose in the range of $10^{13} \sim 10^{15}$ $cm^{-2}$ and four different proton energy ranges between 200 to 420 keV were adapted according to simulation results of the stopping and range of ions in matter (SRIM). The implantation region was kept away from the mesa to prevent damage to the active region and consequent voiding of triggering reliability issues.

### 6.3 LIV performance and small signal response

The DC characteristics of completed VCSELs were measured with a probe station, an Agilent 4145A semiconductor parameter analyzer and an NIST traceable integration sphere with a photodiode. Fig. 6-1 plots curves of light output and voltage versus current (LIV) of typical VCSELs for both tapered oxide VCSELs and blunt oxide VCSELs with 5.5 μm aperture. The threshold current is ~ 1 mA (0.9 mA) for tapered (blunt) type VCSELs with the same slope efficiency of ~ 0.35 mW/mA. The similar static performance is not surprising since *1.* the oxide apertures here have the same size of 5~6μm and *2.* the blunt oxide don't incur excess scattering except at very small oxide size (< 3μm ). The maximal output power

exceeds 3 mW at room temperature and output power rollover occurs as the current increases above 12 mA.

The small signal response of VCSELs was measured using a calibrated vector network analyzer (Agilent 8720ES) with wafer probing and a 9 μm optical fiber connected to a New Focus 40 GHz photodetector. The emission of VCSEL was collimated and then focused to a diffraction-limited spot by a 10×/20× objective pair (NA=0.25/0.4). The overall coupling efficiency is around 20% ~ 30%. Fig. 6-2(a) and 6-2(b) show the modulation response of the VCSELs with the bias current for both tapered oxide VCSELs and blunt oxide VCSELs. At low bias currents, the bandwidth increased in proportion to the square root of the current above threshold, as expected from the rate equation analysis. For blunt oxide VCSEL, low frequency rollover was observed and the modulation response became gradually overdamped as the bias current increasing. In contrast, no rollover was observed in low frequency for tapered oxide VCSELs and the 3-dB bandwidth reached a maximum value of 13 GHz before fully overdamped. The observations coincide with the simulation results for blunt oxide VCSEL in which a significant overdamping was reported in the relaxation oscillation due to the nonuniformity of the transverse mode and significantly reduced the modulation bandwidth. [2, 5]

In Fig. 6-3, the 3-dB bandwidth is plotted with the root square of the bias current above threshold. The bandwidth are similar at low bias current for both tapered oxide VCSELs and blunt oxide VCSELs and saturated at the bias current higher than 8 mA. The maximal bandwidth for the blunt oxide VCSELs was 9.5 GHz and was enhanced to 13.2 GHz for the tapered oxide VCSELs. The modulation current efficiency factor was ~6.5 GHz/(mA)$^{1/2}$. As the Fig. 6-2 shows, the peak height of modulation response was higher in the tapered oxide VCSEL than that of blunt oxide VCSEL. The higher modulation amplitude in tapered oxide VCSELs implies the lower damping rate which was known to approximately proportion to the ratio between resonant frequency and peak modulation amplitude [9]. In depth, the damping rate, resonant frequency, and parasitic roll-off frequency can be obtained by fitting the experimental data to a three-pole approximation of the modulation response equation [9]. The $K$ factor can be found out from the slope of damping rate with the square of resonant frequency, as plotted in Fig. 6-4. It was shown the damping rate indeed about two times higher than that in the blunt oxide VCSELs and the $K$ factors were 0.15 ns and 0.4 ns, respectively. The comparison of the damping rate is also coincident with the theoretical prediction [2, 5]. If parasitic and other heating effects are ignored, the theoretical damping limited 3-dB bandwidth may be over 59 GHz for tapered oxide VCSEL and 22 GHz for blunt

oxide VCSEL, from the ration of $2 (2)^{1/2}/K$. [9]

As previously shown in Fig. 6-2(a), the 3-dB bandwidth reached a maximum value of ~13 GHz before fully overdamped. We therefore investigate the extrinsic bandwidth limitation on the tapered oxide VCSELs in the next. An equivalent circuit for the VCSEL impedance is useful for analysis of electrical bandwidth limitations. Inset of Fig. 6-5 shows the equivalent circuit model used to extract the circuit components. The resistance Rm represents the mirror loss while the Ra accounts for active region resistance. Ca represents a combination of capacitance of active area and oxide layer. A shunt resistance Rp is also included to account for pad loss and the pad capacitance is represented by Cp. Using this equivalent circuit, we can also investigate the extrinsic limitations on the modulation speed and determine the influence of the parasitic capacitance and the mirror resistance on the modulation bandwidth. To extract the capacitance of VCSELs, the measured amplitude and the phase of $S_{11}$ data were fitted from 100 MHz to 20 GHz. Fig. 6-5 illustrates measured and fitted $S_{11}$ results of the tapered oxide VCSEL at 6mA. Convergence of the fitting values to physically reasonable values was obtained using the following procedure. First, the Cp, Rp, Rm, Ca were extracted using zero bias $S_{11}$ data (where Ra is very large and can be neglected). Second, the Ra and Ca values were extracted by fitting the $S_{11}$ data for different bias currents. Finally, all the circuit parameters were allowed to vary about these values in order to minimize the squared error. The resulting Cp, Rp, and Rm were 160 fF, 5Ω and 51Ω respectively and the extracted Ra and Ca values for different bias currents were listed in Table 6-Ⅰ. Based on these extracted values, the electrical bandwidth can be determined from -3dB of the $S_{21}$ of the equivalent circuit shown in inset of Fig. 6-5. In consequence, electrical bandwidth of ~ 12.5 GHz was obtained and showed weak dependence on bias current. The calculated electrical bandwidth is coincident with the maximal measured modulation bandwidth and confirms the parasitic effects as the main limitation on the tapered oxide VCSELs.

**6.4 Eye diagram of tapered oxide VCSEL**

Finally, the eye diagram of the tapered oxide VCSELs was demonstrated. Microwave and light wave probes were used in conjunction with a 10 Gb/s pattern generator (MP1763 Anritsu) with a pseudorandom bit sequence of $2^{31}$-1 and a 12.5 GHz photoreceiver. Eye diagrams were obtained for back-to-back (BTB) transmission on VCSELs via a multimode

fiber. Fig. 6-6 shows the room temperature eye diagram of the tapered oxide VCSEL with compliance OC-192 mask. The eye diagram was measured at 6mA with an extinction ratio of 6dB. The clear open eye pattern indicates good performance of these VCSELs with the rising time ($T_r$) of 26 ps, the falling time ($T_f$) of 40 ps, and jitter(p-p) < 20 ps.

In conclusion, planarized oxide-implanted VCSELs were fabricated utilizing tapered oxide layer. The VCSELs exhibited similar static performance, but superior modulation bandwidth up to 13 GHz, compared with the VCSELs utilizing conventional blunt oxide layer. A very clean eye was demonstrated with rising time of 26 ps, falling time of 40 ps and jitter of less than 20 ps operating at 10Gb/s with 6mA bias and 6dB extinction ratio. The devices are fabricated using a simple, reliable planarized process and can be suitable for mass production. The high bandwidth and good eye characteristics make these devices very promising in future 10 Gb/s or even higher modulation applications.

**Reference**
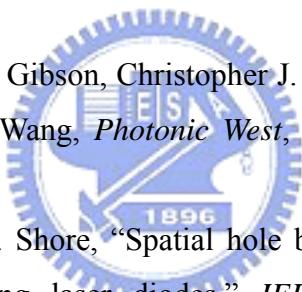
[1] Ian Aeby, Doug Collins, Brian Gibson, Christopher J. Helms, Hong Q. Hou, Wenlin Luo, David J. Bossert, Charlie X. Wang, *Photonic West*, San Jose, CA, pp. 152-161, 4994, (2003).

[2] A. Valle, J. Sarma, and K. A. Shore, "Spatial hole burning effects on the dynamics of vertical cavity surface-emitting laser diodes," *IEEE J.Quantum Electron.*, 31, pp. 1423–1431, 1995.

[3] Y. Liu, W.-C. Ng, F. Oyafuso, Klein and K. Hess, "Simulating the modulation response of VCSELs: the effects of diffusion capacitance and spatialhole-burning," *IEE Proc.-Optorlectron.,* 149, 182-188, 2002

[4] E. R. Hegblom, B. J. Thibeault, R. L. Naone, and L. A. Coldren, "Vertical cavity lasers with tapered oxide apertures for low scattering loss," *Electron. Lett.*, 33, pp. 869–879, 1997.

[5] Y. Liu, W.-C. Ng, B. Klein, and K. Hess, *IEEE J. QUANTUM ELECTRONICS,* 39, 99-108 (2003)

[6] C. H. Chang, L. Chrostowski, and Constance J. Chang-Hasnain, "Parasitics and Design Considerations onOxide-Implant VCSELs", *Photon. Technol. Lett. 13, 1274, 2001*

[7] H. C. Yu, S. J. Chang, Y. K. Su, C. P. Sung, Y. W. Lin, H. P. Yang, C. Y. Huang, J. M. Wang, *Mater. Sci. Eni. B.*, 106 (2004) 101-104.

[8] Y. H. Chang, Fang-I Lai, C. Y. Lu, H. C. Kuo, H. C. Yu, C. P. Sung, H. P. Yang and S. C.

Wang, *Semicond. Sci. Technol.* 19 (2004) L74–L77

[9] G. P. Agrawal and N. K. Dutta, "Semiconductor Lasers," 2nd 276-280, Van Nostrand Reinhold published.
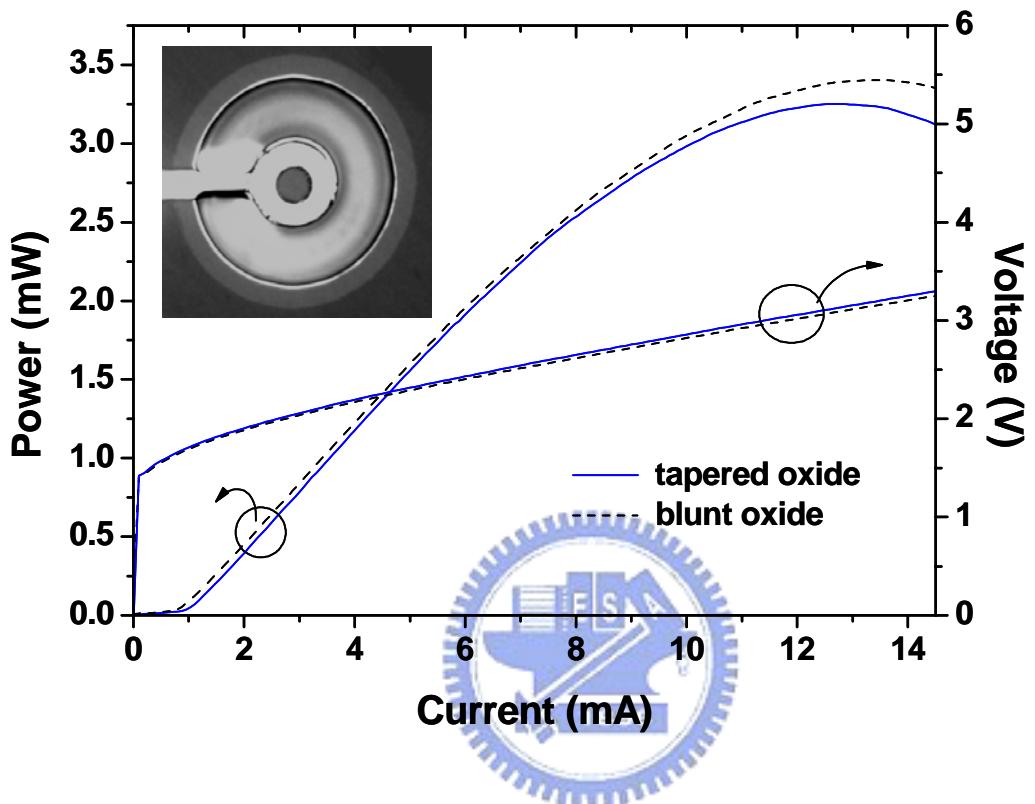
FIG. 6-1. L-I-V curves of the tapered oxide VCSELs (solid lines) and the blunt oxide VCSELs (dashed lines). Inset is top view image of the VCSEL.
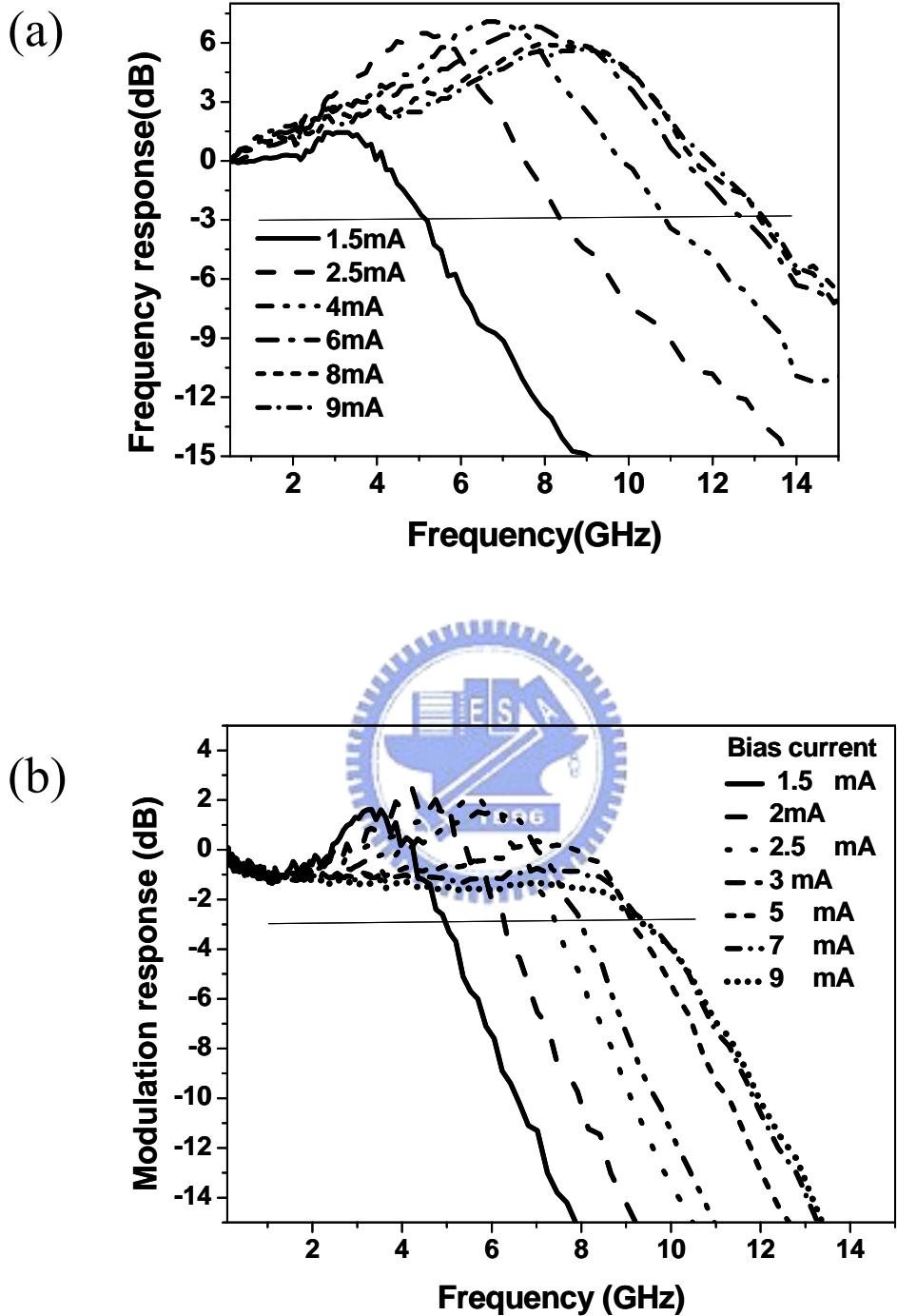
FIG. 6-2. Small signal modulation response of (a) the tapered oxide VCSEL and (b) the blunt oxide VCSEL.

73
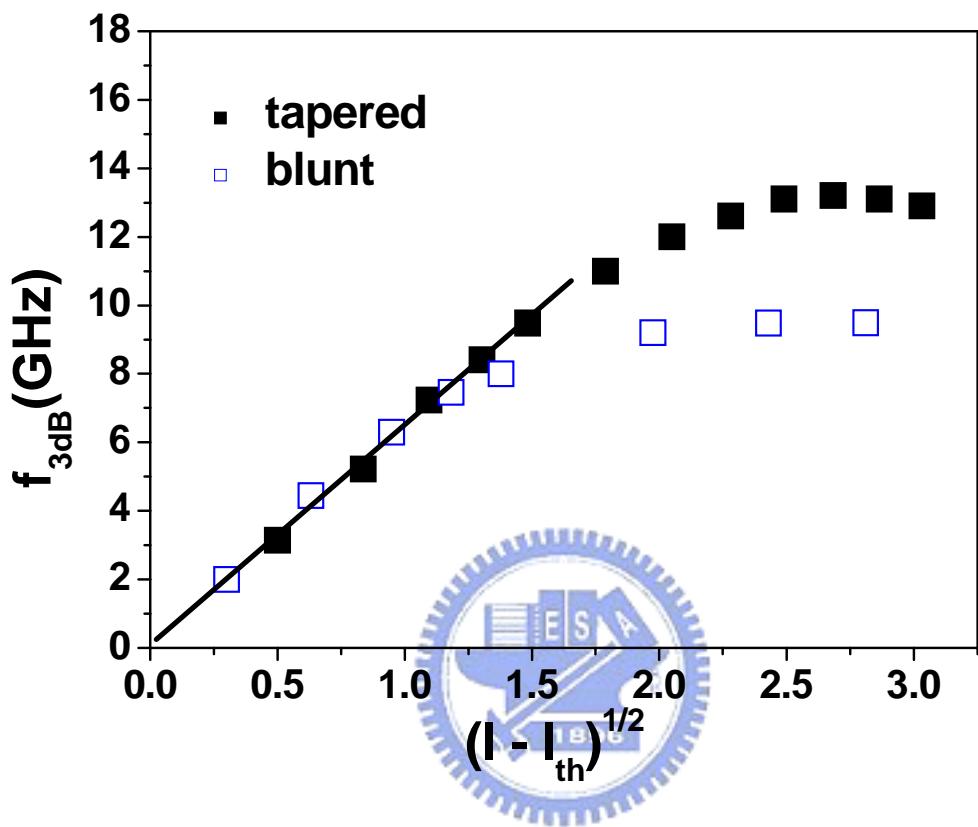
FIG. 6-3 3-dB frequency of the oxide-implanted VCSELs as a function of root square of bias current above threshold. (Filled square: tapered oxide VCSELs, Opened square: blunt oxide VCSELs)
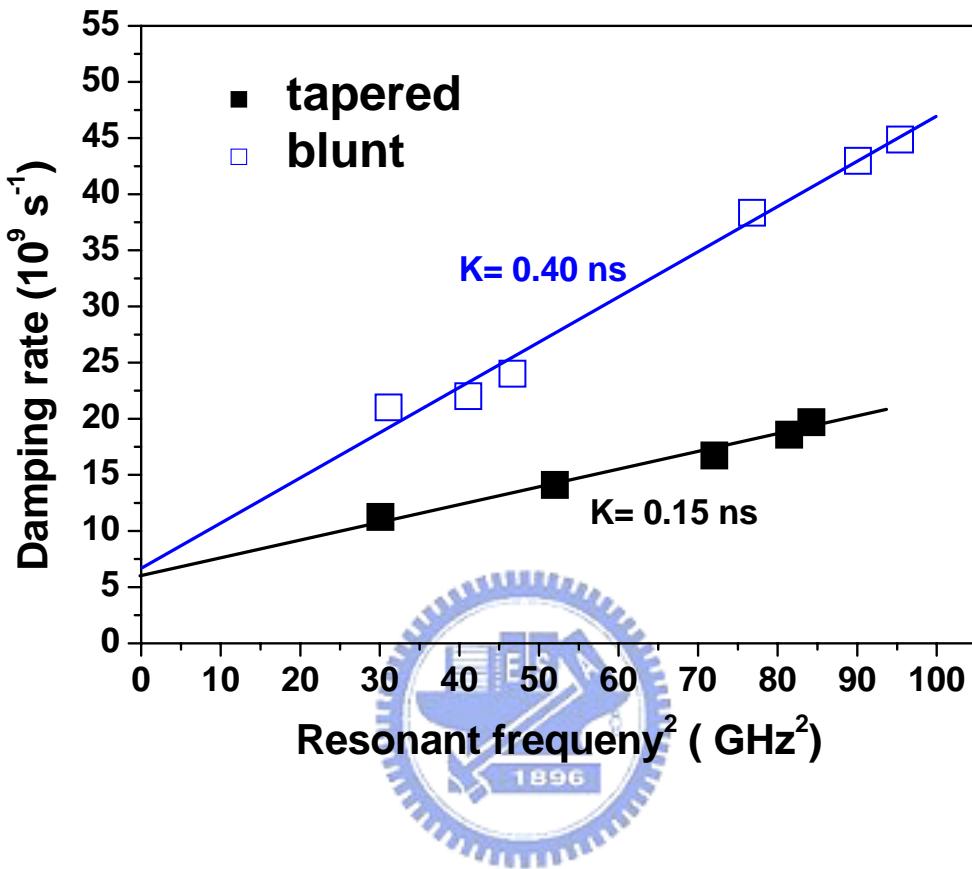
FIG. 6-4 Damping rate as a function of resonance frequency squared for VCSELs. (Filled square: tapered oxide VCSELs, Opened square: blunt oxide VCSELs)
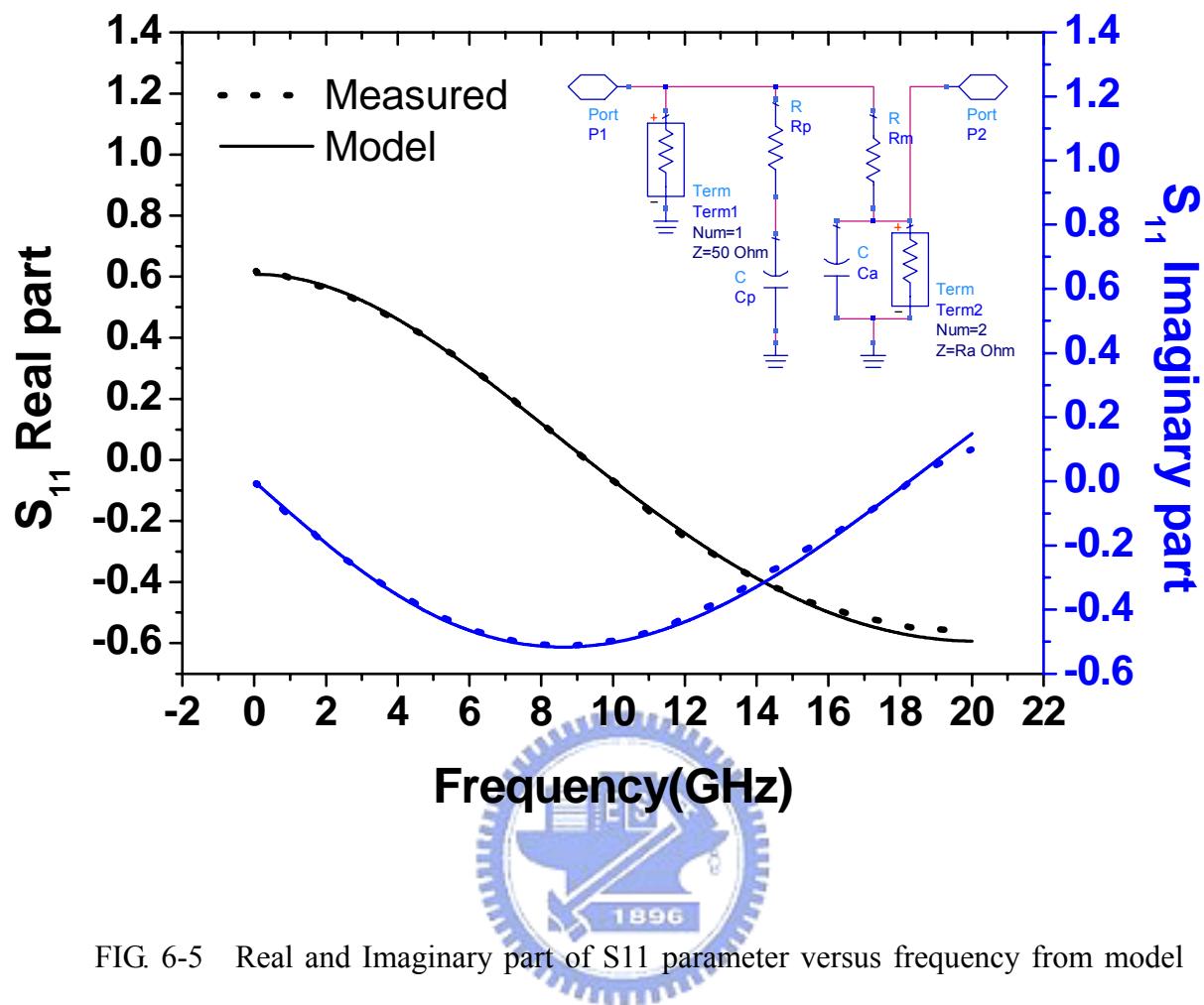
FIG. 6-5 Real and Imaginary part of S11 parameter versus frequency from model

and measured data. Inset is the equivalent circuit model of VCSELs.

FIG. 6-6    Eye diagram of the tapered oxide VCSELs at PRBS of $2^{31}$-1 and 6dB

extinction ratio, biased at 6 mA. (the time scale is 15.6 ps/div)
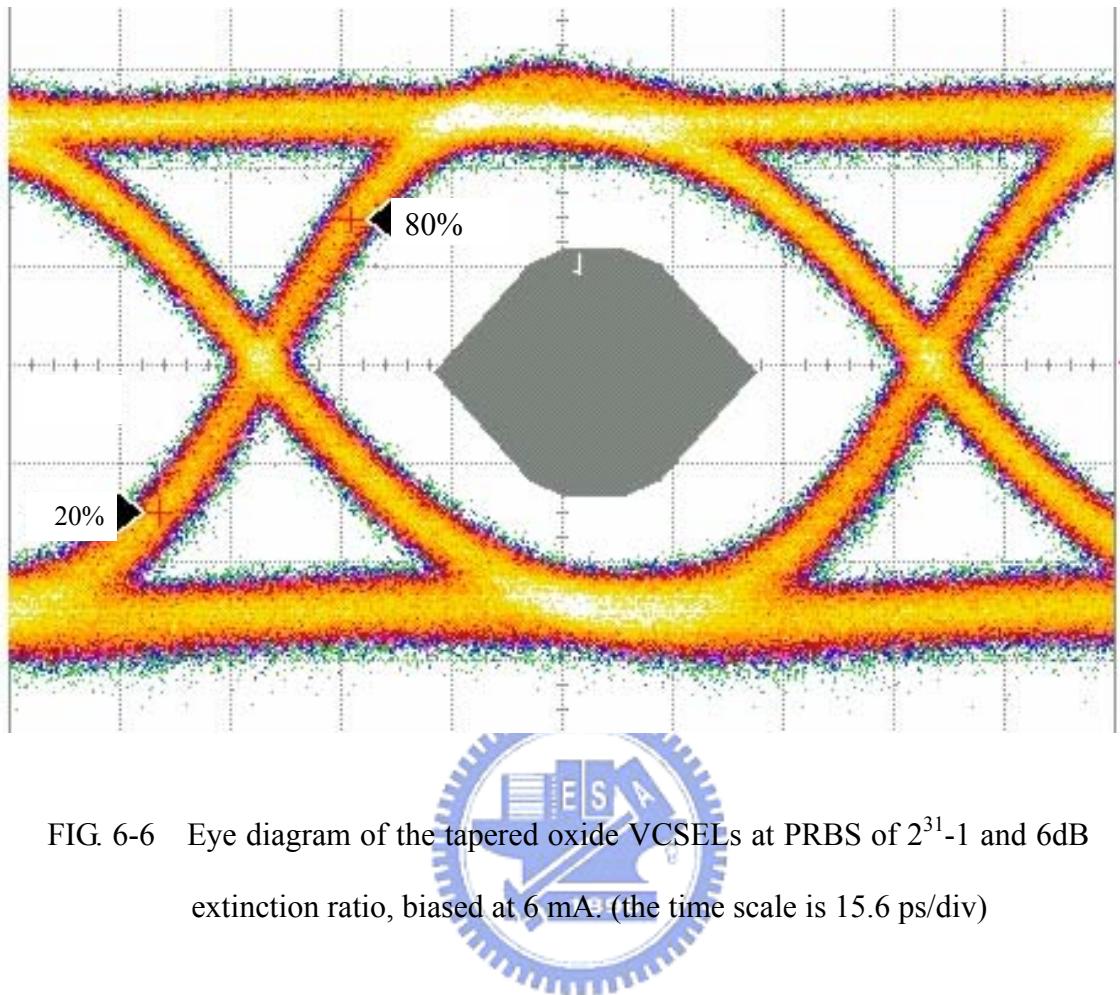
| Bias (mA) | 0 | 1 | 2.5 | 4 | 6 | 8 | 10 |
|---|---|---|---|---|---|---|---|
| $R_a(\Omega)$ | ∞ | 200 | 162 | 136 | 113 | 96 | 87 |
| $C_a$(fF) | 185 | 191 | 197 | 202 | 210 | 221 | 240 |

Table 6- I    Extracted circuit values at different bias current for the tapered oxide VCSELs.

# CHAPTER 7　　Summary

In summary, we have studied the high speed performance of vertical-cavity surface-emitting laser. The high speed performance was improved through modifying the gain region, proton-implantation process, and tapered oxide layer.

In chapter 4, we present the fabrication and characteristics of high performance 850 nm InGaAsP/InGaP strain-compensated MQWs vertical-cavity surface-emitting lasers. The InGaAsP/InGaP MQWs composition was optimized through theoretical calculations and the growth condition was optimized using photoluminescence. These VCSELs exhibited superior performance with characteristics threshold currents ~0.4 mA, and the slope efficiencies ~ 0.6 mW/mA. The threshold current change with temperature is less than 0.2 mA and the slope efficiency drops less than ~30% when the substrate temperature is raised from room temperature to $85^{\circ}$C. High modulation bandwidth of 14.5 GHz and modulation current efficiency factor of 11.6 GHz/(mA)$^{1/2}$ are demonstrated. We have also accumulated life test data up to 1000 hours at $70^{\circ}$C/8mA. Although the BCB planaried process has very low capacitance, the cost was relatively high due the lower yield. We adapted a simple, reliable process by proton implantation to cut down the device capacitance. In chapter 5, we reported the high speed performance of 850nm oxide-confined vertical cavity surface emitting lasers (VCSELs) with planar process and reduced parasitic capacitance. The parasitic capacitance of VCSELs was reduced using additional proton implantation. The small signal modulation bandwidth which was restricted by electrical parasitic capacitance expanded from 2.3 GHz to 9 GHz after proton implantation. To investigate the extrinsic bandwidth limitation of the oxide VCSELs, an equivalent circuit for the VCSEL impedance was introduced. The reflection coefficient showed that the electric parasitic pole exceeded 20 GHz. The eye diagram of VCSEL with reduced parasitic capacitance operating at 10Gbps with 6mA bias and 6dB extinction ratio showed a very clean eye with a jitter of less than 20 ps. This simple method can be applied to mass production with low cost.

In the last part, we present the improved oxide-implanted VCSELs utilizing the tapered oxide layer. The VCSELs exhibited similar static performance, but superior modulation bandwidth up to 13.2 GHz, compared with conventional blunt oxide VCSELs. The damping rate was reduced two times in the tapered oxide VCSEL and therefore enhanced the maximal modulation bandwidth. A very clean eye was demonstrated from improved VCSEL with rising time of 26 ps, falling time of 40 ps and jitter of less than 20 ps, operating at 10Gb/s

with 6mA bias and 6dB extinction ratio. A comprehensive small signal measurement and analysis was conducted. Based on the equivalent circuit model, the extrinsic bandwidth limitation of the tapered oxide VCSELs was determined.

# Curriculum Vita

*Name***:** Mr. Ya-Hsien Chang

*Place of Birth***:** Taipei, Taiwan

*Date of Birth***:** Jan 12, 1976

*Electronic Mail***:** orson.eo90g@nctu.edu.tw

*Education:*

Ph.D.    Electro-Optical Engineering, National Chiao Tung University, Taiwan

M.S.     Electronics, National Tsing-Hua University, Taiwan

B.S.     Electronic Engineering, National Tsing-Hua University, Taiwan

*Areas of Special Interest***:**

High speed Vertical-Cavity Surface-Emitting Laser

Optical / RF photonics measurement

Optical microscopy and micro-photoluminescence

*Title of Ph.D. Thesis:*

High speed characteristics of Vertical-Cavity Surface-Emitting Laser

Ya Hsien Chang (張亞銜)

## I. JOURNAL PAPERS:

2005

1. **Ya-Hsien Chang**[*], Hao-Chung Kuo[*], Yi-An Chang, Jung-Tang Chu, Min-Ying Tsai and Shing-Chung Wang, "10 Gbps InGaAs:Sb-GaAs-GaAsP Quantum Well Vertical Cavity Surface Emitting Lasers with 1.27 µm Emission Wavelengths", J. J. Appl. Phys. 44(4B), 2556-2559 (2005)

2. **Y. H. Chang**, T. H. Hsueh, F. I. Lai, C. W. Chang, C. C. Yu, H. W. Huang, C. F. Lin, H. C. Kuo and S. C. Wang," Fabrication and micro-photoluminescence investigation of Mg-doped gallium nitride Nanorods " J. J. Appl. Phys. J. J. Appl. Phys. 44(4B), 2657-2660, (2005)

3. **Y. H. Chang**, H. C. Kuo, Fang-I Lai, K. F. Tzeng, H. C. Yu, C. P. Sung, H. P. Yang and S. C. Wang, "High Speed (>13GHz) Modulation of 850nm Vertical Cavity Surface Emitting Lasers (VCSELs) with Tapered Oxide Confined Layer", IEE Proc.-Optoelectron., Vol. 152(3), pp. 170-173, 2005

4. Hao-Chung Kuo, **Ya-Hsien Chang**, Yi-An Chang, Jung-Tang Chu, Min-Ying Tsai, and Shing-Chung Wang," Single mode 1.27-µm InGaAs:Sb-GaAs-GaAsP Quantum Well Vertical Cavity Surface Emitting Lasers" IEEE J. Selected Topic of Quantum Electronics, 11(1) p.p 121-126 (2005)

5. H. C. Kuo, **Y. H. Chang**, H. H. Yao, Y. A. Chang, M. Y. Tsai, and S. C. Wang," High-Speed modulation of InGaAs:Sb-GaAs-GaAsP Quantum Well Vertical Cavity Surface Emitting Lasers with 1.27 µm Emission Wavelength" Photonics Technology Letter, **17**(3) p.p 528-530 (2005).

6. H. C. Kuo, Fang-I Lai, **Y. H. Chang**, M. Y. Tsai, S. Y. Kuo, S. C. Wang, N. Tansu, Jeng-Ya Yeh and Luke J. Maws, "Temperature dependent photoluminescence of highly strained InGaAsN/GaAs Quantum Well ( λ=1.28-1.45 µm) with GaAsP strain-compensated layer", accepted by J. J. Appl. Phys.

7. H. C. Kuo, H. H. Yao, **Y. S. Chang,** Y. A. Chang and S. C. Wang," MOCVD growth of InGaAs:Sb-GaAs-GaAsP Quantum Well Vertical Cavity Surface Emitting Lasers with 1.27 µm Emission Wavelength", J. of Crystal Growth 272(1-4), 538-542 (2004).

8. Tao-Hung Hsueh, Hung-Wen Huang, Chih-Chiang Kao, Ya-Hsien Chang, Miao-Chia. Ou-Yang, Hao-Chung Kuo, Jinn-Kong Sheu, and Shing-Chung Wang,

"Fabrication and Characterization of InGaN/GaN Multiple Quantum Wells Embedded within Nanorods", J. J. Appl. Phys. 44(4B), 2661-2663 (2005)

9. Yang HPD, Lai FI, **Chang YH**, Yu HC, Sung CP, Kuo HC, Wang SC, Lin SY, Chi JY, "Single-mode (SMSR>40dB) proton-implanted photonic crystal vertical-cavity surface-emitting lasers" 41 (6): 326-328 (2005)

2004

1. **Y. H. Chang**, H. C. Kuo, F. I. Lai, T. H. Hseuh and S. C. Wang, "Fabrication of high speed InGaAsP/InGaP strain-compensated VCSELs with 850 nm emission wavelength" published in IEEE J. of Lightwave Technologies , vol. 22(12) pp. 2828, 2004

2. **Y H Chang**, Fang-I Lai, C Y Lu, H C Kuo, H C Yu, C P Sung, H P Yang, S C Wang, " High-speed (>10 Gbps) 850 nm oxide-confined vertical cavity surface emitting lasers (VCSELs) with a planar process and reduced parasitic capacitance," Semiconductor Science and Technology, 19 (7): L74-L77 2004

3. Fang-I Lai, **Y. S. Chang**, T. H. Hseuh, H. C. Kuo and S. C. Wang, "Improvement of kink characteristics and high speed performance of implanted VCSELs with a top transparent overcoating" Material Science& Engineering (B), 113(3), pp. 203-206, 2004

4. H. C. Kuo, **Y. S. Chang**, C. F. Lin, T. C. Lu, and S. C. Wang, "MOCVD growth of high-performance InGaAsP/InGaP strain-compensated VCSELs with 850 nm emission wavelength," J. of Crystal Growth, 261 (2-3) 355-358 JAN 19 2004

5. H. C. Kuo, **Y. S. Chang,** F. Y. Lai, Tao-Hung Hseuh, L. T. Chu, L. H. Lai, and S. C. Wang, "High Speed Performance of 850 nm VCSEL silicon-implanted AlGaAs/GaAs vertical cavity emitting lasers," Solid-State Electronics 48(3): Dec, 483-485 MAR 2004 (SCI)

6. Yi-An Chang, Hao-Chung Kuo, **Ya-Hsien Chang**, Shing-Chung Wang, " Simulation of 1300-nm $In_{0.4}Ga_{0.6}As_{0.986}N_{0.014}/GaAs_{1-x}N_x$ quantum-well lasers with various $GaAs_{1-x}N_x$ strain compensated barriers ", Optics Communications 241() 195–202, (2004)

7. T. C. Lu, W. C. Hsu, **Y. S. Chang**, H. C. Kuo and S. C. Wang, "Measurement of Spontaneous Emission of oxide confined VCSEL," *Journal of Applied Physics, 96(11) 5992, 2004*

8. Fang-I Lai, Tao-Hung Hsueh, **Ya-Hsien Chang**, Hao-Chung Kuo, S C Wang, Li-Hong Laih, C P Song, H P Yang, "10 Gb/s single-mode vertical-cavity

surface-emitting laser with large aperture and oxygen implantation," Semiconductor Science and Technology, 19(8): L86 2004

2003

1.  H. C. Kuo, **Y. S. Chang**, F. Y. Lai, T. H. Hsueh, L. H. Laih, and S. C. Wang, "High-speed modulation of 850 nm InGaAsP/InGaP strain-compensated VCSELs," Electronics Letters, Vol. 39, No. 14, 1051-1053, July 2003

2.  Fang-I Lai, Tao-Hung Hsueh, **Ya-Hsien Chang**, Wen-Chun Shu, Li-Hung Lai, H. C. Kuo and S. C. Wang, "Performance of 850 nm AlGaAs/GaAs implanted VCSEL utilizing Si implantation induced disordering," Solid-State Electronics 47 (10): 1805-1809 OCT 2003

## II. CONFERENCE PAPERS:

**International:**

2005

1.  **Y. H. Chang**, G. R. Lin, H. C. Kuo, Jim Y. Chi, and S. C. Wang," Singlemode Monolithically Quantum-Dot Vertical-Cavity Surface-Emitting Laser in 1.3 μm with Side-mode Suppression ratio > 30dB", IEEE/LEOS 2005 Annual Meeting

2.  Hung-Pin D. Yang, Fang-I Lai, **Ya-Hsien Chang**, Hsin-Chieh Yu, Chia-Pin Sung, Hao-Chung Kuo, S. C. Wang, Shih-Yen Lin, Jim Y. Chi," Single Mode (SMSR>40dB) Proton-Implanted Photonic Crystal Vertical-Cavity Surface-Emitting Lasers", Conference of Laser and Electro-Optics, CThW1

3.  Hao-Chung Kuo, Yi-An Chang, **Ya-Hsien Chang**, Jung-Tang Chu, Min-Ying Tsai, and Shing-Chung Wang," Single mode 1.27-μm InGaAs:Sb-GaAs-GaAsP Quantum Well Vertical Cavity Surface Emitting Lasers", *SPIE Photonic West*, Conference 5364, paper 5737-22, Jan. 2005

4.  Yi-An Chang, Hao-Chung Kuo, **Ya-Hsien Chang**, Shing-Chung Wang, and Li-Hong Laih, "Simulation and analysis of 1300-nm $In_{0.4}Ga_{0.6}As_{0.986}N_{0.014}/GaAs_{1-x}N_x$ quantum-well lasers with various $GaAs_{1-x}N_x$ strain compensated barriers," *SPIE-Proceedings,* vol. 5628, pp. 40-48, 2005. (Invited)

**2004**

5. **Y. H. Chang**, H. C. Kuo, Y. A. Chang, M. Y. Tsai, S. C. Wang, N. Tansu, Jeng-Ya Yeh, Luke J. Mawst," Temperature dependent photoluminescence of highly strained InGaAsN/GaAs Quantum Well (1280-1450 nm) with GaAsP strain-compensated layer", *International Conference on Solid State Devices and Materials*, Tokyo, Japan (2004)

6. **Y. H. Chang**, H. C. Hsueh, F. I Lai, W. Y. Chang, C. C. Yu, W. H. Huang, C. F. Lin, H. C. Kuo, S. C. Wang," Observation of large spectral blue-shift in photoluminescence spectra of Mg-doped gallium nitride Nanorods", *International Conference on Solid State Devices and Materials*, Tokyo, Japan (2004)

7. **Ya-Hsien Chang** , Hao-Chung Kuo , Fang-I Lai , Yi-A Chang , Po-Tsung Lee , Shing-Chung Wang," Fabrication of high speed single mode 1.27 um InGaAs:Sb-GaAsP Quantum Wells Vertical Cavity Surface Emitting Laser", *International Conference on Solid State Devices and Materials*, Tokyo, Japan (2004)

8. **Y. S. Chang**, H.C. Kuo, F. I. Lai, Y. A. Chang, L. H. Laih and S. C. Wang, " Improvement of high speed performance for 10-Gb/s 850 nm VCSELs," *SPIE Photonic West*, Conference 5364, paper 5364-10, Jan. 2004

9. T. H. Hsueh, **Y. H. Chang**, F. I Lai, H. W. Hung, M. C. Ou-yang, C. W. Chang, H. C. Kuo, and S. C. Wang, "Fabrication and emission characteristic of InGaN/GaN multiple quantum wells nanorods," *CLEO 2004*, IWA20.

10. H. C. Kuo, **Y. S. Chang**, F. Y. Lai, T. H. Hsueh, L. H. Lai, and S. C. Wang, "High speed Perfromance of 850 nm InGaAsP/InGaP strain-compensated VCSELs", *SPIE Proceeding* 2004 (EI)

11. Tao-Hung Hsueh, Hung-Wen Huang, Chih-Chiang Kao, **Ya-Hsien Chang**, Miaochia Ou-Yang, Hao-Chung Kuo, Shing-Chung Wang," InGaN/GaN Multi-Quantum-Well Nanorods Fabricated by Plasma Etching Using Self-assembled Nickel Nano-masks", *International Conference on Solid State Devices and Materials*, Tokyo, Japan (2004)

**2003**

12. H. C. Kuo, **Y. H. Chang**, T. H. Hseuh, F. I Lai and S. C. Wang, "Development of 850nm VCSELs for OC-192 Application," *ECS conference2003*. (invited) (EI)

13. H. C. Kuo, **Y.S. Chang**, T. H. Hsueh, C. C. Yu, J. W. Chang, C. F. Lin and S. C. Wang, "Fabrication and Characterization of GaN Nanorods, " *Electrochemical Soc. Proc.* Wide Bandgap Optoelectronic Materials and Devices (2003).

14. H. C. Kuo, T. C. Lu, **Y. S. Chang**, F. Y. Lai, G. C. Kao, L. H. Laih, and S. C. Wang, "Growth and characterization of 850nm InGaAsP/InGaP strain-compensated VCSELs by MOCVD," *PR/CLEO 2003*, paper W2B-(2)-7, December 2003

15. H. C. Kuo, W. C. Shu, T. C. Lu, **Ya-Hsien Chang**, Fang-i Lai, Li-Hung Lai, and S. C. Wang, "Characterization of 850nm AlGaAs/GaAs implant vertical cavity emitting lasers utilizing silicon implantation induced disordering," *PR/CLEO 2003*, paper THP-(2)-6, December 2003

16. Fang-I Lai, L. H. Laih, **Y. S. Chang**, T. H. Shei, H. C. Kuo, and S. C. Wang, "Enhancement of proton-implanted GaAs VCSEL performance by transparent overcoating," *PR/ CLEO 2003*, paper WP-(2)-9, December 2003

Domestic:
1. **Y. H. Chang**, C. C. Kao, T. H. Hsueh, T. C. Lu, H. C. Kuo, and S. C. Wang, "High speed modulation of InGaAsP/InGaP strain-compensated VCSELs," *Optics and Photonics Taiwan '03*, paper TB2-6, December 2003

2. **Y. H. Chang**, C. W. Chang, C. C. Yu, H. C. Kuo, and S. C. Wang, "Observation of enormous blue-shift in photoluminescence spectrum of Mg-doped GaN Nanorods," *Optics and Photonics Taiwan '03*, paper PA1-10, December 2003

3. J. Y. Lu, **Y. H. Chang**, F. Y. Lai, H. C. Kuo, and S. C. Wang, "Small signal modulation response of oxide-confined VCSEL with different aperture size," *Optics and Photonics Taiwan '03*, paper FB4-2, December 2003

4. T. C. Lu, **Y. H. Chang**, C. W. Chang, W. C. Hsu, H. C. Kuo, and S. C. Wang, "Spectrally resolved spontaneous emission patterns of oxide-confined vertical-cavity surface-emitting lasers," *Optics and Photonics Taiwan '03*, paper PA1-11, December 2003

5. C. L. Luo, G. F. Zeng, **Y. H. Chang**, F. Y. Lai, H. C. Kuo, and S. C. Wang, "Simulation of multimode operation effects on modulation response of VCSEL," *Optics and Photonics Taiwan '03*, paper FA2-6, December 2003

6. C. W. Chang, C. L. Lee, **Y. H. Chang**, M. C. O-Yang, H. C. Kuo, and S. C. Wang, "Photoluminescence of gaN grown by HVPE with different V/III ratio," *Optics and Photonics Taiwan '03*, paper FA2-7, December 2003

7. F. Y. Lai, T. H. Hsueh, **Y. H. Chang,** W. C. Hsu, L. H. Lai, H. C. Kuo, and S. C. Wang, "Performance of enhancement of AlGaAs/GaAs VCSEL utilizing silicon implantation induced disordering," *Optics and Photonics Taiwan '03*, paper FB3-1, December 2003

8. W. Y. Chen, F. Y. Lai, **Y. H. Chang**, L. H. Laih, H. C. Kuo, and S. C. Wang, "Performance of GaAs VCSEL with a top transparent," *Optics and Photonics Taiwan '03*, paper FB3-8, December 2003

9. M. C. O-Yang, T. H. Hsueh, **Y. H. Chang**, C. W. Chang, H. C. Kuo, and S. C. Wang, "Fabrication and optical characteristic of InGaN Multi-quantum well nanorods," *Optics and Photonics Taiwan '03*, paper FA3-3, December 2003